

**Titre:** Analysis and Applications of the Substrate-Integrated Image Guide  
Title: (SIIG) Structure for THz Components and Systems Development

**Auteur:** Mohammad Moradi  
Author:

**Date:** 2023

**Type:** Mémoire ou thèse / Dissertation or Thesis

**Référence:** Moradi, M. (2023). Analysis and Applications of the Substrate-Integrated Image Guide (SIIG) Structure for THz Components and Systems Development [Thèse de doctorat, Polytechnique Montréal]. PolyPublie.  
Citation: <https://publications.polymtl.ca/62748/>

 **Document en libre accès dans PolyPublie**  
Open Access document in PolyPublie

**URL de PolyPublie:** <https://publications.polymtl.ca/62748/>  
PolyPublie URL:

**Directeurs de recherche:** Mohammad S. Sharawi, & Ke Wu  
Advisors:

**Programme:** Génie électrique  
Program:

**POLYTECHNIQUE MONTRÉAL**

affiliée à l'Université de Montréal

**Analysis and Applications of the Substrate-Integrated Image Guide (SIIG)  
Structure for THz Components and Systems Development**

**MOHAMMAD MORADI**

Département de génie électrique

Thèse présentée en vue de l'obtention du diplôme de *Philosophiæ Doctor*  
Génie électrique

Décembre 2023



**POLYTECHNIQUE MONTRÉAL**

affiliée à l'Université de Montréal

Cette thèse intitulée :

**Analysis and Applications of the Substrate-Integrated Image Guide (SIIG)  
Structure for THz Components and Systems Development**

présentée par **Mohammad MORADI**

en vue de l'obtention du diplôme de *Philosophiæ Doctor*  
a été dûment acceptée par le jury d'examen constitué de :

**Jean-Jacques LAURIN**, président

**Mohammad S. SHARAWI**, membre et directeur de recherche

**Ke WU**, membre et codirecteur de recherche

**Elham BALADI**, membre

**Tayeb A. DENIDNI**, membre externe

## DEDICATION

*I would like to dedicate this thesis to my cherished family, whom I missed dearly, your unwavering love and understanding sustained me throughout the challenges and triumphs of my Ph.D. Your patience, encouragement, and unwavering belief in me have been my greatest motivation.*

*With heartfelt gratitude and profound appreciation,*

*Mohammad*

## ACKNOWLEDGEMENTS

I would like to extend my heartfelt appreciation to the individuals who have been instrumental in the completion of this thesis.

First and foremost, I wish to express my profound gratitude to my dedicated supervisor, Prof. Mohammad S. Sharawi. Your guidance, unwavering support, and expertise have been the cornerstone of my academic journey. Your mentorship has provided invaluable insights and has helped shape this work.

I am deeply thankful to my co-supervisor, Prof. Ke Wu, whose expertise in the field has enriched this research. Your contributions and insights have broadened the horizons of my understanding.

I would like to extend my sincere gratitude to Prof. Jean-Jacques Laurin, who served as the jury president for this thesis. I am honored to have benefited from your expertise and perspective. I also wish to express my appreciation to Prof. Elham Baladi and Prof. Tayeb Denidni, who served as jury members. Your valuable feedback and evaluation have contributed significantly to the quality of this work.

A special note of thanks goes to the dedicated technician staff: Traian Antonescu, Steve Dubé, and Maxime Thibault. Your technical expertise, support, and assistance during the fabrication process have been invaluable to the successful completion of this research.

I am grateful to each of you for your guidance, support, and contributions, without which this thesis would not have been possible.

I also wish to express my deep appreciation to the Government of Quebec for providing the Fonds de Recherche du Québec Nature et technologies, which partially supported my Ph.D. research. This financial assistance played a crucial role in the successful execution of my work.

Mohammad Moradi

## RÉSUMÉ

En réponse à la croissance exponentielle des utilisateurs de systèmes de communication sans fil, les canaux de communication font face à une congestion croissante. L'essor des applications d'imagerie haute résolution, des dispositifs spectroscopiques sensibles aux molécules et de la demande croissante de transmission de données sans fil ultra-large bande dans des environnements multi-utilisateurs a attiré une attention significative dans le domaine des circuits intégrés et des systèmes haute fréquence. Avec l'introduction imminente de la technologie 6G, une grande variété de capteurs sans fil et de dispositifs de communication se propageront rapidement. Cette expansion souligne le besoin critique d'un cadre de système hautement intégré, un défi amplifié par l'espace limité disponible pour accueillir de nombreux capteurs et composants de communication. Pour relever ces défis complexes, l'utilisation des technologies terahertz (THz) présente une solution prometteuse.

Dans cette thèse, nous avons étudié la structure du guide d'image intégré au substrat en tant que technologie prometteuse pour les applications sub-THz et THz. En conséquence, nous avons d'abord proposé et développé deux méthodes analytiques pour modéliser des guides d'ondes diélectriques avec perte: 1) En considérant que les régions adjacentes ont des perforations périodiques dans un substrat diélectrique avec perte et en appliquant la *théorie Floquet* et l'expansion des *séries de Fourier*, nous avons formulé un problème de système eigen pour les composants de champ électrique. Le facteur effectif de permittivité et de dissipation de chaque mode peut être extrait avec précision des fréquences de coupure calculées. La permittivité efficace et le facteur de dissipation de chaque mode peuvent être extraits avec précision à partir des fréquences de coupure calculées. Cette méthode peut être utilisée efficacement pour modéliser avec précision la propagation des ondes le long des matériaux diélectriques avec des perforations périodiques. 2) en considérant les plaques métalliques comme des conducteurs avec perte, en appliquant la *condition de bord d'impédance (IBC)* et en supposant que le facteur de dissipation ( $\tan \delta$ ) est le même pour tous les matériaux diélectriques, nous avons réalisé une analyse modale modifiée qui fournit des informations exactes sur la distribution du champ électromagnétique et la constante de propagation des modes de propagation le long des guides d'ondes diélectriques. Cette méthode peut être appliquée efficacement à tous les guides d'ondes diélectriques multicouches, y compris le guide diélectrique à bande, le guide d'image isolé et le guide à bande de bande.

L'exactitude, l'applicabilité et l'efficacité des méthodes proposées sont démontrées par comparaison avec les simulations de logiciels EM commerciaux (par exemple, *CST Studio Suite*

et *Ansys HFSS*) et un prototype de guide d'ondes fabriqué. Un excellent accord entre les modèles analytiques développés et les simulations en ondes complètes est obtenu tout en réduisant considérablement le temps de simulation. Il convient de mentionner que les méthodes proposées peuvent modéliser la propagation des ondes le long des guides d'ondes diélectriques multicouches dans toutes les plages de fréquence. Cependant, en raison des limitations de fabrication et de la disponibilité des matériaux au *centre de recherche Poly-Grames*, une structure de guide d'image intégré au substrat (SIIG) pour une fréquence de fonctionnement de 150 GHz a été fabriquée. La comparaison avec le guide d'ondes SIIG fabriqué en tant que prototype expérimental a démontré que la méthode proposée est hautement précise dans des scénarios réalistes.

Nous avons étudié et démontré la technologie SIIG comme une candidate prometteuse pour les applications THz. En raison de son mécanisme de guidage, le SIIG présente des pertes de transmission très faibles. De plus, étant donné que le plan de masse métallique n'intervient pas dans le processus de guidage des ondes, cette technologie génère des pertes de conducteur très faibles, ce qui est crucial dans le régime THz. La structure SIIG étudiée offre l'avantage d'incorporer un film d'isolation à faible permittivité en option entre le plan de masse et le substrat à haute permittivité. Ce film supplémentaire permet de minimiser efficacement les pertes de conducteur, car il atténue l'intensité des champs magnétiques à la surface du plan de masse, ce qui réduit les densités de courant induit. En éliminant la couche d'isolation facultative, la structure SIIG étudiée permet une fabrication plus simple et une intégration potentielle sans couture avec d'autres composants de circuit pour les applications de circuit intégré au substrat (SIC). La suppression de la couche d'isolation facultative simplifie l'intégration avec différentes technologies en leur permettant de partager le même substrat et le même plan de masse. Les effets des paramètres structuraux sur le comportement de guidage des ondes du SIIG sont étudiés de manière analytique. Deux guides d'ondes prototypes fonctionnant dans les fréquences de 150 GHz et 300 GHz sont fabriqués en choisissant les meilleurs paramètres structuraux disponibles. Les réponses des guides d'ondes fabriqués sont mesurées et comparées avec la méthode analytique et le logiciel EM commercial. Les comparaisons effectuées montrent un excellent accord entre les mesures et les simulations.

Bien que le guide d'ondes SIIG présente des performances exceptionnelles dans des configurations linéaires, il rencontre des problèmes de fuite dans les virages serrés. Lorsque l'onde guidée rencontre ces virages brusques, elle commence à fuir dans les régions perforées, ce qui entraîne une dégradation des performances, en particulier en ce qui concerne les pertes par insertion. Ces problèmes peuvent limiter les applications des technologies SIIG, en particulier dans les applications nécessitant des discontinuités marquées, telles que les diviseurs/combinés de puissance compacts.

Dans cette thèse, une solution est présentée pour relever les défis de fuite à des virages aigus dans les guides d'ondes SIIG. Cette solution implique l'intégration d'un guide d'onde hybride, formé en introduisant un guide d'onde métallique intégré au substrat (SIMIG) dans la structure SIIG. Cette innovation empêche efficacement l'onde guidée de fuir dans les régions perforées et améliore les performances globales du SIIG à des virages tranchants. Par conséquent, cette percée permet la création d'un diviseur/combiner de puissance hautement compact en utilisant la technologie SIIG.

## ABSTRACT

In response to the exponential growth in wireless communication system users, communication channels are now facing increasing congestion. The rise of high-resolution imaging applications, molecular-sensitive spectroscopic devices, and a soaring demand for ultra-broadband wireless data transmission in multi-user environments has captured significant attention within the realm of high-frequency integrated circuits and systems. With the imminent introduction of 6G technology, a diverse array of wireless sensors and communication devices will rapidly proliferate. This expansion underscores the critical need for a highly integrated system framework, a challenge compounded by the limited available space for accommodating numerous sensors and communication components. In addressing these intricate challenges, the utilization of terahertz (THz) technologies presents a promising solution.

In this thesis, we investigated the Substrate-Integrated Image Guide (SIIG) structure as a promising technology for THz applications. Accordingly, we first proposed and developed two analytical methods for modeling lossy dielectric waveguides: 1) by considering the adjacent regions to have periodic perforations in a lossy dielectric substrate and applying the *Floquet Theory* and *Fourier Series* expansion, we formulated an eigensystem problem for electric field components. Solutions to this eigensystem problem will provide each propagating mode's cut-off frequency and field distribution. The effective permittivity and dissipation factor of each mode can be accurately extracted from the calculated cut-off frequencies. This method can be effectively used to accurately model wave propagation along lossy dielectric materials with periodic perforations. 2) by considering the metallic plates as lossy conductors, applying the *Impedance Boundary Condition (IBC)*, and assuming the dissipation factor ( $\tan \delta$ ) for all dielectric materials, we completed a modified modal analysis that provides exact information on the electromagnetic field distribution and propagation constant of propagating modes along the dielectric waveguides. This method can be effectively applied to all layered dielectric waveguides, including strip dielectric guide, insulated image guide, and strip-slab guide.

The proposed methods' accuracy, applicability, and efficiency are demonstrated through comparison with the commercial EM software (e.g., *CST Studio Suite* and *Ansys HFSS*) simulations and a fabricated waveguide prototype. Excellent agreement between the developed analytical models and full-wave simulations is achieved while the simulation run-time is reduced significantly. It is worth mentioning that the proposed methods can model the wave propagation along layered dielectric waveguides in all frequency ranges. However, because of the fabrication limitation and material availability at the *Poly-Grames Research Center*, a

substrate-integrated image guide (SIIG) structure for an operating frequency of 150 GHz was fabricated. Comparison with the fabricated SIIG waveguide as an experimental prototype demonstrated that the proposed method has high accuracy in realistic scenarios.

We investigated and demonstrated the SIIG technology as a promising candidate for THz applications. Due to its guiding mechanism, the SIIG possesses very low transmission losses. Further, since the metallic ground plane is not involved in the wave guidance process, this technology produces very low conductor losses, which is critical in the THz regime. The investigated SIIG structure offers the advantage of incorporating an optional low-permittivity insulation film between the ground plane and the high-permittivity substrate. This additional film effectively minimizes conductor losses, as it mitigates the intensity of magnetic fields at the ground plane surface, leading to reduced induced current densities. Through the removal of the insulating layer, the investigated SIIG structure provides an easier fabrication and a potential for seamless integration with other circuit components for substrate-integrated circuit (SIC) applications. The elimination of the optional insulating layer simplifies integration with different technologies by allowing them to share the same substrate and ground plane. The effects of the structural parameters on the wave guidance behavior of the SIIG are analytically studied. Two prototype waveguides operating within the frequencies of 150 GHz and 300 GHz are fabricated by choosing the best available structural parameters. The responses of the fabricated waveguides are measured and compared with the analytical method and the commercial EM software. The provided comparisons have demonstrated excellent agreement between the measurements and the simulations.

While the SIIG waveguide demonstrates exceptional performance in straight-line configurations, it experiences issues with leakage at sharp bends. When the guided wave encounters these sharp turns, it begins to leak into the perforated regions, resulting in a degradation of performance, particularly with respect to insertion loss. These issues may limit the applications of SIIG technologies, especially in applications requiring sharp discontinuities, such as compact power dividers/combiners.

In this thesis, a solution is presented to tackle the leakage challenges at sharp bends in SIIG waveguides. This solution involves the integration of a hybrid waveguide, formed by introducing a Substrate-Integrated Metallic Image Guide (SIMIG) waveguide into the SIIG structure. This innovation effectively prevents the guided wave from leaking into the perforated regions and enhances the overall performance of SIIG at sharp bends. Consequently, this breakthrough allows for the creation of a highly compact power divider/combiner using SIIG technology.



# TABLE OF CONTENTS

DEDICATION . . . . .	iii
ACKNOWLEDGEMENTS . . . . .	iv
RÉSUMÉ . . . . .	v
ABSTRACT . . . . .	viii
TABLE OF CONTENTS . . . . .	x
LIST OF TABLES . . . . .	xii
LIST OF FIGURES . . . . .	xiii
LIST OF SYMBOLS AND ABBREVIATIONS . . . . .	xviii
LIST OF APPENDICES . . . . .	xix
CHAPTER 1 INTRODUCTION . . . . .	1
1.1 Motivation . . . . .	1
1.2 Problem Statement . . . . .	2
1.3 Research Objectives . . . . .	7
1.4 Thesis Organization . . . . .	9
CHAPTER 2 ARTICLE 1: ANALYTICAL MODEL OF GUIDED WAVES IN PERIODICALLY PERFORATED DIELECTRIC STRUCTURE AND ITS APPLICATIONS TO TERAHERTZ SUBSTRATE-INTEGRATED IMAGE GUIDE (SIIG)	12
2.1 Introduction . . . . .	12
2.2 Effective Permittivity Extraction . . . . .	14
2.3 Modal Analysis . . . . .	19
2.3.1 Extracting $k_y$ . . . . .	20
2.3.2 Extracting $k_z$ . . . . .	24
2.4 Validation using eigen-mode solver and Experimental Prototype . . . . .	25
2.5 Conclusion . . . . .	35

CHAPTER 3	ARTICLE 2: EXPLORING LOW-LOSS WIDEBAND SUBSTRATE- INTEGRATED IMAGE GUIDES (SIIG) FOR TERAHERTZ APPLICATIONS .	36
3.1	Introduction . . . . .	36
3.2	Substrate Integrated Image Guide (SIIG) Analysis . . . . .	40
3.3	SIIG Design Parameters And Procedure . . . . .	48
3.4	Fabrications And Measurements . . . . .	52
3.5	Comparison . . . . .	57
3.6	Conclusion . . . . .	58
CHAPTER 4	SUBSTRATE-INTEGRATED HYBRID DIELECTRIC-METALLIC IM- AGE GUIDE (SIHDMIG) ARCHITECTURE AND ITS APPLICATIONS IN DE- VELOPING SUB-THZ/THZ POWER DIVIDER . . . . .	60
4.1	Introduction . . . . .	60
4.2	Feasibility of Substrate-Integrated Hybrid Dielectric-Metallic Image Guide .	62
4.2.1	Substrate-Integrated Image Guide (SIIG) Structure . . . . .	62
4.2.2	Substrate-Integrated Metallic Image Guide (SIMIG) Structure . . . .	65
4.2.3	Substrate-Integrated Hybrid Dielectric-Metallic Image Guide . . . . .	67
4.3	Substrate-Integrated Hybrid Dielectric-Metallic Image Guide Performance at Sharp Bends . . . . .	70
4.4	Developing Compact Power/Divider for SIIG Technology . . . . .	76
4.5	Conclusion . . . . .	80
CHAPTER 5	CONCLUSION AND RECOMMENDATION . . . . .	81
5.1	Conclusion . . . . .	81
5.2	Recommendation . . . . .	82
REFERENCES	. . . . .	84
APPENDICES	. . . . .	92

## LIST OF TABLES

Table 2.1	Recorded Run-Time and Calculated Relative Error of Different Methods Used to Extract the Propagating Modes. . . . .	29
Table 3.1	Comparison of Measured Results among Different THz Transmission Lines. . . . .	59

## LIST OF FIGURES

Figure 1.1	Prospective indoor and outdoor applications of sub-THz and THz communications [1]. . . . .	1
Figure 1.2	Different metallic-bases transmission lines [2]. . . . .	3
Figure 1.3	Dielectric and optical waveguides [3]. (a) Silica taper fiber, (b) integrated As <sub>2</sub> S <sub>3</sub> waveguide buried on SiO <sub>2</sub> , (c) silica photonic crystal fiber, (d) suspended silicon waveguide, (e) dual-nanoweb silica fiber, (f) suspended silicon waveguide membrane. . . . .	4
Figure 1.4	Technology gap between the microwave and optical region of the electromagnetic spectrum. . . . .	5
Figure 1.5	Exposed view of (a) insulated image guide and (b) exploded view of substrate integrated (insulated) image guide (SIIG) [4]. . . . .	6
Figure 2.1	Cross-sectional view of a two-dimensional array of (a) rectangular and (b) circular perforations in a dielectric substrate. . . . .	16
Figure 2.2	Exposed view of (a) actual Substrate Integrated Image Guide (SIIG) structure and (b) its equivalent model. . . . .	20
Figure 2.3	Modal analysis structures: (a) SIIG equivalent model, (b) the first stage sub-structure, and (c) the second stage sub-structure. . . . .	22
Figure 2.4	Extracted effective permittivity of alumina substrate with rectangular perforations. . . . .	26
Figure 2.5	Extracted dissipation factor of alumina substrate with rectangular perforations. . . . .	26
Figure 2.6	Normalized electric (i.e., $E_z$ for the vertical mode) and magnetic (i.e., $H_z$ for the horizontal mode) field magnitude distribution inside an alumina substrate with rectangular perforations: a) CST Studio Suite software (V-Pol), b) Ansys HFSS software (V-Pol), c) analytical method with $N = 10$ (V-Pol), d) analytical method with $N = 20$ (V-Pol), e) CST Studio Suite software (H-Pol), f) Ansys HFSS software (H-Pol), g) analytical method with $N = 10$ (H-Pol), h) analytical method with $N = 20$ (H-Pol). . . . .	27
Figure 2.7	Extracted effective permittivity of alumina substrate with circular perforations. . . . .	29
Figure 2.8	Extracted dissipation factor of alumina substrate with circular perforations. . . . .	30

Figure 2.9	Normalized electric (i.e., $E_z$ for the vertical mode) and magnetic (i.e., $H_z$ for the horizontal mode) field magnitude distribution inside an alumina substrate with circular perforations: a) CST Studio Suite software (V-Pol), b) Ansys HFSS software (V-Pol), c) analytical method with $N = 10$ (V-Pol), d) analytical method with $N = 20$ (V-Pol), e) CST Studio Suite software (H-Pol), f) Ansys HFSS software (H-Pol), g) analytical method with $N = 10$ (H-Pol), h) analytical method with $N = 20$ (H-Pol). . . . .	30
Figure 2.10	Dispersion diagram of an alumina substrate having periodic rectangular perforations with different sizes. . . . .	31
Figure 2.11	Dispersion diagram of an alumina substrate having periodic circular perforations with different sizes. . . . .	31
Figure 2.12	a) The fabricated SIIG structure fed by WR-5.1 waveguide, b) the fabricated alumina substrate having 5 rows of circular perforations, c) zoomed view of the guiding channel and adjacent perforated regions. . . . .	32
Figure 2.13	Extracted normalized phase constant of the mentioned SIIG structure. . . . .	33
Figure 2.14	Extracted attenuation constant of the mentioned SIIG structure. . . . .	33
Figure 2.15	Extracted normalized phase constant of the fabricated SIIG structure. . . . .	34
Figure 2.16	Extracted attenuation constant of the fabricated SIIG structure. . . . .	34
Figure 3.1	Exposed view of (a) actual Substrate Integrated Image Guide (SIIG) structure and (b) its equivalent model. . . . .	39
Figure 3.2	Extracted effective permittivity of the alumina substrate with different size of circular perforations. . . . .	43
Figure 3.3	Extracted dissipation factor of the alumina substrate with different size of circular perforations. . . . .	44
Figure 3.4	Modal analysis structures: (a) SIIG equivalent model, (b) the first stage sub-structure, and (c) the second stage sub-structure. . . . .	45
Figure 3.5	Extracted normalized phase constant of a few first modes of mentioned SIIG structures. . . . .	47
Figure 3.6	Attenuation constant of a few first modes of mentioned SIIG structures. . . . .	47
Figure 3.7	Extracted normalized phase constant of the fundamental mode of the mentioned SIIG structure with different substrate permittivity. . . . .	49
Figure 3.8	Extracted normalized phase constant of the fundamental mode of the mentioned SIIG structure with different substrate thickness. . . . .	50
Figure 3.9	Extracted normalized phase constant of the second order mode of the mentioned SIIG structure with different guiding channel width. . . . .	50

Figure 3.10	Extracted usable single mode bandwidth based on the unloaded Q-factor of the fundamental and second mode. . . . .	51
Figure 3.11	Extracted attenuation constant of the fundamental mode of the mentioned SIIG structure with different substrate dissipation factor. . . .	51
Figure 3.12	Extracted attenuation constant of the fundamental mode of the mentioned SIIG structure with different ground plane's conductivity. . . .	52
Figure 3.13	a) The fabricated SIIG structure fed by WR-5.1 waveguide, b) the fabricated alumina substrate having 5 rows of circular perforations, c) zoomed view of the guiding channel and adjacent perforated regions.	54
Figure 3.14	Measurement setup used to extract the S-parameters of the SIIG waveguide in WR-5.1 Band. . . . .	55
Figure 3.15	Simulated and measured insertion loss and return loss of the SIIG prototype in the WR-5.1 band. . . . .	55
Figure 3.16	a) The fabricated SIIG structure fed by WR-3.5 waveguide, b) the fabricated alumina substrate having 5 rows of circular perforations, c) zoomed view of the guiding channel and adjacent perforated regions.	56
Figure 3.17	Simulated and measured insertion loss and return loss of the SIIG prototype in the WR-3.5 band. . . . .	57
Figure 4.1	Exposed view of (a) Substrate-Integrated Image Guide (SIIG) structure and (b) Substrate-Integrated Metallic Image Guide (SIMIG) structure.	63
Figure 4.2	Field distribution of the fundamental mode (i.e., $E_{11}^y$ ) of the SIIG structure at the frequency of 150 GHz, (a) magnitude of the electric field along the guiding channel and (b) electric field distribution on the cross-section. . . . .	63
Figure 4.3	Extracted normalized phase constant of a few first modes of mentioned SIIG structures. . . . .	64
Figure 4.4	Wave impedance of a few first modes of mentioned SIIG structures. .	64
Figure 4.5	Field distribution of the $E_{11}^y$ mode of the SIMIG structure at the frequency of 190 GHz, (a) magnitude of the electric field along the guiding channel and (b) electric field distribution on the cross-section. . . . .	65
Figure 4.6	Extracted normalized phase constant of a few first modes of mentioned SIMIG structures. . . . .	66
Figure 4.7	Wave impedance of a few first modes of mentioned SIMIG structures.	67
Figure 4.8	Extracted normalized phase constant of the fundamental mode of mentioned SIMIG structure. . . . .	68

Figure 4.9	Extracted normalized phase constant of the second mode of mentioned SIMIG structure. . . . .	69
Figure 4.10	Field distribution of mentioned SIIG/SIMIG transition at the frequency of 200 GHz. . . . .	69
Figure 4.11	Extracted S-parameter of mentioned SIIG/SIMIG transition. . . . .	70
Figure 4.12	Extracted performance of the different technologies at a 60-degree bend. (a) insertion loss and (b) return loss . . . . .	72
Figure 4.13	Field distribution of different technology at a 60-degree bend at the frequency of 180 GHz, a) SIIG waveguide, b) proposed SIHDMIG waveguide along with tapering opening. . . . .	72
Figure 4.14	a) The fabricated hybrid waveguide featuring a 60 degree bend fed by WR-5.1 waveguide, b) the fabricated alumina substrate having 5 rows of circular perforations, c) zoomed view of the guiding channel and adjacent perforated regions. . . . .	73
Figure 4.15	Measurement setup used to extract the S-parameters of the SIHDMIG waveguide in WR-5.1 Band. . . . .	73
Figure 4.16	a) The fabricated hybrid waveguide featuring a 60 degree bend fed by WR-3.5 waveguide, b) the fabricated alumina substrate having 5 rows of circular perforations, c) zoomed view of the guiding channel and adjacent perforated regions. . . . .	74
Figure 4.17	Extracted performance of the different technologies at a 60-degree bend. (a) insertion loss and (b) return loss . . . . .	75
Figure 4.18	Field distribution of different technology at a 60-degree bend at the frequency of 180 GHz, a) SIIG waveguide, b) proposed SIHDMIG waveguide along with tapering opening. . . . .	76
Figure 4.19	a) The fabricated power divider/combiner fed by WR-5.1 waveguide, b) zoomed view of the guiding channel and adjacent perforated regions. . . . .	77
Figure 4.20	Extracted performance of the designed power divider/combiner in term of insertion/return loss. . . . .	77
Figure 4.21	Field distribution of the designed power divider/combiner at, a) 150 GHz , b) 175 GHz, and c) 190 GHz. . . . .	78
Figure 4.22	a) The fabricated power divider/combiner fed by WR-3.5 waveguide, b) zoomed view of the guiding channel and adjacent perforated regions. . . . .	79
Figure 4.23	Extracted performance of the designed power divider/combiner in term of insertion/return loss. . . . .	79

Figure 4.24	Field distribution of the designed power divider/combiner at, a) 235 GHz , b) 260 GHz, and c) 310 GHz. . . . .	80
Figure B.1	Computed real part of the cut-off frequency for the initial propagating modes. . . . .	101
Figure B.2	Computed imaginary part of the cut-off frequency for the initial propagating modes. . . . .	101
Figure B.3	Extracted effective permittivity of fundamental mode. . . . .	103
Figure B.4	Extracted effective dissipation factor of fundamental mode. . . . .	104
Figure C.1	Proposed unit-cell design in HFSS software. . . . .	111
Figure C.2	Defining periodic boundary condition along $y$ -direction. . . . .	112
Figure C.3	Defining periodic boundary condition along $x$ -direction. . . . .	112
Figure C.4	Defining periodic boundary condition along $z$ -direction. . . . .	113
Figure C.5	Defining the <i>Eigenmode</i> solver and parameters sweep. . . . .	113
Figure C.6	Defining the formulation for effective permittivity and effective dissipation factor. . . . .	114
Figure C.7	Extracted effective permittivity of the fundamental mode. . . . .	114
Figure C.8	Extracted effective dissipation factor of the fundamental mode. . . . .	115
Figure C.9	CST Suite Studio template configuration. . . . .	116
Figure C.10	<i>Eigenmode Solver</i> selection. . . . .	117
Figure C.11	Configuration of periodic boundary conditions. . . . .	118
Figure C.12	Configuring the <i>Eigenmode</i> solver and parameter sweeps. . . . .	118
Figure C.13	Extracted dispersion diagram of the fundamental mode using the CST Suite Studio. . . . .	119
Figure C.14	Extracted Q-factor of the fundamental mode using the CST Suite Studio. . . . .	119
Figure C.15	Extracted effective permittivity of the fundamental mode. . . . .	120
Figure C.16	Extracted effective dissipation factor of the fundamental mode. . . . .	120
Figure D.1	Difficulty encountered in fabricating SIIG waveguides on a Silicon wafer. . . . .	122
Figure D.2	The fabricated SIIG structure fed by rectangular waveguide. . . . .	123



## LIST OF SYMBOLS AND ABBREVIATIONS

SIIG	Substrate-Integrated Image Guide
THz	Terahertz
IBC	Impedance Boundary Condition
$\tan \delta$	Dissipation Factor
SIC	Substrate-Integrated Circuit
EM	Electromagnetic
SIMIG	Substrate-Integrated Metallic Image Guide
mmW	Millimeter-Wave
CPW	Coplanar Waveguide
SIW	Substrate-Integrated Waveguide
GCPW	Grounded Coplanar Waveguide
NRD	Non-Radiative Dielectric
SIHDMIG	Substrate-Integrated Hybrid Dielectric-Metallic Image Guide
PEC	Perfect Electric Conductor
TE	Transverse Electric
TM	Transverse Magnetic
V-Pol	Vertically Polarized
H-Pol	Horizontally Polarized
RW	rectangular waveguide
GW	Gap Waveguide
PMC	Perfect Magnetic Conductor
DRIE	Deep Reactive Ion Etching
SOI	Silicon-on-Insulator
DML	Dielectric Microstrip Line
SIDW	Substrate-Integrated Dielectric Waveguide
SINRD	Substrate-Integrated Non-Radiative Dielectric
Q-Factor	Quality Factor
EBG	Electromagnetic Band Gap
CBCPW	Cavity-backed Coplanar Waveguide

**LIST OF APPENDICES**

Appendix A	. . . . .	92
Appendix B	. . . . .	94
Appendix C	. . . . .	111
Appendix D	. . . . .	121
Appendix E	. . . . .	124

## CHAPTER 1 INTRODUCTION

### 1.1 Motivation

As shown in Fig. 1.1, the explosive growth in commercial applications in the terahertz (THz) bands of the electromagnetic spectrum including sub-THz ranges has set the stage for a transformative wave of technological advancement. This spectrum, spanning frequencies from 100 GHz to 10 THz, has witnessed a surge in applications such as personal communications, high-capacity wireless data links, automotive and aircraft radar systems, spectroscopy sensors, medical imaging, and security scanners [1]. These applications exploit the distinctive features of THz waves that include an extensive bandwidth, high spatial resolution with compact antennas, the ability to penetrate challenging environments like dust, smoke, or fog, resonance with critical atmospheric molecules, and access to previously untapped frequency resources.

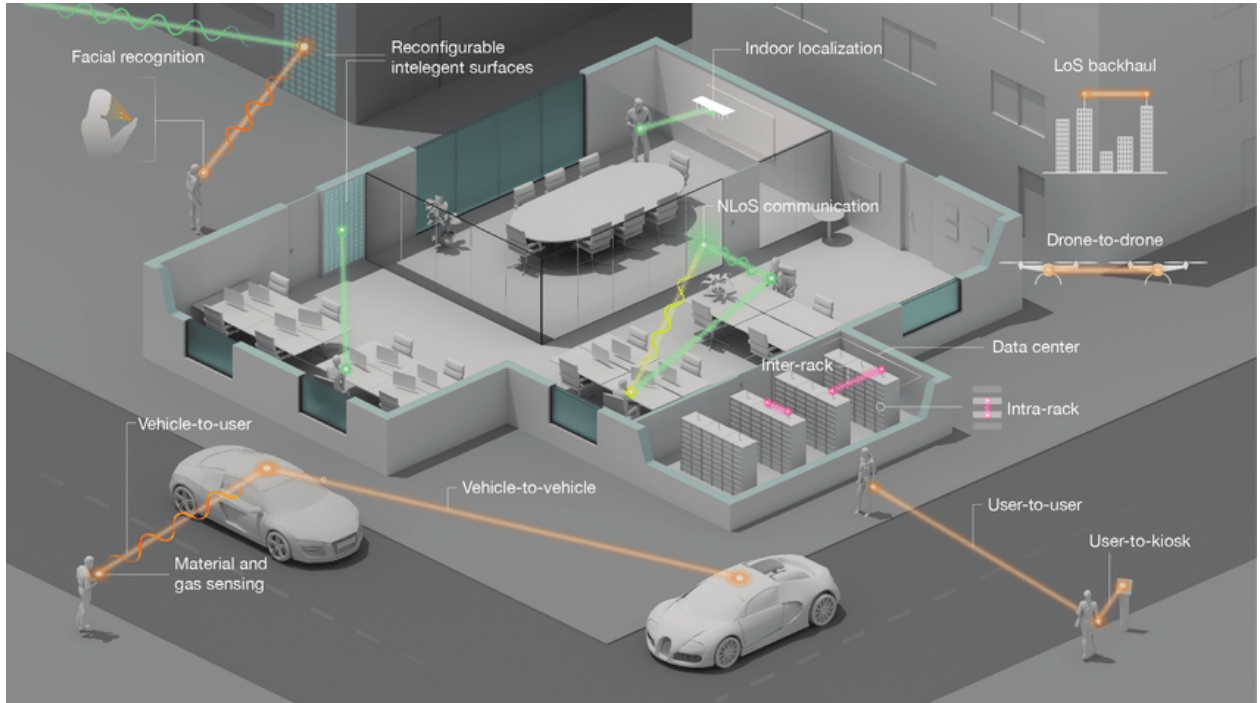


Figure 1.1 Prospective indoor and outdoor applications of sub-THz and THz communications [1].

This Ph.D. thesis is intrinsically motivated by the potential of sub-THz and THz technology to address a critical challenge within this burgeoning field. Our research is dedicated to the exploration and development of technology that promises minimal transmission loss and seamless interconnection with other circuit components. Furthermore, our aim is to enable the creation of highly compact integrated circuits that will play an essential role in the deployment of these transformative technologies.

In conclusion, this Ph.D. thesis is driven by the pressing need to harness the immense potential of sub-THz and THz technology to address real-world challenges and drive innovation. It is motivated by the vision of a future where the unique attributes of this electromagnetic spectrum will shape a new era of communication, sensing, and imaging, with profound implications for various industries and the global community.

## 1.2 Problem Statement

Achieving high-density integration is paramount for the mass production of cost-effective, compact, and lightweight commercial products. Fig. 1.2 illustrates various metallic-based transmission lines operating in the microwave frequency range. In the microwave range up to approximately 30 GHz, microstrip serves as the dominant integrated waveguide structure [5]. Its popularity stems from its simplicity, cost-effective fabrication through printed circuit technology, and the extensive design information available in accurate empirical formulas for use in circuit synthesis software.

However, in the millimeter-wave (mmW) frequencies, ranging from 30 GHz, coplanar waveguide (CPW) is often preferred over microstrip [6]. This preference arises because the microstrip line requires very thin substrates due to the potential for overmoding and power leakage into substrate modes. Additionally, achieving reliable ground connections through metallized vias becomes increasingly challenging.

CPW is suitable for the mmW range, but in the sub-THz/THz frequency range, inefficient wave guidance by metal-based waveguides remains a pervasive issue. The skin effect plays an increasing role, causing currents to flow in a thin region below the metal surface, while surface roughness becomes a critical factor. Furthermore, as frequencies rise, the cross-sectional dimensions of the guide must be scaled down to suppress higher-order modes and potential leakage or radiation. These factors result in high current densities and, consequently, significant conductor losses. The situation worsens for traditional integrated planar transmission lines like microstrip and CPW, as the existing electromagnetic field singularities at the conductor strip edges exacerbate the loss problem. Other well-developed metallic-based

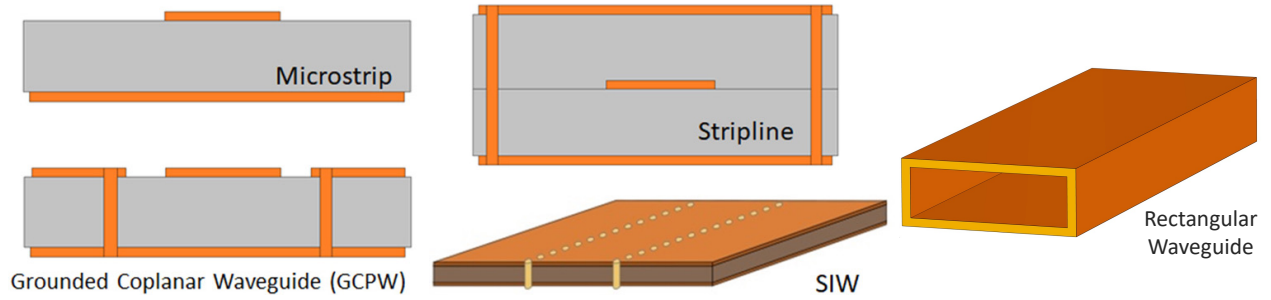


Figure 1.2 Different metallic-bases transmission lines [2].

technologies are the stripline transmission line [7] and the Substrate-Integrated Waveguide (SIW) [8], which are similar to the other metallic waveguides, also grapples with conductor losses.

In the past, researchers attempted to reduce dielectric losses in the substrate material through techniques such as micro-machining. However, conductor-related losses dominate and couldn't be significantly reduced. While this limitation is generally acceptable in miniature MMICs with very short transmission lines, it poses a significant challenge when designing larger passive devices such as antenna arrays, feeding networks, power dividers, combiners, directional couplers, phase shifters, resonators, and filters. Hence, the technology of choice for such components in the sub-THz/THz frequencies has traditionally been metallic rectangular waveguide due to its superior performance [9]. It exhibits low wave attenuation because the modal fields are well distributed over a relatively large air cross-section without any field singularities. Nonetheless, the drawbacks of rectangular waveguide technology include its high cost, bulkiness, and limited integrability.

As shown in Fig. 1.3, another well-established technology is the dielectric waveguide. The exploration of wave propagation on purely dielectric rods dates back to the early 20th century and was documented in a theoretical paper [10]. Subsequent experiments [11] and the development of a comprehensive theory demonstrating the existence of TE, TM, and hybrid modes [12] were published. The use of dielectric rod antennas became prevalent [13], and research into dielectric waveguides continued due to their appealing attributes of low signal loss and flexibility [14, 15].

Unlike metallic waveguides, where electromagnetic waves are guided through interactions with currents on conductors, dielectric waveguides function on the principle of total internal reflection at the dielectric-air interface. The actual wave guidance occurs at the surface of the dielectric material, leading to these waves being termed surface waves. A similar guidance effect is achieved when a denser dielectric material is enclosed by a material with lower

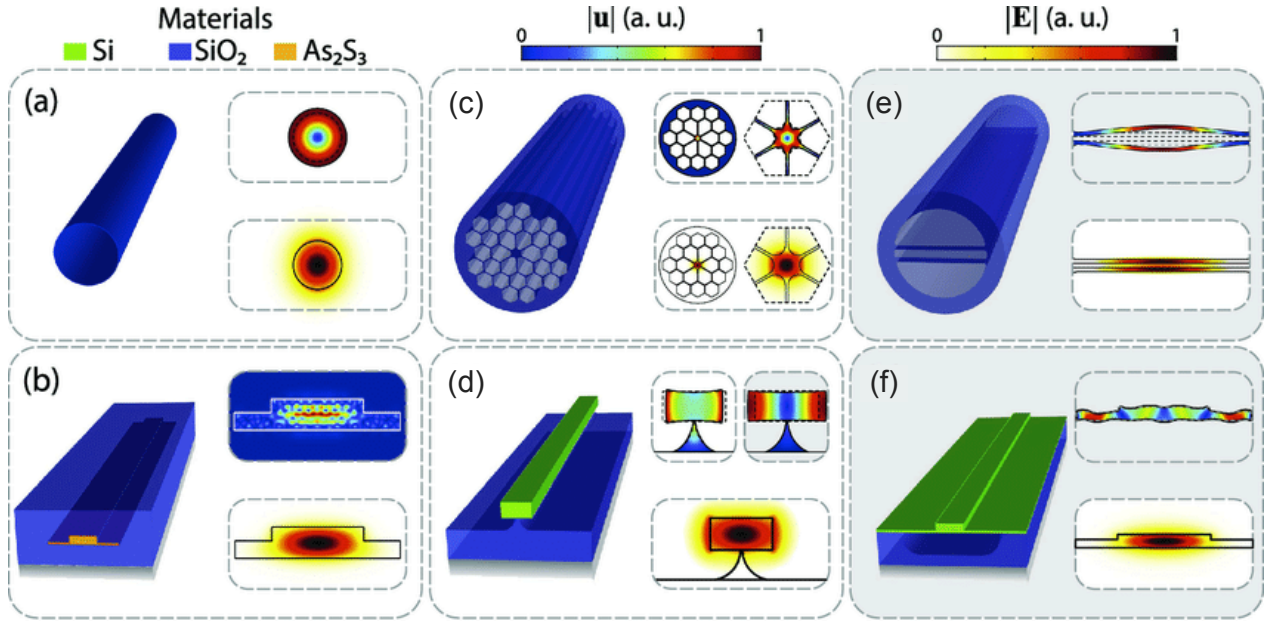


Figure 1.3 Dielectric and optical waveguides [3]. (a) Silica taper fiber, (b) integrated As<sub>2</sub>S<sub>3</sub> waveguide buried on SiO<sub>2</sub>, (c) silica photonic crystal fiber, (d) suspended silicon waveguide, (e) dual-nanoweb silica fiber, (f) suspended silicon waveguide membrane.

permittivity. The most notable success story in this realm is that of optical fibers, which transport signals in the form of electromagnetic waves in the optical range over incredibly long distances, paving the way for the Information Age, including the advent of the Internet.

While optical waveguides are typically composed entirely of dielectric materials, metallic elements are avoided due to the plasma-like characteristics of metals at optical wavelengths, which would introduce significant transmission losses [16]. Conversely, radio frequency and microwave technology has traditionally relied on metallic waveguide structures, as dielectric-based technologies struggle to achieve the necessary compactness and are more challenging to design.

As depicted in Fig. 1.4, the sub-THz/THz range resides between these two parts of the electromagnetic spectrum (i.e., the microwave region and the optical region), and it faces a technology gap. The absence of a practical technology prompted research into integrated dielectric waveguides. Notable examples include the image guide [17] and its rectangular strip variant [18], the inverted strip guide [19], the non-radiative dielectric (NRD) guide [20], and the inset guide [21]. While all these structures feature a metallic ground plane, their conductor losses are minimal because they lack the field singularities present in microstrip or CPW configurations, and their field concentration is relatively modest. Consequently, they can be viewed as hybrid metallic-dielectric waveguides, well-suited for bridging the gap

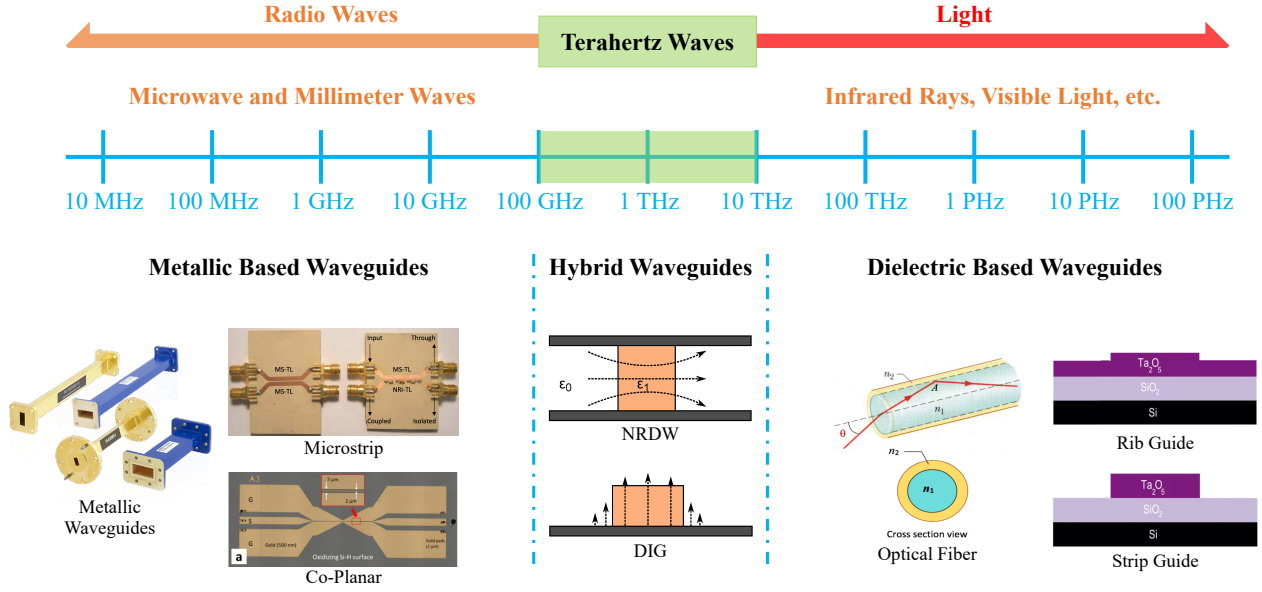


Figure 1.4 Technology gap between the microwave and optical region of the electromagnetic spectrum.

between the microwave and infrared/optical segments of the electromagnetic spectrum.

While wave guidance could theoretically occur without any conductor, incorporating a ground plane at sub-THz/THz frequencies offers several notable advantages. It serves as a sturdy mechanical support for the dielectric lines, acts as one-sided shielding, and can be utilized for biasing and dissipating heat generated by active devices [22]. Additionally, the ground plane has the effect of shifting higher-order and degenerate modes to higher frequencies, thereby expanding the usable single-mode bandwidth.

Among the integrated dielectric guides mentioned, the image guide stands out as one of the simplest and likely the most widely employed. It derives its name from the "mirror" effect created by the ground plane. King [17] primarily focused on the low-loss characteristics of the image guide with loosely bound waves, while Knox [18] concentrated on the rectangular, high-permittivity image guide with the aim of integration. In the case of the latter type, the insertion of an optional insulating dielectric film with low permittivity between the substrate and the metallic ground plane additionally reduces conductor losses [23]. Fig. 1.5a provides a visual representation of the resulting insulated image guide.

A diverse range of passive and active components, along with circuits, have been successfully implemented using image guide technology, underscoring the advantages of integrated dielectric technology. These applications include leaky-wave antennas [24], filters, couplers, and even a 94-GHz radar system [25]. Despite the image guide technology's decades-long

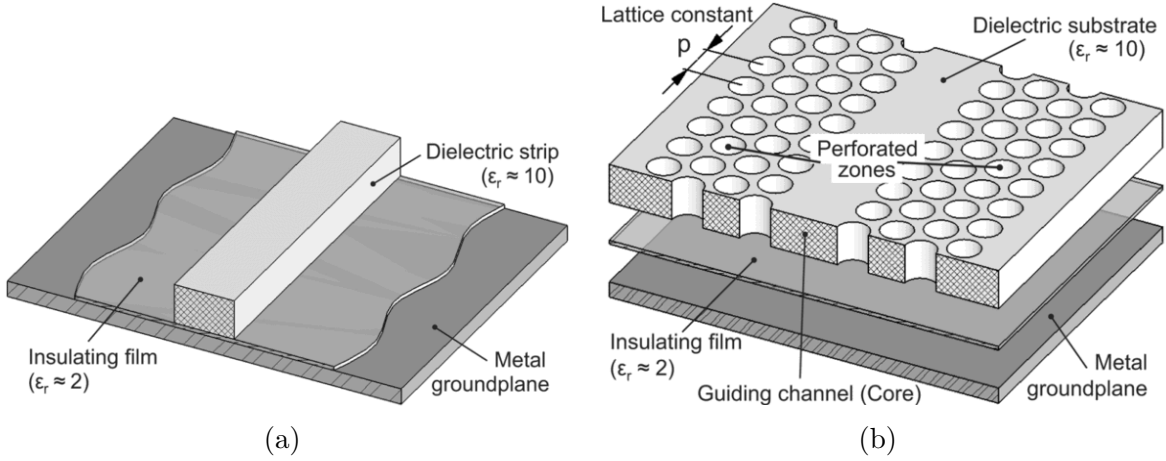


Figure 1.5 Exposed view of (a) insulated image guide and (b) exploded view of substrate integrated (insulated) image guide (SIIG) [4].

presence, it hasn't been extensively utilized in millimeter-wave (mmW) and sub-terahertz (sub-THz) integrated circuits. One primary obstacle has been the lack of mass-producible MMICs for this frequency range, which serve as the foundation for cost-effective commercial products today.

This landscape is gradually evolving, driven by technological advancements and the mounting pressure to explore higher frequency bands due to the scarcity of spectrum resources in the sub-THz/THz range. Although the standard image guide offers remarkable advantages with very low attenuation loss, it presents notable challenges in terms of integration and manufacturing. The small size of the individual dielectric strips, particularly at shorter wavelengths, necessitates precise placement onto the supporting metallic ground plane. Achieving stringent control over the image guide's dimensions and demanding alignment precision between the guides is imperative. Additionally, connecting image guide circuits to other transmission lines represents a significant limitation. Combining different technologies is challenging due to varying support requirements (e.g., ground plane versus dielectric substrate) and the exceptional precision demanded at sub-THz/THz frequencies, not to mention the multiple fabrication steps involved.

Inspired by the "substrate-integrated circuit" concept [26], Patrovsky et al. proposed a sanitized form of the image guide named "Substrate-Integrated Image Guide (SIIG)" [4]. Similar to the standard image guide, the SIIG consists of a planar high-permittivity substrate placed on a continuous metallic ground plane. To realize the permittivity contrast between the guiding channel and the bilateral regions, periodic air perforations are added to these regions, which artificially reduces the effective permittivity of these sections. Therefore, the



SIIG provides a similar guiding effect as the standard image guide, except for particularities caused by the periodic perforations. The planar substrate makes the fabrication process more accessible and provides a high alignment precision to the other integrated circuit components. Additionally, the interconnection with other waveguide technologies is substantially simplified on the same substrate.

The aforementioned SIIG structure [4], initially designed for millimeter-wave (mmW) applications up to 105 GHz, faces several significant challenges that hinder its broader utility and practical implementation. Firstly, the existing research lacks an analytical model for the SIIG structure, relying instead on data extracted from Ansys HFSS, an electromagnetic (EM) simulation software. This approach not only extends the design process but also limits the insight into the SIIG's behavior.

Secondly, a pronounced issue is the substantial substrate leakage that occurs at sharp discontinuities within the SIIG structure, particularly at sharp bends. This drawback poses a severe constraint on its application in highly compact integrated circuits, where signal integrity and minimal signal loss are paramount.

Additionally, while the optional insulating layer used in the SIIG structure does reduce transmission losses and mitigates field concentration near the metallic ground plane, it complicates the fabrication process and introduces challenges in terms of interconnecting the SIIG structure with other circuit components.

### 1.3 Research Objectives

To address the previously mentioned issues with the original SIIG structure, we have outlined the following objectives for this Ph.D. thesis:

#### 1. Development of an analytical model for accurate SIIG guiding performance analysis:

To gain a comprehensive understanding of the guiding performance of the SIIG structure, an analytical model must be established. The first step is to create an analytical method for extracting the effective properties (i.e., effective permittivity and dielectric loss) of the perforated regions accurately. This method utilizes periodic perforations within a lossy dielectric substrate and leverages *Floquet Theory* and *Fourier Series expansion* to solve an eigen-system problem related to electric field components. It provides precise calculations for cut-off frequencies, field distributions, effective permittivity, and dissipation factors for each propagating mode within these perforated regions.

The second method treats metallic plates as lossy conductors, incorporating the *Impedance Boundary Condition (IBC)* and accounting for a dielectric material's dissipation factor ( $\tan \delta$ ). This approach yields detailed information about the electromagnetic field distribution and propagation constants for modes in dielectric waveguides. Both methods are versatile and can be applied to various layered dielectric waveguides. These methods are suitable for modeling wave propagation across various frequency ranges and have been experimentally validated using a substrate-integrated image guide structure at 150 GHz, demonstrating their high accuracy in practical scenarios.

The completion of the first objective resulted in a published paper in the *IEEE Transactions on Microwave Theory and Techniques*:

- **Article 1: M. Moradi**, M. S. Sharawi, and K. Wu, "Analytical Model of Guided Waves in Periodically Perforated Dielectric Structures and Its Applications to Terahertz Substrate-Integrated Image Guides (SIIG)," *IEEE Transactions on Microwave Theory and Techniques*, 2023.

## 2. Design and fabrication of prototype SIIGs for sub-THz/THz frequency band:

The second objective is to utilize the developed analytical model to assess the suitability of substrate-integrated image guide technology (SIIG) for sub-THz/THz applications. In pursuit of this objective, we investigate the impact of structural parameters on the wave-guiding behavior of the SIIG. Removing the insulating layer streamlines the fabrication process and enhances integration potential with other circuit components in substrate-integrated circuit (SIC) applications. This eliminates the need for separate substrates and ground planes for different technologies, promoting compatibility and resource sharing. Two prototype waveguides, operating at frequencies of 150 GHz and 300 GHz, are fabricated using the optimal structural parameters. The responses of these fabricated waveguides are measured and compared with analytical methods and commercial electromagnetic software simulations. These comparisons reveal excellent agreement between the measurements and simulations, affirming the effectiveness and accuracy of the SIIG technology for THz applications.

The successful completion of the second objective leads to a published paper in the *IEEE Transactions on Terahertz Science and Technology*:

- **Article 2: M. Moradi**, M. S. Sharawi, and K. Wu, "Exploring Low-Loss Wide-band Substrate-Integrated Image Guides (SIIG) for Terahertz Applications," *IEEE Transactions on Terahertz Science and Technology*, 2023.

### 3. Substrate-integrated hybrid dielectric-metallic image guide (SIHDMIG) architecture and its applications in developing sub-THz/THz power divider:

While the SIIG waveguide exhibits exceptional performance in straight-line configurations, it faces challenges related to leakage at sharp bends. As a result, we have established our next objective to discover a solution that effectively resolves this issue of leakage. We introduce a novel waveguide, called the Substrate-Integrated Metallic Guide (SIMIG), which, when combined with SIIG, enables the creation of a hybrid waveguide known as the Substrate-Integrated Hybrid Dielectric-Metallic Image Guide (SIHDMIG) technology. SIHDMIG effectively mitigates wave leakage into the substrate and exhibits exceptional performance at sharp bends. The experimental results reveal that the proposed SIHDMIG structure enhances SIIG performance at sharp bends by 3 dB. Subsequently, we leverage this innovative technology to design a highly compact power divider/combiner. Based on the obtained results, the designed power divider/-combiner demonstrates superior performance across various frequency bands within the WR-5.1 and WR-3.5 frequency ranges.

## 1.4 Thesis Organization

In this thesis, we investigate and demonstrate the SIIG technology as a promising candidate for sub-THz/THz applications. Accordingly, the rest of the thesis is organized as follows:

Chapter 2 introduces the first article titled "Analytical Model of Guided Waves in Periodically Perforated Dielectric Structures and Its Applications to Terahertz Substrate-Integrated Image Guides (SIIG)". This paper presents and derives an analytical model for accurately analyzing lossy dielectric waveguides in the THz regime. By considering the dielectric loss of waveguides and applying the *Impedance Boundary Condition (IBC)*, the proposed method can accurately simulate the waveguiding behavior. By applying the *Fourier Series expansion* along with the *Floquet Theory*, an analytical model is developed which can effectively account for periodic perforations, which describes an inherent feature of substrate integrated dielectric waveguides at THz frequencies. The applicability and high accuracy of the proposed method are demonstrated by providing several examples and comparisons with measurements from a fabricated prototype. The efficiency of the proposed method in terms of simulation run-time is compared with some commercial EM software packages. These results demonstrate that while the proposed method maintains a minimum accuracy of 95% compared to the *CST Studio Suite* and *Ansys HFSS* software, the simulation run-time is reduced by 300 times.

Chapter 3 presents the second article with the title "Exploring Low-Loss Wideband Substrate-

Integrated Image Guides (SIIG) for Terahertz Applications". This paper proposes and explores high-performance Substrate-Integrated Image Guide (SIIG) techniques for THz applications. Due to its low-loss transmission, planar geometry, and metallic ground plane that can be shared among other circuit components, the SIIG structure is an ideal candidate for THz integrated circuits and systems development. By conducting modal analysis and selecting proper parameters for geometrical design considerations, the SIIG can provide the best possible performances in the THz regime. An alumina substrate is utilized to fabricate two SIIG prototypes for WR-5.1 and WR- 3.5 frequency bands. The experimental results show that one fabricated prototype exhibits a mean insertion loss of 0.578 dB/cm over a frequency range of 135 GHz – 225 GHz using a dual-line parameter extraction technique. The other fabricated prototype of SIIG presents an average insertion loss of 1.431 dB/cm in the frequency range of 215 GHz – 335 GHz. Those results demonstrate a promising potential of the SIIG techniques for THz applications. A detailed description of an SIIG structural analysis and also its design procedure are provided.

Chapter 4 delves into the third article with the title "Substrate-Integrated Hybrid Dielectric-Metallic Image Guide (SIHDMIG) Architecture and Its Applications in Developing sub-THz/THz Power Divider." This paper introduces a novel hybrid waveguide architecture designed to mitigate substrate leakage in the substrate-integrated image guide (SIIG) structure when confronted with sharp bends. This innovative approach combines elements of SIIG waveguides and substrate-integrated metallic image guide (SIMIG) waveguides to tailor specific design components based on the transmission properties of each waveguide type. We investigate and experimentally validate back-to-back WR-5.1 and WR-3.5 band prototypes constructed using this hybrid scheme. The proposed method demonstrates a 3 dB improvement in SIIG performance at a 60-degree bend, which is confirmed through the fabrication and measurement of the prototypes. This architecture is leveraged to create highly compact substrate-integrated power dividers/combiners. The presented hybrid waveguide architecture showcases its potential for the development of low-loss, highly integrated sub-terahertz (sub-THz) and terahertz (THz) circuits and systems.

Ultimately, this thesis is brought to a close in Chapter 5, where we summarize our contributions and accomplishments. Furthermore, this chapter offers recommendations for potential improvements to this research and suggests avenues for future work.

Before delving deeply into the following projects, namely, developing an analytical model, designing SIIGs for WR-5.1 and WR-3.5 frequency bands, preventing leakage, and designing the power divider, it is crucial to note that, given that each project addresses distinct topics, a comprehensive literature review specific to each project is included in their respective

sections.

# **CHAPTER 2    ARTICLE 1: ANALYTICAL MODEL OF GUIDED WAVES IN PERIODICALLY PERFORATED DIELECTRIC STRUCTURE AND ITS APPLICATIONS TO TERAHERTZ SUBSTRATE-INTEGRATED IMAGE GUIDE (SIIG)**

Mohammad Moradi, Mohammad S. Sharawi, Ke Wu

Published in: IEEE Transactions on Microwave Theory and Techniques

Publication date: March 29, 2023

## **2.1 Introduction**

Everything around us is becoming smarter as wireless communications and sensing technologies proliferate everywhere, from smart-phones and smart-watches to smart homes and autonomous vehicles [27]. Due to the exponential growth in the number of end-users of wireless communication systems, the communication channel is becoming increasingly congested. On the other hand, the development of high-resolution imaging applications [28], molecular-sensitive spectroscopic devices [29], and the increasing demand for ultra-broadband wireless data transmission in multi-user systems gather much attention towards high-frequency integrated circuits. Shortly, it is expected that a large number of wireless sensors and communication devices will be ubiquitously deployed and used immediately with the upcoming 6G technology. Thus, the system framework must be extremely highly integrated due to a limited space allocated for installing a massive number of sensors and communication components. THz technologies are proving to be the key to overcoming these underlying issues [9].

While sharing the same fundamental principles as microwaves, THz communication faces many challenges. One of them is the transmission loss in front-ends, which is often substantial in the THz regime. Specifically, the conductive loss will increase significantly as frequency increases, and the skin effect aggravates this loss; consequently, attenuation reaches several tens of dB/cm [30–32]. Therefore, conventional metal-based technologies (e.g., microstrip, coplanar, and substrate integrated waveguide (SIW)) may not be practical in THz band circuit and antenna applications. Dielectric waveguides, which are widely used in photonic circuits, exhibit excellent potential in developing THz circuits and antennas due to the absence of metallic loss, at least partially.

Typically, a high contrast between the permittivity of the guiding channel and adjacent regions should be realized to achieve the highest possible power transmission along dielectric

waveguides [33]. Adding perforations can artificially reduce the permittivity of the adjacent regions and realize this required contrast [4]. Analyzing these perforated regions is essential for developing an analytical model of dielectric waveguides. In all existing methods, this effective permittivity is considered to be purely real (i.e., lossless dielectric materials) and mainly calculated based on huge computationally intensive numerical methods [34–38]. These methods showed promising results but with a complicated procedure and expensive computation. On the other hand, approximate and empirical formulations for the effective permittivity of the perforated part were given in [39]; however, these empirical formulations might lead to inaccurate estimations for the design parameters and, accordingly, imprecise results. Moreover, the need for polarization diversity in enhancing the microwave and THz component efficiency [40–42] makes it essential to accurately analyze different polarizations of the electric field components.

Although wave guidance would be possible in the absence of any conductors [43–45], using a ground plane at THz frequencies has several significant advantages. It provides appropriate mechanical support for the dielectric lines, acts as a one-sided shielding, and can be used for biasing and dissipating heat from active devices if any [46]. Furthermore, the ground plane shifts higher-order and degenerate modes to higher frequencies, thus increasing the useable single-mode bandwidth. Since all existing analytical methods are developed for low frequencies, the metallic plates used within them were considered lossless perfect conducting layers [47, 48]. Accordingly, the perfect electric conductor (PEC) boundary conditions were applied wherever these plates were placed. As mentioned before, the conductive loss will increase significantly as frequency increases [49]; hence, the existing models do not provide accurate results in the THz regime.

This work is set to propose and develop two analytical methods for modeling lossy dielectric waveguides: 1) by considering the adjacent regions to have periodic perforations in a lossy dielectric substrate and applying the *Floquet Theory* [50] and *Fourier Series* [51] expansion, we achieved an eigensystem problem for electric field components. Solutions to this eigensystem problem will provide each propagating mode’s cut-off frequency and field distribution. The effective permittivity and dissipation factor of each mode can be accurately extracted from the calculated cut-off frequencies. This method can be effectively used to accurately model wave propagation along lossy dielectric materials with periodic perforations. 2) by considering the metallic plates as lossy conductors, applying the *Impedance Boundary Condition (IBC)* [52], and assuming the dissipation factor ( $\tan \delta$ ) for all dielectric materials, we completed a modified modal analysis that provides exact information on the electromagnetic field distribution and propagation constant of the propagating modes along the dielectric waveguides. This method can be effectively applied to all layered dielectric waveguides, including

strip dielectric guide, insulated image guide, and strip-slab guide.

The proposed methods' accuracy, applicability, and efficiency are demonstrated through comparison with the commercial EM software (e.g., *CST Studio Suite* and *Ansys HFSS*) simulations and a fabricated waveguide prototype. Excellent agreement between the developed analytical models and full-wave simulations is achieved while the simulation run-time is reduced significantly. It is worth mentioning that the proposed methods can model the wave propagation along layered dielectric waveguides in all frequency ranges. However, because of the fabrication limitation and material availability at the *Poly-Grames Research Center*, a substrate-integrated image guide (SIIG) structure for an operating frequency of 150 GHz was fabricated. Comparison with the fabricated SIIG waveguide as an experimental prototype demonstrated that the proposed method has high accuracy in realistic scenarios.

Accordingly, the rest of the chapter is organized as follows: Section 2.2 presents the development of an analytical method that accurately extracts the effective permittivity and loss of periodic perforated waveguide out of a lossy dielectric substrate. Section 2.3 demonstrates the procedure of modifying a modal analysis to account for the dielectric and metallic losses in dielectric waveguides. The accuracy, efficiency, and applicability of the proposed method are demonstrated by providing comparisons of simulations with two commercial EM software and of measurements through a fabricated prototype SIIG structure in Section 2.4. A brief conclusion is presented in Section 2.5, and some required detailed derivations are provided in the Appendix section.

## 2.2 Effective Permittivity Extraction

Developing the proposed analytical method can begin with the wave equation for electric field [53]. In dielectric waveguide applications, we consider having variation only in the medium's permittivity ( $\varepsilon_r$ ), while the permeability ( $\mu_r$ ) in the analysis domain is considered constant. Accordingly, for a source-free and lossy dielectric medium, the wave-equation can be written in the frequency domain as [53]:

$$\nabla^2 \mathbf{E} + k_0^2 \varepsilon_{r(x,y)} \mathbf{E} = 0 \quad (2.1)$$

where  $k_0$  is the free-space wave-number equal to  $k_0 = \omega \sqrt{\mu_0 \varepsilon_0}$ . The magnetic field wave-equation can be written in the frequency domain as [53]:

$$\nabla \times \left( \frac{1}{\varepsilon_{r(x,y)}} \nabla \times \mathbf{H} \right) + k_0^2 \mathbf{H} = 0 \quad (2.2)$$



As demonstrated in Fig. 2.1, we consider having a periodic structure along the  $x$  and  $y$  directions. For the  $TM_z$  modes, the electric field only has an axial component (i.e.,  $E_z$ ) [53], and based on the *Plane-wave expansion* method [54] and the *Floquet Theory* [50], we have:

$$\mathbf{E}(x, y, z) = \hat{\mathbf{z}}E_z(x, y) = \hat{\mathbf{z}}E_p(x, y)e^{-jk_{x_0}x}e^{-jk_{y_0}y} \quad (2.3)$$

where  $E_p(x, y)$ ,  $k_{x_0}$ , and  $k_{y_0}$  are the periodic electric field in the  $xy$ -plane, propagation constant along the  $x$ , and  $y$  directions, respectively. Assuming the structure has a periodicity of  $a$  along the  $x$  direction and  $c$  along the  $y$  direction, and using the *Fourier Series* expansion [51];  $E_p(x, y)$  can be formulated as:

$$E_p(x, y) = \sum_n \sum_q a_{(n,q)} e^{-j\frac{2\pi n}{a}x} e^{-j\frac{2\pi q}{c}y} \quad (2.4)$$

where  $a_{(n,q)}$  is an unknown *Fourier* coefficient.

Similar to the previous formulation, the permittivity of the structure can be expressed as:

$$\varepsilon_{r(x,y)} = \sum_m \sum_p b_{(m,p)} e^{-j\frac{2\pi m}{a}x} e^{-j\frac{2\pi p}{c}y} \quad (2.5)$$

It is necessary to mention that the number of summed terms (i.e.,  $n$ ,  $q$ ,  $m$ , and  $p$ ) defines the accuracy of the approximation. To be specific, more summed terms produces more accurate results. These variables should be an integer number ranging from  $-N$  to  $N$ .

As shown in Fig. 2.1, the structure has variations only along the  $x$  and  $y$  directions. Accordingly, the wave-equation (2.1) can be expanded as:

$$\frac{\partial^2}{\partial x^2} E_z(x, y) + \frac{\partial^2}{\partial y^2} E_z(x, y) + k_0^2 \varepsilon_{r(x,y)} E_z(x, y) = 0 \quad (2.6)$$

Substituting (2.4) and (2.5) into (2.6), leads to:

$$\begin{aligned} \sum_n \sum_q \left[ \left( \frac{2\pi n}{a} + k_{x_0} \right)^2 + \left( \frac{2\pi q}{c} + k_{y_0} \right)^2 \right] a_{(n,q)} \\ e^{-j\frac{2\pi n}{a}x} e^{-j\frac{2\pi q}{c}y} = k_0^2 \sum_m \sum_p b_{(m,p)} e^{-j\frac{2\pi m}{a}x} e^{-j\frac{2\pi p}{c}y} \\ \sum_n \sum_q a_{(n,q)} e^{-j\frac{2\pi n}{a}x} e^{-j\frac{2\pi q}{c}y} \end{aligned} \quad (2.7)$$

after doing some simplifications (more details are provided in Appendix A), the above equa-

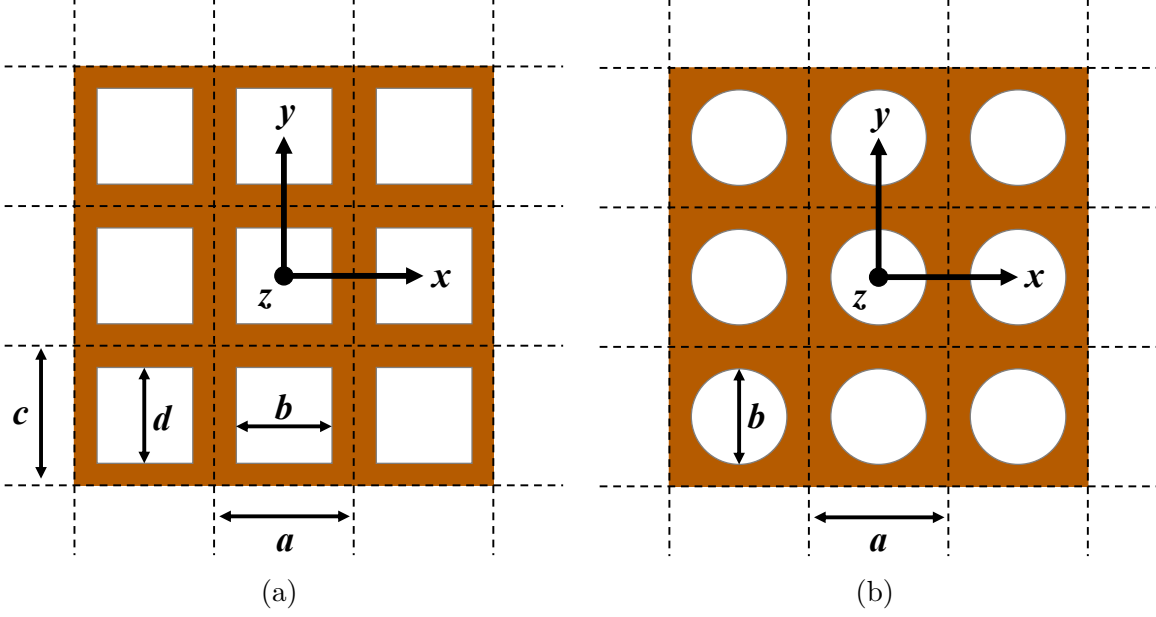


Figure 2.1 Cross-sectional view of a two-dimensional array of (a) rectangular and (b) circular perforations in a dielectric substrate.

tion reforms to the following eigenvalue equation:

$$a_{(n,q)} \left[ \left( \frac{2\pi n}{a} + k_{x_0} \right)^2 + \left( \frac{2\pi q}{c} + k_{y_0} \right)^2 \right] = k_0^2 \sum_m \sum_p a_{(m,p)} b_{(n-m, q-p)} \quad (2.8)$$

A careful review of the above equation reveals two unknown variables (i.e.,  $a_{(i,j)}$ , and  $b_{(i,j)}$ ). However,  $b_{(i,j)}$  can be found by applying the *Fourier Series* coefficient on a unit-cell as:

$$b_{(i,j)} = \varepsilon_r \delta_{(i,j)} - (\varepsilon_r - 1) \frac{bd}{ac} \text{sinc} \left( \frac{\pi ib}{a} \right) \text{sinc} \left( \frac{\pi jd}{c} \right) \quad (2.9)$$

where  $b$ ,  $d$ , and  $\delta_{(i,j)}$  are the perforation sizes along the  $x$ , and  $y$  directions, and the *Kronecker Delta* function, respectively. The relative permittivity ( $\varepsilon_r$ ) of a lossy dielectric medium can be expressed in a complex form as  $\varepsilon_r = \varepsilon' - j\varepsilon''$ , in which the ratio of the imaginary and the real parts defines the tangent of dielectric loss angle (i.e.,  $\tan \delta$ ) [55].

It is worth mentioning that the formulation of  $b_{(i,j)}$  will be changed for different perforation patterns. To demonstrate this fact, we consider and begin with circular perforations having the diameter of  $b$  and periodicity of  $a$  (as shown in Fig. 2.1b). The corresponding  $b_{(i,j)}$  can

be calculated as:

$$b_{(i,j)} = \varepsilon_r \delta_{(i,j)} - (\varepsilon_r - 1) \frac{\pi b^2}{a^2} \frac{2J_1 \left( \sqrt{\left(\frac{2\pi ib}{a}\right)^2 + \left(\frac{2\pi jb}{a}\right)^2} \right)}{\sqrt{\left(\frac{2\pi ib}{a}\right)^2 + \left(\frac{2\pi jb}{a}\right)^2}} \quad (2.10)$$

where  $J_1$  is the *Bessel function of the first kind*.

By substituting (2.9) (or (2.10)) into (2.8), it turns into a generalized linear eigensystem problem. Equation (2.8) can be put in a matrix form as:

$$\begin{bmatrix} \mathbf{A} \end{bmatrix}_{nq \times nq} \begin{bmatrix} \mathbf{a} \end{bmatrix}_{nq \times 1} = k_0^2 \begin{bmatrix} \mathbf{B} \end{bmatrix}_{nq \times mp} \begin{bmatrix} \mathbf{a} \end{bmatrix}_{mp \times 1} \quad (2.11)$$

The above equation can be transformed into an ordinary eigen-equation as follows:

$$k_0^{-2} \begin{bmatrix} \mathbf{a} \end{bmatrix}_{nq \times 1} = \underbrace{\begin{bmatrix} \mathbf{A} \end{bmatrix}_{nq \times nq}^{-1} \begin{bmatrix} \mathbf{B} \end{bmatrix}_{nq \times mp}}_{\begin{bmatrix} \mathbf{C} \end{bmatrix}} \begin{bmatrix} \mathbf{a} \end{bmatrix}_{mp \times 1} \quad (2.12)$$

According to the eigen-equation (2.12), the eigenvalues of matrix  $[\mathbf{C}]$  are equal to  $k_0^{-2}$ , which can provide us with the cut-off frequencies of  $TM_z$  propagating modes. We can calculate the effective permittivity of each corresponding mode from its cut-off frequency. In other words, we should specify the wavenumber (i.e.,  $k_{x_0}$  and  $k_{y_0}$ ) and calculate the corresponding eigenvalue. The effective permittivity and effective loss factor of each mode can be calculated as [55]:

$$\varepsilon'_{\text{eff}} = \left( \frac{c_0}{2\pi} \frac{\partial k_0}{\partial \Re\{f\}} \right)^2 \quad (2.13)$$

$$\varepsilon''_{\text{eff}} = \left( \frac{c_0}{2\pi} \frac{\partial k_0}{\partial \Im\{f\}} \right)^2 \quad (2.14)$$

where  $c_0$ ,  $k_0$ ,  $\Re\{f\}$ , and  $\Im\{f\}$  are the speed of light, defined wavenumber, real and imaginary part of extracted cut-off frequency, respectively. The eigenvector of matrix  $[C]$  will provide the field distribution of each mode inside the unit-cell.

For the  $TE_z$  modes, the magnetic field only has an axial component (i.e.,  $H_z$ ), and again based on the *Plane-wave expansion* method and the *Floquet Theory*, we have:

$$\mathbf{H}(x, y, z) = \hat{\mathbf{z}}H_z(x, y) = \hat{\mathbf{z}}H_p(x, y)e^{-jk_{x_0}x}e^{-jk_{y_0}y} \quad (2.15)$$

where  $H_p(x, y)$  is the periodic magnetic field in the  $xy$ -plane. Using the *Fourier Series*,  $H_p(x, y)$  can be formulated as:

$$H_p(x, y) = \sum_n \sum_q a_{(n,q)} e^{-j\frac{2\pi n}{a}x} e^{-j\frac{2\pi q}{c}y} \quad (2.16)$$

where  $a_{(n,q)}$  is an unknown coefficient. Checking (2.2) reveals that we have to formulate  $1/\varepsilon_r$  using the *Fourier Series* as:

$$\frac{1}{\varepsilon_r(x,y)} = \sum_m \sum_p b_{(m,p)} e^{-j\frac{2\pi m}{a}x} e^{-j\frac{2\pi p}{c}y} \quad (2.17)$$

Expanding (2.2), and substituting (2.16) and (2.17) into it leads to the following eigenvalue equation:

$$\begin{aligned} k_0^2 a_{(n,q)} = & - \sum_m \sum_p a_{(m,p)} b_{(m,p)} \left[ \left( \frac{2\pi n}{a} + k_{x_0} \right)^2 \right. \\ & + \left( \frac{2\pi q}{c} + k_{y_0} \right)^2 - \frac{2\pi(n-m)}{a} \left( \frac{2\pi n}{a} + k_{x_0} \right) \\ & \left. - \frac{2\pi(q-p)}{c} \left( \frac{2\pi q}{c} + k_{y_0} \right) \right] \end{aligned} \quad (2.18)$$

A careful review of the above equation reveals two unknowns (i.e.,  $a_{(i,j)}$  and  $b_{(i,j)}$ ). However, for a rectangular perforation,  $b_{(i,j)}$  can be achieved by applying the *Fourier Series* coefficient on a unit-cell as:

$$b_{(i,j)} = \frac{1}{\varepsilon_r} \delta_{(i,j)} - \left( \frac{1}{\varepsilon_r} - 1 \right) \frac{bd}{ac} \text{sinc} \left( \frac{\pi ib}{a} \right) \text{sinc} \left( \frac{\pi jd}{c} \right) \quad (2.19)$$

for the circular perforation,  $b_{(i,j)}$  can be calculated as:

$$b_{(i,j)} = \frac{1}{\varepsilon_r} \delta_{(i,j)} - \left( \frac{1}{\varepsilon_r} - 1 \right) \frac{\pi b^2}{a^2} \frac{2J_1 \left( \sqrt{\left( \frac{2\pi i b}{a} \right)^2 + \left( \frac{2\pi j b}{a} \right)^2} \right)}{\sqrt{\left( \frac{2\pi i b}{a} \right)^2 + \left( \frac{2\pi j b}{a} \right)^2}} \quad (2.20)$$

By substituting (2.19) (or (2.20)) into (2.18), it turns into an ordinary eigensystem problem, which can be put in a matrix form like:

$$k_0^2 \begin{bmatrix} \mathbf{a} \\ \end{bmatrix}_{nq \times 1} = \begin{bmatrix} \mathbf{D} \\ \end{bmatrix}_{nq \times mp} \begin{bmatrix} \mathbf{a} \\ \end{bmatrix}_{mp \times 1} \quad (2.21)$$

According to the eigen-equation (2.21), eigenvalues of matrix  $[D]$  are equal to  $k_0^2$  which can provide us with the cut-off frequencies of  $TE_z$  propagating modes. The eigenvector of matrix  $[D]$  will provide the field distribution of each mode inside the unit-cell. This procedure is similar to the case of  $TM_z$  modes as described above.

### 2.3 Modal Analysis

Accurate extraction of the effective permittivity and dissipation factor of the perforated regions enables us to use an equivalent model instead of the original SIIG structure. As shown in Fig. 2.2, an equivalent model can be constructed by replacing the perforated regions with equivalently uniform dielectric layers with relative permittivity equal to the calculated effective permittivity. It is worth mentioning that the effective permittivity and dissipation factor of the perforated regions are highly dispersive (i.e., resulting effective permittivity and dissipation factor changes with frequency). Therefore, values of the effective permittivity and dissipation factor should be selected according to the corresponding frequency. We can use this equivalent structure for the next step and apply the proposed modal analysis to extract all propagating modes through the guiding channel.

As shown in Fig. 2.3a, the equivalent model has material variation in two directions (here  $x$ , and  $y$  directions). The proposed method uses the *effective dielectric constants* approach to extract the propagating modes [18]. This approach splits the original structure into two simple sub-structures, which can be analyzed much more straightforwardly. The first sub-structure is considered to have material variation only along the  $y$  direction, as shown in

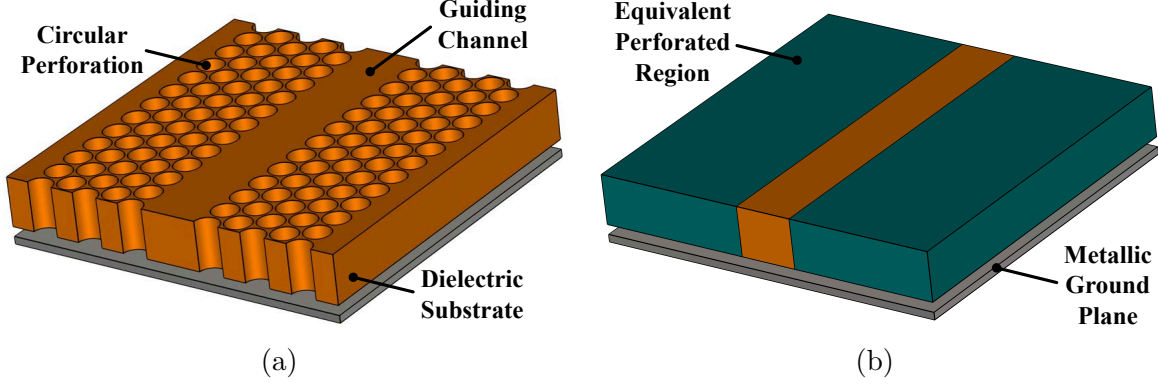


Figure 2.2 Exposed view of (a) actual Substrate Integrated Image Guide (SIIG) structure and (b) its equivalent model.

Fig. 2.3b. The effective dielectric constant of this combination (i.e., the dielectric layer plus the top free-space layer) and the propagation constant along the  $y$  direction (i.e.,  $k_y$ ) will be extracted through the first stage. In the second stage, this combination will be replaced by a single uniform layer with relative permittivity equal to the extracted effective dielectric constant, that enables us to calculate the propagation constant along the  $x$  direction (i.e.,  $k_x$ ). Having the propagation constants along the  $x$  and  $y$  directions allows us to calculate the propagation constant along the  $z$  direction.

### 2.3.1 Extracting $k_y$

SIIG structure and its equivalent waveguide can support wave propagation in two possible field configurations:  $E_{pq}^y$  (vertically polarized) and  $E_{pq}^x$  (horizontally polarized) modes. The subscripts  $p$  and  $q$  indicate the number of electric field extrema along the  $x$ , and  $y$  directions, respectively.

Maxwell curl equations can be solved in terms of two scalar parameters, named the *Electric Scalar Potentials*  $\phi^e$  and the *Magnetic Scalar Potentials*  $\phi^h$  as [56]:

$$E_x = \frac{1}{\varepsilon_{r(x,y)}} \frac{\partial^2 \phi^e}{\partial y \partial x} + \omega \mu_0 k_z \phi^h \quad (2.22a)$$

$$E_y = \frac{1}{\varepsilon_{r(x,y)}} \left( k_z^2 - \frac{\partial^2}{\partial x^2} \right) \phi^e \quad (2.22b)$$

$$E_z = \frac{-jk_z}{\varepsilon_{r(x,y)}} \frac{\partial \phi^e}{\partial y} - j\omega \mu_0 \frac{\partial \phi^h}{\partial x} \quad (2.22c)$$

$$H_x = -\omega \varepsilon_0 k_z \phi^e + \frac{\partial^2 \phi^h}{\partial y \partial x} \quad (2.22d)$$

$$H_y = \left( k_z^2 - \frac{\partial^2}{\partial x^2} \right) \phi^h \quad (2.22e)$$

$$H_z = j\omega\varepsilon_0 \frac{\partial \phi^e}{\partial x} - jk_z \frac{\partial \phi^h}{\partial y} \quad (2.22f)$$

where  $\varepsilon_{r(x,y)}$  and  $k_z$  are the relative permittivity of the medium and the propagation constant along the  $z$  direction, respectively. It is worth mentioning that  $\varepsilon_{r(x,y)}$  is a complex number that includes the permittivity and dielectric loss information. A review of the equations mentioned earlier indicates that vertical modes  $E_{pq}^y$  have principal electric field component along the  $y$  direction (i.e.,  $E_y$ ) and magnetic field component along the  $x$  direction (i.e.,  $H_x$ ). Setting  $\phi^h = 0$  provides much simpler equations for the electric and magnetic field components of these modes. This simplification reduces the accuracy of solutions; however, analyses and simulations (which will be discussed in the next section) demonstrate an acceptable accuracy for the proposed method. Accordingly, (2.22) can be simplified to:

$$E_x = \frac{1}{\varepsilon_r(y)} \frac{\partial^2 \phi^e}{\partial y \partial x} \quad (2.23a)$$

$$E_y = \frac{1}{\varepsilon_r(y)} \left( k_z^2 - \frac{\partial^2}{\partial x^2} \right) \phi^e \quad (2.23b)$$

$$E_z = \frac{-jk_z}{\varepsilon_r(y)} \frac{\partial \phi^e}{\partial y} \quad (2.23c)$$

$$H_x = -\omega\varepsilon_0 k_z \phi^e \quad (2.23d)$$

$$H_y = 0 \quad (2.23e)$$

$$H_z = j\omega\varepsilon_0 \frac{\partial \phi^e}{\partial x} \quad (2.23f)$$

For the structure shown in Fig. 2.3b, most of the power will propagate through the dielectric slab, which is considered to have higher permittivity than the free-space (i.e.,  $\varepsilon_1, \varepsilon_2 > \varepsilon_0$ ). Accordingly, electric scalar potential  $\phi^e$  should have sinusoidal distribution in the dielectric layer and exponentially decay in the free-space. Thus,  $\phi^e$  can be formulated as:

$$\begin{aligned} \phi^e(y) &= A_1^c \cdot \cos(k_y y) + A_1^s \cdot \sin(k_y y), & 0 \leq y \leq y_1 \\ \phi^e(y) &= B_1 \cdot e^{-\eta_0(y-y_1)}, & y \geq y_1 \end{aligned} \quad (2.24)$$

where  $\eta_0 = \sqrt{\mu_0/\varepsilon_0}$  is the free-space impedance. The propagation constant in different layers can be formulated by the following relation:

$$k_{zd}^2 = \varepsilon_0 k_0^2 + \eta_0^2 = \varepsilon_1 k_0^2 - k_y^2 \quad (2.25)$$

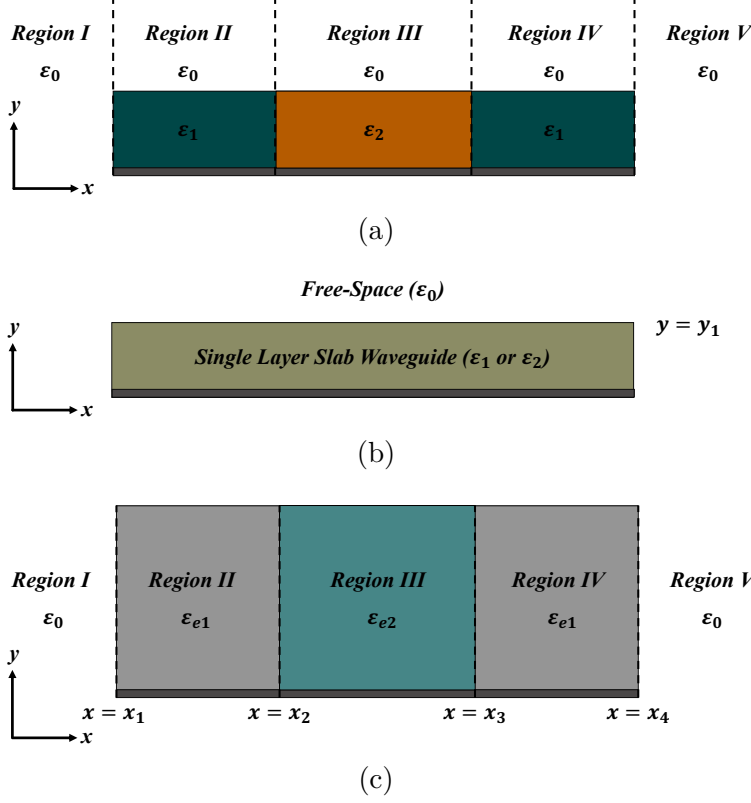


Figure 2.3 Modal analysis structures: (a) SIIG equivalent model, (b) the first stage sub-structure, and (c) the second stage sub-structure.

where  $k_y$  and  $k_{zd}$  are the propagation constants along the  $y$  and  $z$  directions inside the dielectric layer.  $A_1^c$ ,  $A_1^s$ , and  $B_1$  are unknown constants that can be determined by applying the boundary conditions. As seen in Fig. 2.3b, a metallic ground plane is placed at the bottom of the structure. Typically, this ground plane is considered a *Perfect Electric Conductor (PEC)* at low frequencies. However, the conductor losses have considerable values at high frequencies and should not be ignored. Therefore, the proposed method considers the ground plane a lossy metallic layer, and the *Impedance Boundary Condition (IBC)* is applied [52]. This boundary condition can be expressed as:

$$\mathbf{E}_t + \eta_m [\mathbf{H}_t \times \hat{\mathbf{n}}] = 0 \quad (2.26)$$

and

$$\eta_m = \sqrt{\frac{j\omega\mu_m}{\sigma_m + j\omega\epsilon_m}} \quad (2.27)$$

where  $\mu_m$ ,  $\epsilon_m$ , and  $\sigma_m$  are the permeability, permittivity, and the conductivity of the metal, respectively, and  $\hat{\mathbf{n}}$  is the unit vector that is normal to the metal surface. Applying this



condition on (2.23) at  $y = 0$  leads to:

$$A_1^s = \frac{\eta_m \varepsilon_1}{k_y} A_1^c \quad (2.28)$$

Matching the tangential electric and magnetic fields components (i.e.,  $E_z$ ,  $H_x$ ) at  $y = d$  yields:

$$\frac{k_y}{\varepsilon_1} (A_1^s \cdot \cos(k_y \cdot d) - A_1^c \cdot \sin(k_y \cdot d)) = \frac{-\eta_0}{\varepsilon_0} B_1 \quad (2.29)$$

and

$$A_1^c \cdot \cos(k_y \cdot d) + A_1^s \cdot \sin(k_y \cdot d) = B_1 \quad (2.30)$$

where  $A_1^c$ ,  $A_1^s$ ,  $B_1$  can be eliminated using (2.28), (2.29), and (2.30), which generates the following eigenvalue equation for  $k_y$ :

$$\begin{aligned} & (\eta_0 \varepsilon_1 + \eta_m \varepsilon_0 \varepsilon_1) \cdot k_y \cdot \cos(k_y \cdot d) \\ & + (\eta_0 \eta_m \varepsilon_1^2 - \varepsilon_0 k_y^2) \sin(k_y \cdot d) = 0 \end{aligned} \quad (2.31)$$

The solution of the above equation provides the propagation constant along the  $y$  direction. The lowest value of  $k_y$  corresponds to the fundamental mode  $E_{p1}^y$ , the second value corresponds to the  $E_{p2}^y$  mode, and so on. After determining the values of  $k_y$ , the effective permittivity of the structure can be calculated by:

$$\varepsilon_{e1} = \varepsilon_1 - \frac{k_y^2}{k_0^2} \quad (2.32)$$

where  $\varepsilon_{e1}$  is the extracted effective permittivity. Since the structure is considered to incorporate dielectric and conductor losses, the extracted propagation constant  $k_y$  is a complex number that provides phase and attenuation constants along the  $y$  direction. Consequently, the extracted complex dielectric constant (i.e.,  $\varepsilon_{e1}$ ) includes the effective permittivity and effective dissipation factor. Here it is worth mentioning that since we consider the substrate to have two different sections (i.e.,  $\varepsilon_1$  and  $\varepsilon_2$ ), we have to repeat the above procedure and calculate the effective permittivity of the second dielectric layer (i.e.,  $\varepsilon_{e2}$ ). It is noteworthy that these extractions were conducted independently in the two regions, thus avoiding the application of boundary conditions at the interfaces between regions.

### 2.3.2 Extracting $k_z$

The effect of the top free-space layer studied through the method mentioned above and the calculated  $\varepsilon_e$  presents this effect. At this stage, the dielectric layer and the free-space layer are replaced with a single uniform dielectric layer having a relative permittivity equal to the calculated effective permittivity (see Fig. 2.3c).

*Region III*, which corresponds to the guiding channel, has the highest effective permittivity (i.e.,  $\varepsilon_{e2} > \varepsilon_{e1} > \varepsilon_0$ ). Therefore, electric scalar potential  $\phi^e$  should have sinusoidal distribution in this region. *Regions I* and *V* are considered free-space, and  $\phi^e$  should have an exponentially decaying distribution through these regions.  $\phi^e$  can have sinusoidal or decaying distribution through *Regions II* and *IV*, which correspond to the perforations sections. Accordingly,  $\phi^e$  can be formulated as:

$$\phi^e(x) = A_2 \cdot e^{\eta_0(x-x_1)}, \quad x \leq x_1 \text{ (region I)} \quad (2.33a)$$

$$\phi^e(x) = B_2^c \cdot \cosh[\xi(x-x_1)] + B_2^s \cdot \sinh[\xi(x-x_1)], \quad x_1 \leq x \leq x_2 \text{ (region II)} \quad (2.33b)$$

$$\phi^e(x) = C_2^c \cdot \cos[k_x(x-x_2)] + C_2^s \cdot \sin[k_x(x-x_2)], \quad x_2 \leq x \leq x_3 \text{ (region III)} \quad (2.33c)$$

$$\phi^e(x) = D_2^c \cdot \cosh[\xi(x-x_3)] + D_2^s \cdot \sinh[\xi(x-x_3)], \quad x_3 \leq x \leq x_4 \text{ (region IV)} \quad (2.33d)$$

$$\phi^e(x) = E_2 \cdot e^{-\eta_0(x-x_4)}, \quad x \geq x_4 \text{ (region V)} \quad (2.33e)$$

where  $A_2$ ,  $B_2^c$ ,  $B_2^s$ ,  $C_2^c$ ,  $C_2^s$ ,  $D_2^c$ ,  $D_2^s$ , and  $E_2$  are unknown constants.  $\eta_0$ ,  $\xi$ , and  $k_x$  are the attenuation in the free-space, propagation constant in the perforation region, and the propagation constant in the guiding channel along the  $x$  direction. The following equation demonstrates the relation between propagation constants in different regions.

$$k_z^2 = \varepsilon_0 k_0^2 + \eta_0^2 = \varepsilon_{e1} k_0^2 + \xi^2 = \varepsilon_{e2} k_0^2 - k_x^2 \quad (2.34)$$

where  $k_z$  is the propagating constant along the  $z$  direction in *Region III*, which corresponds to the guiding channel in the original SIIG structure. As shown in Fig. 2.3c, there are four interfaces in this sub-structure (i.e.,  $x_1$ ,  $x_2$ ,  $x_3$ , and  $x_4$ ); therefore, according to the boundary condition, tangential electric and magnetic fields components (i.e.,  $E_y$  and  $H_z$ ) should be matched at these interfaces. The following eigenvalue equation for  $k_x$  will be achieved after applying the boundary conditions and executing some mathematical manipulations.

$$\cosh(\xi w_p) \left( T_3 + \frac{\eta_0}{k_x} T_4 \right) + \sinh(\xi w_p) \left( \frac{\eta_0}{\xi} T_3 + \frac{\xi}{k_x} T_4 \right) = 0 \quad (2.35)$$

where

$$T_1 = \cosh(\xi w_p) + \frac{\xi}{\eta_0} \sinh(\xi w_p) \quad (2.36a)$$

$$T_2 = \sinh(\xi w_p) + \frac{\xi}{\eta_0} \cosh(\xi w_p) \quad (2.36b)$$

$$T_3 = T_1 \cdot \cos(k_x w_g) - T_2 \cdot \frac{k_x}{\xi} \sin(k_x w_g) \quad (2.36c)$$

$$T_4 = T_1 \cdot \sin(k_x w_g) + T_2 \cdot \frac{k_x}{\xi} \cos(k_x w_g) \quad (2.36d)$$

and from (2.34), we have:

$$\eta_0 = \sqrt{(\varepsilon_{e2} - \varepsilon_0)k_0^2 - k_x^2} \quad (2.37a)$$

$$\xi = \sqrt{(\varepsilon_{e2} - \varepsilon_{e1})k_0^2 - k_x^2} \quad (2.37b)$$

The solution of (2.35) provides the propagation constant along the  $x$  direction in the guiding channel. The lowest value of  $k_x$  corresponds to the fundamental mode  $E_{1q}^y$ , the second value corresponds to the  $E_{2q}^y$  mode, and so on. Then, the propagation constant  $k_z$  can be calculated using (2.34). The same procedure can be followed to extract the propagation constant  $k_z$  for the horizontally polarized modes  $E_{pq}^x$ .

## 2.4 Validation using eigen-mode solver and Experimental Prototype

The proposed method is applied to analyze an SIIG structure in this section. The accuracy and efficiency of the proposed method are demonstrated through comparison with the eigen-mode solution of *Ansys HFSS*, *CST Studio Suite* software, and a fabricated SIIG structure as an experimental prototype.

As the first example, an alumina substrate with a thickness of  $d = 254 \mu m$ , which has relative permittivity equal to  $\varepsilon' = 9.4$  and loss tangent of  $\tan \delta = 6 \times 10^{-3}$ , is considered to have periodic rectangular perforations as shown in Fig. 2.1a. The perforations have periodicity equal to  $a = c = 290 \mu m$  and dimensions of  $b = d = 200 \mu m$ . The effective permittivity, loss tangent, and the field distribution inside the mentioned structure are calculated using the proposed method, the eigen-mode solver of the *CST Studio Suite*, and the *Ansys HFSS* software, and the results are compared in Figs. 2.4, 2.5, and 2.6, respectively.

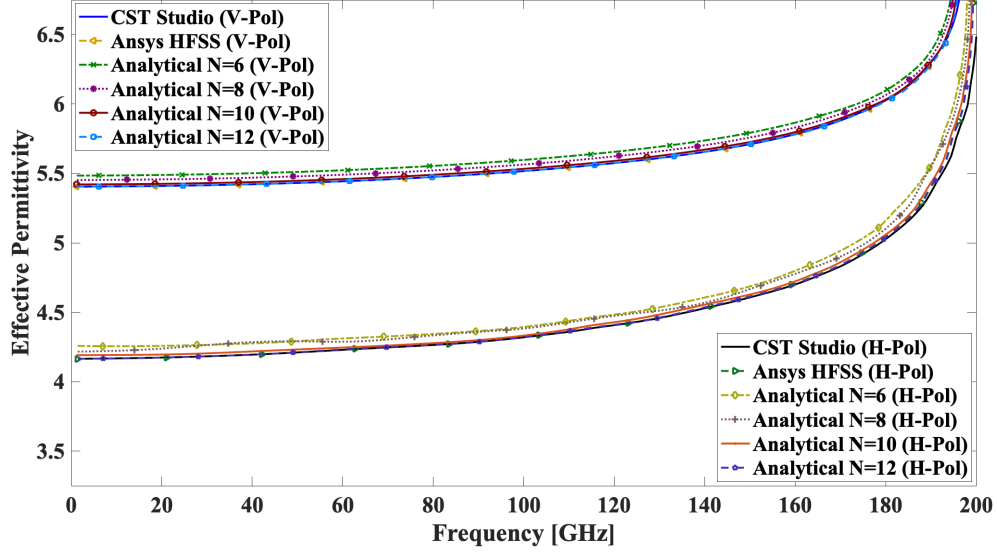


Figure 2.4 Extracted effective permittivity of alumina substrate with rectangular perforations.

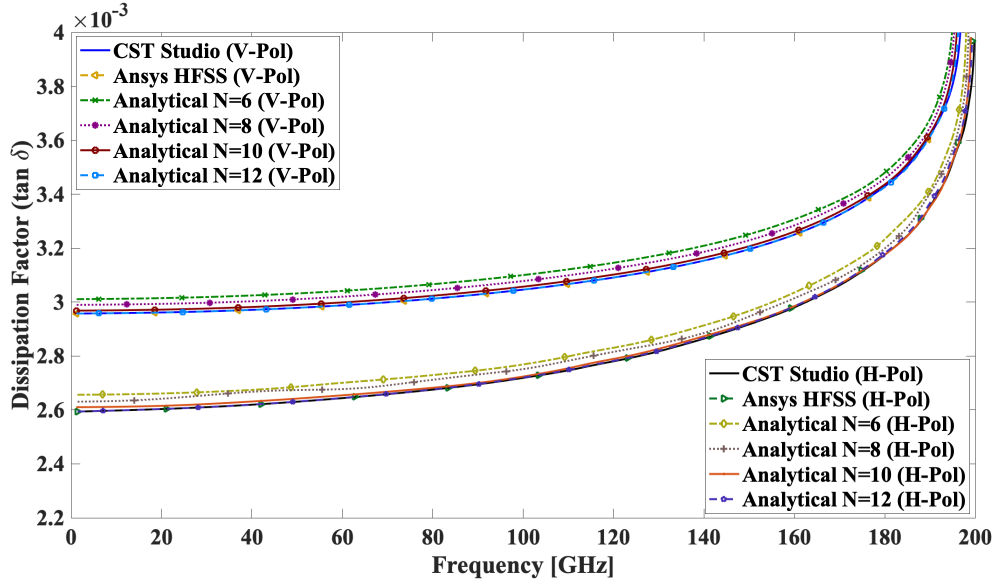


Figure 2.5 Extracted dissipation factor of alumina substrate with rectangular perforations.

The figures demonstrate an excellent agreement between the proposed method and commercial software simulations up to 200 GHz. Additionally, the simulation results reveal that the structure has different responses (in terms of permittivity and loss tangent) for vertically and horizontally polarized modes meaning that the structure has anisotropic behavior [57]. Here, it is important to highlight that the variable  $N$  represents the number of terms summed in the *Fourier Series* expansion, thereby influencing the accuracy of the results. To check the

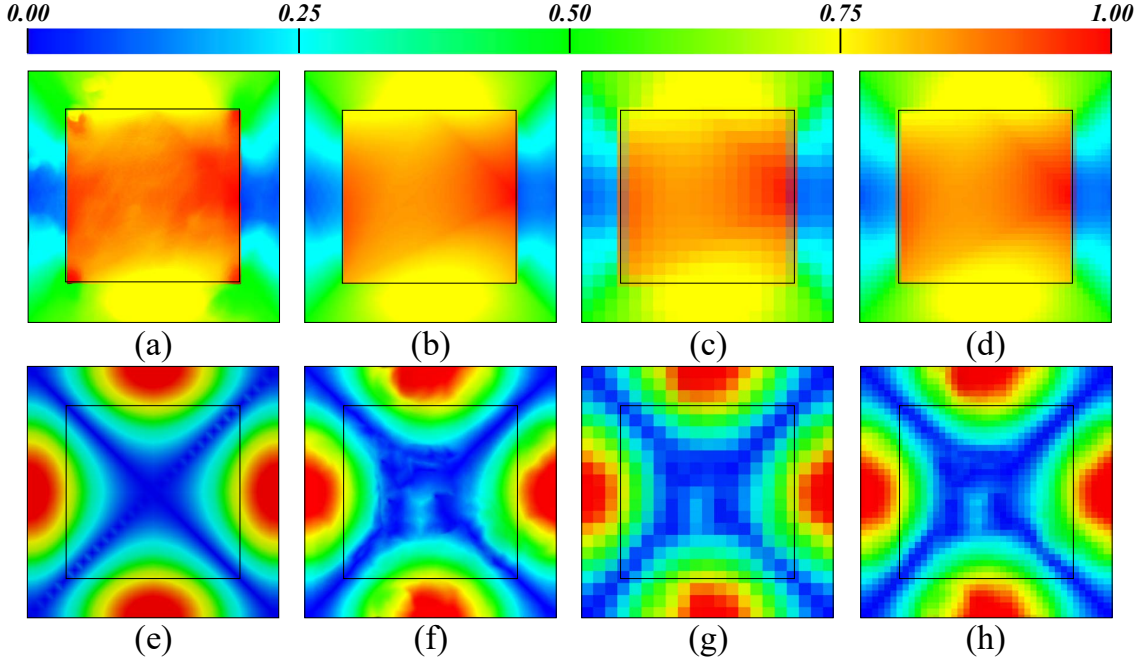


Figure 2.6 Normalized electric (i.e.,  $E_z$  for the vertical mode) and magnetic (i.e.,  $H_z$  for the horizontal mode) field magnitude distribution inside an alumina substrate with rectangular perforations: a) CST Studio Suite software (V-Pol), b) Ansys HFSS software (V-Pol), c) analytical method with  $N = 10$  (V-Pol), d) analytical method with  $N = 20$  (V-Pol), e) CST Studio Suite software (H-Pol), f) Ansys HFSS software (H-Pol), g) analytical method with  $N = 10$  (H-Pol), h) analytical method with  $N = 20$  (H-Pol).

convergence of the proposed method, the number of summed terms considered varies from  $N = 6$  to 12. As shown in Table I, increasing the summed terms produces more accurate results; however, a slight improvement is observed for ten (i.e.,  $N = 10$ ) terms and more. Accordingly, the number of summed terms is set to ten in the further calculations.

A careful review of (2.12) and (2.21) reveals that the number of summed terms in the *Fourier Series* expansion and the *Floquet Theory* defines the number of field harmonics inside the structure, which corresponds to the propagating modes. Considering the number of the summed terms equal to  $N$  leads to extracting  $(2N + 1)^2$  propagating modes. Additionally, this number determines the size of eigenvector matrices which defines the resolution of the field distribution inside the unit-cell. Although an increasing number of the summed terms improves the field distribution resolution, larger eigenvector matrices consume more computational resources and times to be extracted. In order to provide a good insight into the efficiency of the proposed method, the eigen-mode solver of the *CST Studio Suite*, *Ansys HFSS* software, and the proposed method were run on an Intel(R) Core(TM) i7-4790 CPU with 32 GB installed memory (RAM) to extract the effective permittivity of the aforemen-

tioned perforated structure. A comparison between the recorded simulation run-time (which is provided in Table I) reveals that the proposed method is much faster than the eigen-mode solver of these commercial EM software and will significantly reduce the computational time, especially in optimization problems that require simulating a structure repeatedly.

Table I shows that the *CST Studio Suite* achieved a faster run-time than the *Ansys HFSS*, while both provided accurate results (the relative error is 0.37%). Accordingly, we consider the *CST Studio Suite*'s results as the reference. Considering three summed terms (i.e.,  $N = 1$ ) leads to a simulation time of 0.56 seconds and generates a 6.81% relative error. As mentioned, more summed terms generate more accurate results, which would increase the simulation time. Considering 21 summed terms (i.e.,  $N = 10$ ) leads to a simulation time of 42.33 seconds and generates a 1.29% relative error, which is an excellent accuracy. Comparing with the reference results reveals that the proposed method with  $N = 10$  can reduce the run-time by 65 times. In addition to providing more accurate results, increasing the summed terms will increase the simulation time. Hence, we consider 21 summed terms (i.e.,  $N = 10$ ) for further calculations.

To demonstrate the applicability of the proposed method, the same substrate is considered to have circular perforations with a periodicity equal to  $a = 290 \mu m$  and a diameter of  $b = 200 \mu m$ . A comparison between the proposed method and the eigen-mode solver of the *CST Studio Suite* and the *Ansys HFSS* software in terms of the effective permittivity, loss tangent, and the field distribution for V-Pol and H-Pol are shown in Figs. 2.7, 2.8, and 2.9, respectively. Here it is worth mentioning that, for open dielectric waveguide applications, the highest contrast between the permittivity of the guiding channel and the perforated regions needed to be realized to achieve the highest possible power transmission. Specifically, for the SIIG structure, the perforated region should have a low permittivity [4]. As it can be observed from the provided figures, there is an excellent agreement between the results achieved in the low-permittivity region. Considering  $N = 10$  generates a maximum 2.58% relative error for V-Pol and H-Pol modes extraction.

As the second example, the same alumina substrate (i.e.,  $\varepsilon' = 9.4$ ,  $\tan \delta = 6 \times 10^{-3}$ , and  $d = 254 \mu m$ ) is assumed to have periodic rectangular perforations as shown in Fig. 2.1a. The perforation periodicity is considered to be constant and equal to  $a = c = 290 \mu m$ . However, the size of the perforations is considered to vary from  $b = 2 \mu m$  to  $b = 290 \mu m$ . Dispersion diagram of different sizes are extracted and shown in Fig. 2.10. According to this figure, when the substrate has very small perforations, the resulted effective permittivity will be close to the alumina's relative permittivity. Accordingly, the dispersion diagram should approach the  $1/(2\pi \sqrt{\varepsilon_r})$  line. When the substrate has a very large perforations, the resulted

Table 2.1 Recorded Run-Rime and Calculated Relative Error of Different Methods Used to Extract the Propagating Modes.

	CST Studio	Ansys HFSS	Proposed Method			
			$N = 1$	$N = 5$	$N = 10$	$N = 20$
Number of Extracted Modes	9	9	9	121	441	1681
Run-Times(sec)*	2775.70	2911.62	0.56	3.09	42.33	962.66
Relative Error(%)*	ref.	0.37	6.81	4.16	1.29	0.94

\* To consider the worst-case scenario, maximum values of the recorded run-time and calculated relative error of the V-Pol and H-Pol modes are provided in the table.

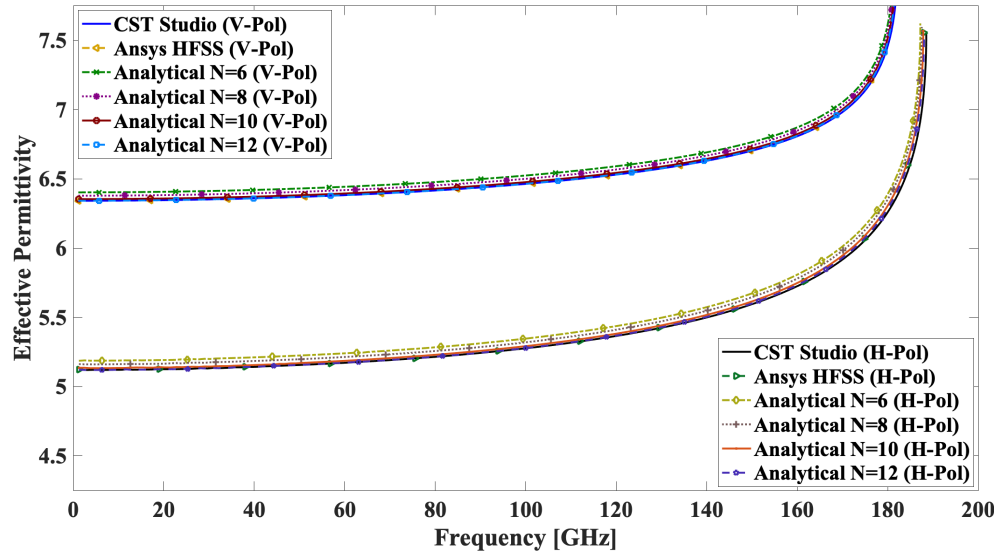


Figure 2.7 Extracted effective permittivity of alumina substrate with circular perforations.

effective permittivity will be close to the free-space's relative permittivity. Accordingly, the dispersion diagram should approach the  $1/(2\pi)$  line. As demonstrated in Fig. 2.10, the proposed method has excellent agreement with the expected results. For the next example, the same analysis is followed for periodic circular perforations and the extracted dispersion diagram is shown in Fig. 2.11. As can be observed from this figure, the proposed method is consistent with the expected results. Here it is worth mentioning that, since the circular perforation removes less substrate than the rectangular perforation with the same sizes, the dispersion curves in the Fig. 2.11 could not reach their maximum value (i.e., the  $1/(2\pi)$  line).

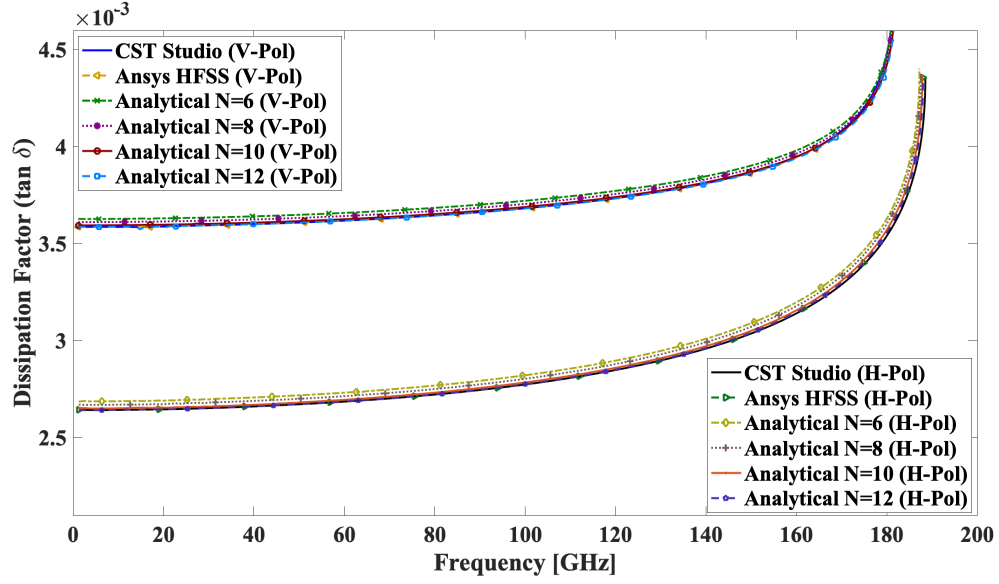


Figure 2.8 Extracted dissipation factor of alumina substrate with circular perforations.

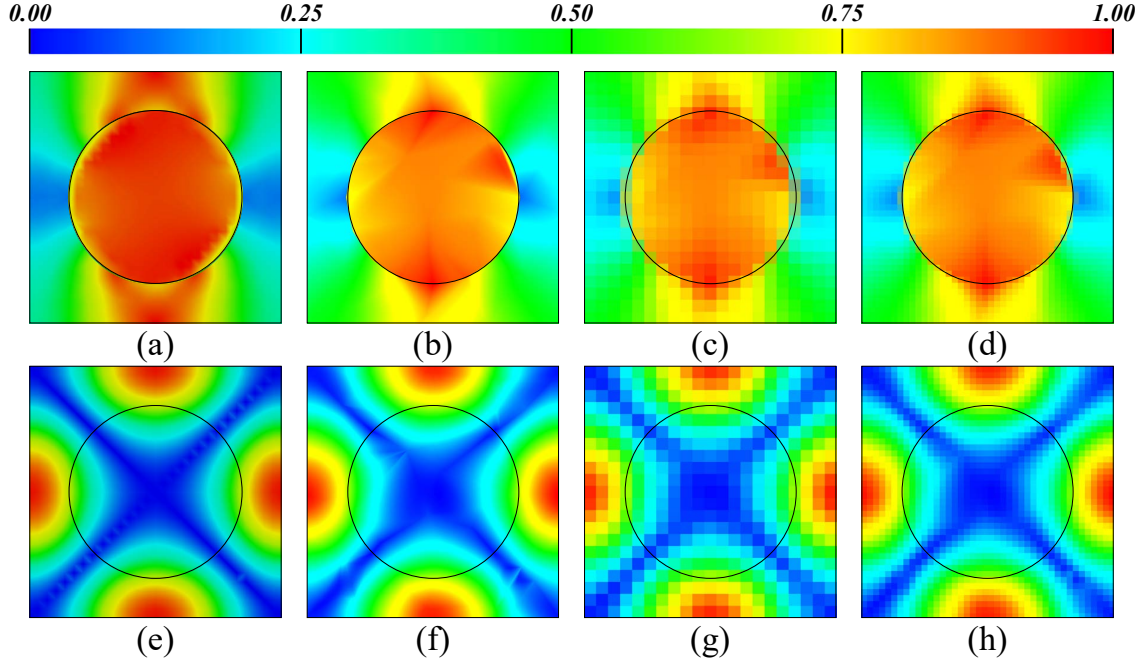


Figure 2.9 Normalized electric (i.e.,  $E_z$  for the vertical mode) and magnetic (i.e.,  $H_z$  for the horizontal mode) field magnitude distribution inside an alumina substrate with circular perforations: a) CST Studio Suite software (V-Pol), b) Ansys HFSS software (V-Pol), c) analytical method with  $N = 10$  (V-Pol), d) analytical method with  $N = 20$  (V-Pol), e) CST Studio Suite software (H-Pol), f) Ansys HFSS software (H-Pol), g) analytical method with  $N = 10$  (H-Pol), h) analytical method with  $N = 20$  (H-Pol).



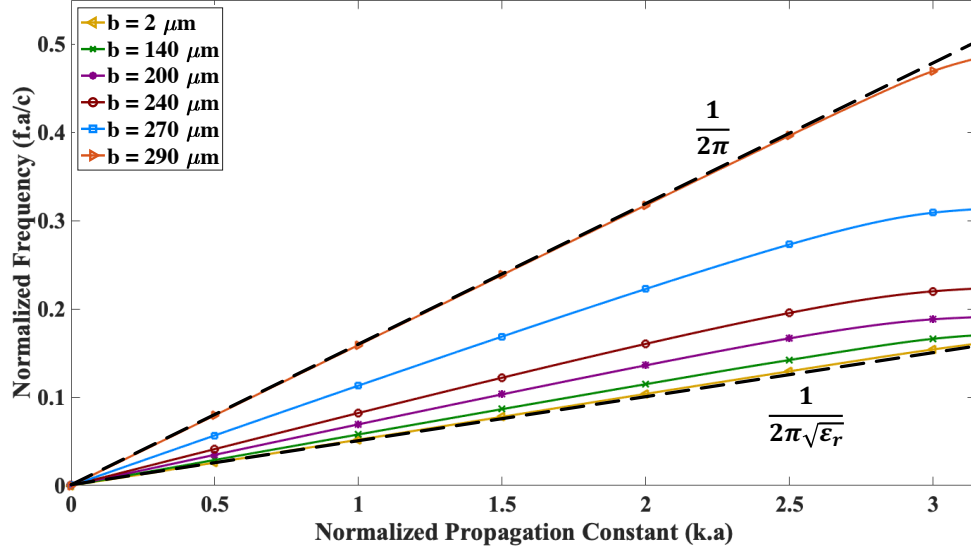


Figure 2.10 Dispersion diagram of an alumina substrate having periodic rectangular perforations with different sizes.

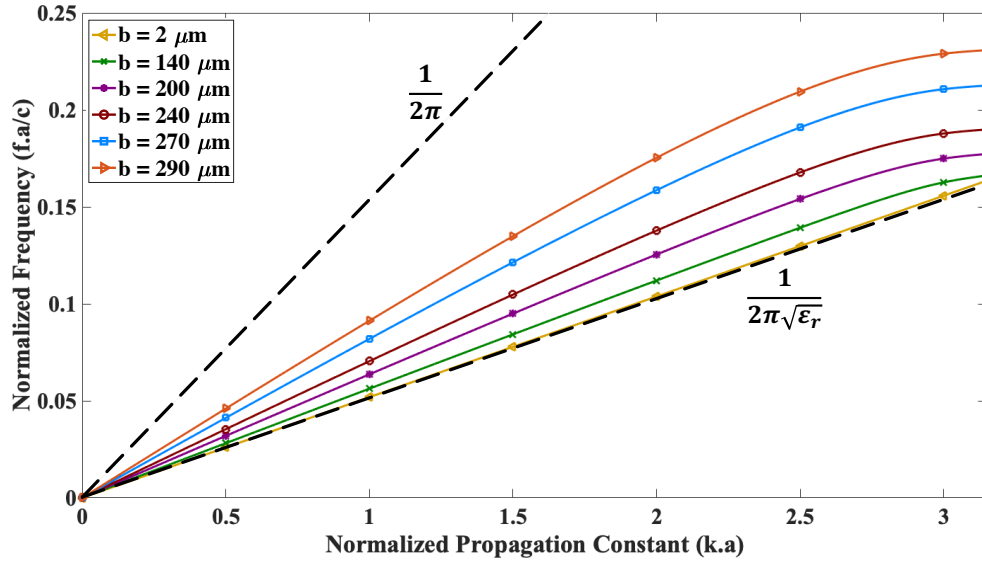


Figure 2.11 Dispersion diagram of an alumina substrate having periodic circular perforations with different sizes.

Based on the fabrication limitations and material availability at the *Poly-Grames Research Center*, an alumina ( $\epsilon_r = 9.4$ ) substrate is utilized to create an SIIG structure. The SIIG structure is considered to have a guiding channel of  $w_c = 500 \mu m$ , a thickness of  $d = 254 \mu m$ , and five rows of circular perforations with a periodicity of  $a = 290 \mu m$  and a diameter of  $b = 200 \mu m$ . The proposed modal analysis, *CST Studio Suite*, and the *Ansys HFSS* software are

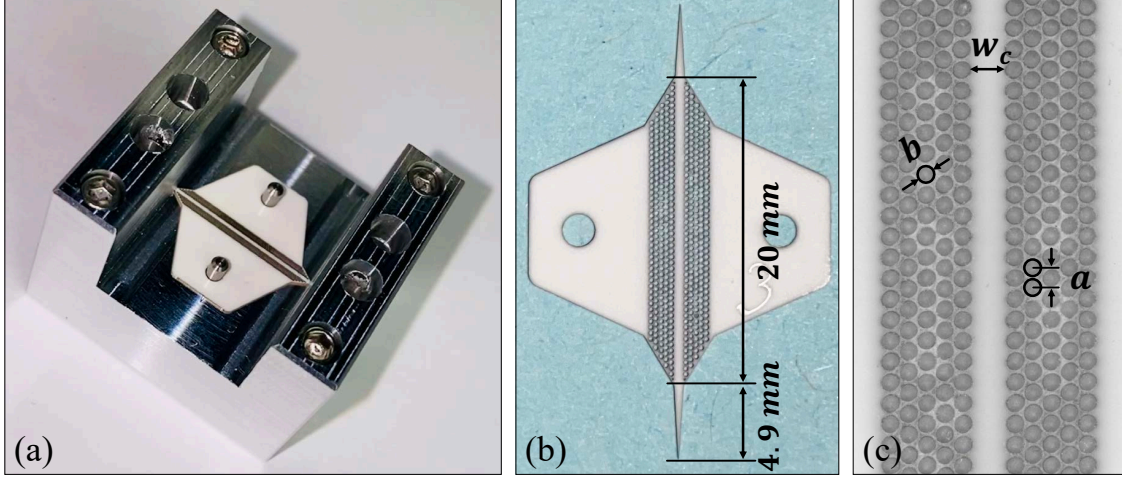


Figure 2.12 a) The fabricated SIIG structure fed by WR-5.1 waveguide, b) the fabricated alumina substrate having 5 rows of circular perforations, c) zoomed view of the guiding channel and adjacent perforated regions.

used to extract the phase constant ( $\beta$ ) and the attenuation constant ( $\alpha$ ) of the aforementioned SIIG structure, and the results are shown in Figs. 2.13 and 2.14, respectively. The results demonstrate that the proposed modal analysis perfectly agrees with the commercial EM simulation software. As illustrated in the mentioned figures, the first ten modes of the SIIG structure are extracted and plotted.

Regarding the implementation of the proposed modal analysis, it is worth mentioning that (2.31) and (2.35) are nonlinear complex eigensystem problems that require substantial computational resources to be solved. Typically, numerical solutions to such eigensystem problems extensively consume the CPU and time. To overcome this problem, *Maple* software is utilized to solve the eigensystems analytically, which is much faster than the numerical solutions. Recorded run times reveal that the proposed method is much faster than the *CST Studio Suite* and the *Ansys HFSS* software ( $\sim 300$  times faster) while providing a remarkably high accuracy. To be specific, considering 21 summed terms (i.e.,  $N = 10$ ) for the effective-permittivity and the effective-loss extraction along with the estimation used in the modified modal analysis enable the proposed method to generate a maximum relative error of 4.29% in extracting the propagating modes in an SIIG structure. It is worth mentioning that this comparison is based on the simulation time spent to extract the first twenty propagating modes and may change for a different number of modes.

The above-mentioned SIIG structure (i.e.,  $w_c = 500 \mu m$ ,  $d = 254 \mu m$ ,  $a = 290 \mu m$ , and  $b = 200 \mu m$ ) was fabricated to compare the proposed method with a real SIIG waveguide. As shown in Fig. 2.12, the structure is fed with a WR-5.1 rectangular waveguide. Although

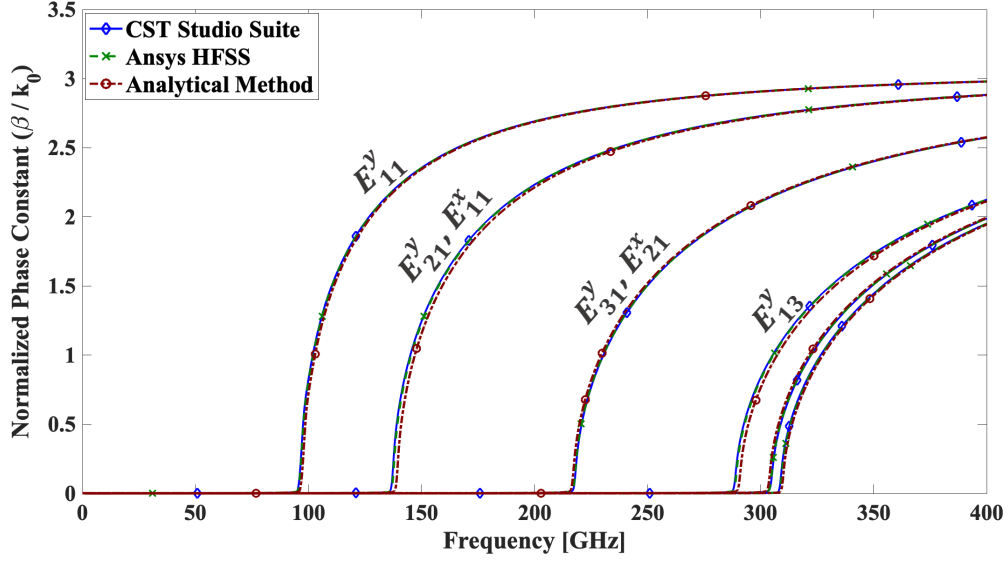


Figure 2.13 Extracted normalized phase constant of the mentioned SIIG structure.

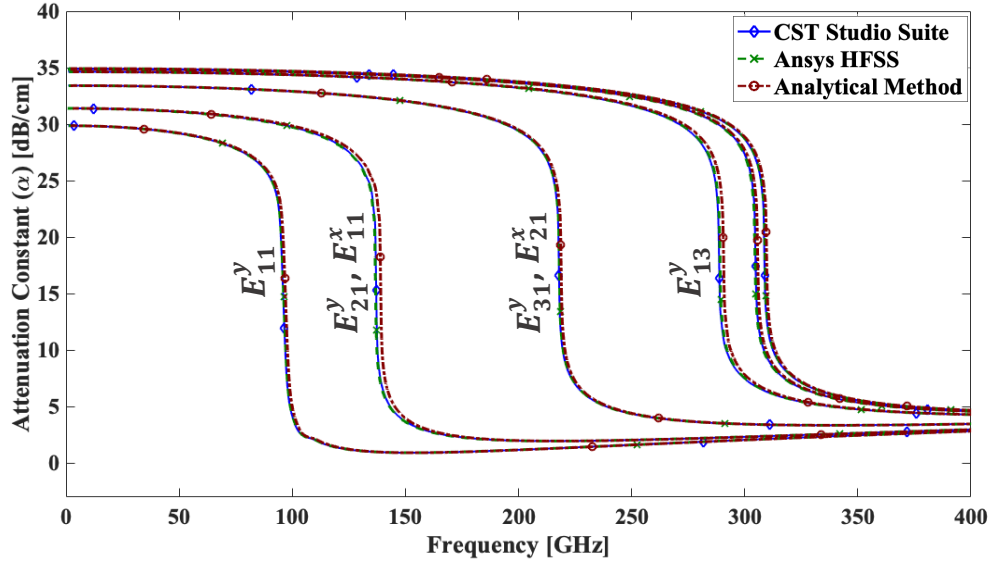


Figure 2.14 Extracted attenuation constant of the mentioned SIIG structure.

the actual SIIG waveguide is a planar structure, it is considered to be fed with a rectangular waveguide. Accordingly, most of the losses in the fabricated structure are due to the feeding mismatch. To remove this loss and accurately measure the transmission loss, the dual-line technique is used [58]. Two SIIG structures differing in length (20mm and 30mm) are fabricated, and the propagation constant is extracted subsequently from the pair of measured

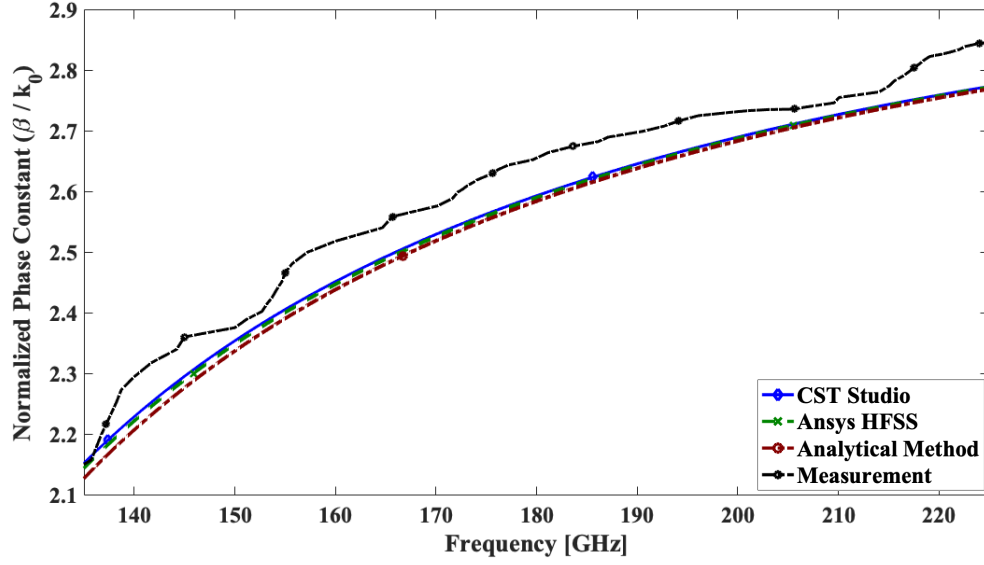


Figure 2.15 Extracted normalized phase constant of the fabricated SIIG structure.

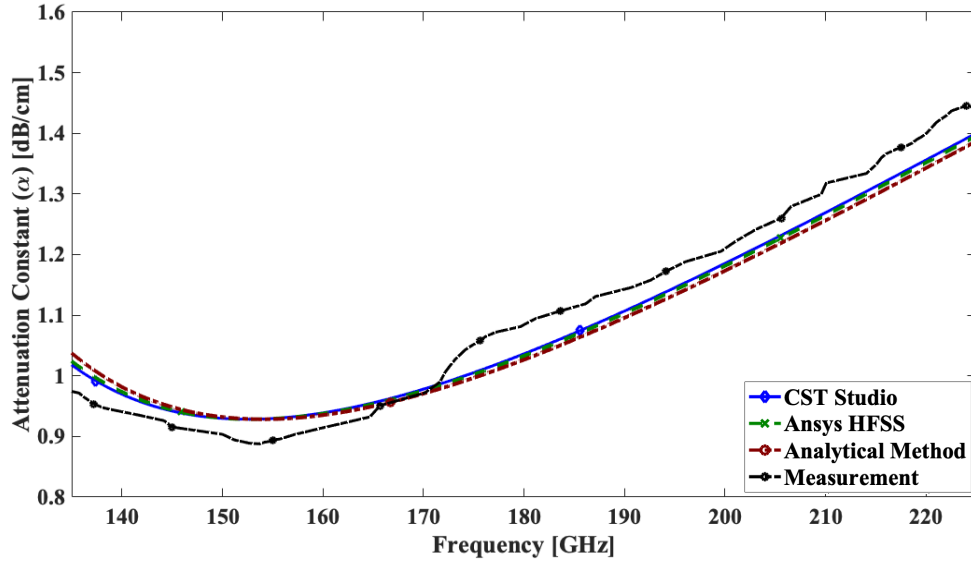


Figure 2.16 Extracted attenuation constant of the fabricated SIIG structure.

S-parameters, as:

$$\beta = \frac{|\angle \mathbf{S}_{21,\text{long}} - \angle \mathbf{S}_{21,\text{short}}|}{\Delta l} \quad (2.38a)$$

$$\alpha = \frac{-\ln(|\mathbf{S}_{21,\text{long}}| / |\mathbf{S}_{21,\text{short}}|)}{\Delta l} \quad (2.38b)$$

where  $\Delta l$  is the length difference,  $\angle \mathbf{S}_{21,\text{long}}$  and  $\angle \mathbf{S}_{21,\text{short}}$  denote the absolute phase (in radian)

of the measured complex S-parameters of the long and the short fabricated SIIG sections, respectively. Comparisons between the proposed method, *CST Studio Suite*, *Ansys HFSS*, and the fabricated SIIG structure are shown in Figs. 2.15 and 2.16, which demonstrate an excellent agreement. Since the measurement equipment (i.e., WR-5.1 waveguide and measurement extender) has a recommended operating frequency band of 135 GHz to 225 GHz, the frequency range plotted in these figures is thus limited. However, the proposed methods' applicability is not limited to this frequency range.

## 2.5 Conclusion

We developed a novel method to accurately analyze dielectric waveguides in the THz regime. The imaginary part of the substrate permittivity is the source of dielectric losses, which will be critical for high-frequency applications. Unlike the existing analytical methods, which consider the substrate as a lossless pure dielectric, the presented method took these losses into consideration. Accordingly, by considering the perforations as a periodic structure and applying the *Floquet Theory* and the *Fourier Series* expansion, we developed an eigen-equation for the electric field inside the dielectric substrate in which the effective permittivity of the structure is accurately modeled through the eigenvalue calculation.

Extracting the effective permittivity and the dielectric losses of the bilateral perforated regions in dielectric waveguides leads to modifying a modal analysis to extract the propagating properties of these structures. Conductor losses become critical in the THz regime; thus, by considering losses for all conductors and applying the *Impedance Boundary Condition (IBC)*, we achieved a modified modal analysis that can accurately extract the propagation constant of the propagating modes along dielectric waveguides. This modified modal analysis can be effectively applied to all layered dielectric waveguides, including strip dielectric guide, insulated image guide, and strip-slab guide.

Through the provided examples, the proposed method's accuracy and applicability were compared with commercial EM software (i.e., *CST Studio Suite* and *Ansys HFSS*). It was shown that the proposed method provides accurate results (95% accuracy) while having a considerable CPU run-time gain (300 times) over the commercial EM software. Comparison with a fabricated SIIG waveguide as an experimental prototype demonstrated that the proposed method has a high accuracy in realistic scenarios.

# CHAPTER 3 ARTICLE 2: EXPLORING LOW-LOSS WIDEBAND SUBSTRATE-INTEGRATED IMAGE GUIDES (SIIG) FOR TERAHERTZ APPLICATIONS

Mohammad Moradi, Mohammad S. Sharawi, Ke Wu

Published in: IEEE Transactions on Terahertz Science and Technology

Publication date: November 13, 2023

## 3.1 Introduction

In light of an exponential growth in the number of end users of wireless communication systems, communication channels are becoming increasingly congested. Furthermore, the development of high-resolution imaging applications [27, 28], and molecular-sensitive spectroscopic devices [29], as well as the increasing demand for ultra-broadband wireless data transmission in multi-user environments has drawn significant attention to high-frequency integrated circuits and systems. Within a short period of time, a wide range of wireless sensors and communication devices will be widely spread and used immediately with the advent of the upcoming 6G technology. Consequently, the system framework must be extremely well integrated due to the limited space available for installing a large number of sensors and communication components. These underlying issues can be properly addressed by utilizing THz technologies [9].

Although THz communication shares many of the same fundamental principles as its microwave counterpart, it faces a number of challenges. One of them is the transmission loss in frontends, which is often substantial in the THz regime. It is important to point out that the conductive losses will increase significantly as frequency increases, and the skin effect further aggravates these losses; as a result, attenuation can reach several tens of dB/cm [30–32]. Due to this limitation, conventional metal-based technologies (e.g., microstrip, co-planar, and substrate integrated waveguide (SIW)) are not suitable for up-end THz band circuit, antenna, and system applications. Although conventional rectangular waveguides (RW) provide low-loss wave transmission, they suffer from a lack of compactness which is critical for integrated circuits applications. Moreover, since electrical contacts between waveguide blocks are strictly required, RWs require a precise and costly manufacturing process [59, 60].

The Gap Waveguide (GW), proposed in [61], could attract a great deal of attention due to its low transmission losses and low fabrication complexity. By parallelly placing a perfect

electric conductor (PEC) layer along with a perfect magnetic conductor (PMC) layer [62,63] having a separating air gap ( $< \lambda/4$ ), the gap waveguide technology restricts the wave from being propagated in an unintended direction. To provide wave propagation along the gap waveguide, specific guiding structures (i.e., strips, ridges, and grooves) are embedded within the above-mentioned parallel-layers configuration [64]. Since no perfect electrical/mechanical contact between metal blocks is required, the gap waveguide's fabrication process is more straightforward than the rectangular waveguide, especially at higher frequencies. This type of waveguide possesses a lower loss than microstrip lines since no dielectric material is used in its structure [65]. However, similar to rectangular waveguides, gap waveguides suffer from a lack of compactness. A small air gap of  $\lambda/4$  that needs to be maintained all over the parallel plates, will become extremely small and hard to realize at THz frequencies. Furthermore, the PMC section of the gap waveguides is typically implemented using small periodic conductive pins, which necessitates the use of highly conductive materials in their structures. However, the fabrication of these pins involves intricate, costly, and time-consuming processes (i.e., micro-machining CNC or deep reactive ion etching (DRIE) combined with metal coating).

Dielectric waveguides, which have widely been used in photonic circuits, exhibit excellent potentials in developing THz circuits and antennas due to the absence of metallic loss. These photonic-inspired guiding structures, including hollow-core [66,67], solid-core [68,69], and porous-core [70–72] waveguides demonstrate to have attenuation as low as 1.0 to 0.1 dB/cm in the THz region. Typically, the wave guidance occurs in the metallic waveguides based on the field's interactions with conductor flowing currents. In the dielectric waveguides, however, the wave guidance happens due to the total internal reflections at the dielectric-dielectric (or air) interface. The geometry of hollow and porous-core waveguides is inherently large, limiting their usage in highly integrated THz systems. However, the planar forms of solid-core waveguides, including silicon-on-insulator (SOI) waveguides [73,74], dielectric microstrip lines (DMLs) [45,75], and dielectric photonic crystal waveguides [33,76,77] are good candidates for usage in THz systems. However, these waveguides are extremely fragile, and their low field confinement yields considerable leakage around the guiding channel.

To provide more rigidness, a metallic ground plane can be added to these planar dielectric waveguides. In addition to providing mechanical support, the metallic ground plane acts as one-side shielding, which also can be used to dissipate heat from active devices. Furthermore, the ground plane increases the useable single-mode bandwidth by shifting higher-order modes to higher frequencies. In [18], by placing a high-permittivity rectangular dielectric line on a metallic ground plane, Knox et al. proposed a hybrid guiding structure named "Image Guide," which is probably the simplest and the most used dielectric waveguide. A wide variety of passive and active circuit components were realized in image guide technology, which proves

the benefits of integrated dielectric technology [78–80]. While image guide structures provide very low transmission losses, they have some problems regarding fabrication and integration. Especially at high frequencies, the single dielectric strip has extremely small dimensions, which requires a precise fabrication process. Additionally, this small dielectric strip should be precisely aligned with other circuit components in integrated circuit applications.

Inspired by the "substrate-integrated circuit" concept [26], Patrovsky et al. proposed a sanitized form of the image guide named "Substrate-Integrated Image Guide (SIIG)" [4]. Similar to the standard image guide, the SIIG consists of a planar high-permittivity substrate placed on a continuous metallic ground plane. To realize the permittivity contrast between the guiding channel and the bilateral regions, periodic air perforations are added to these regions, which artificially reduces the effective permittivity of these sections. Therefore, the SIIG provides a similar guiding effect as the standard image guide, except for particularities caused by the periodic perforations. The planar substrate makes the fabrication process more accessible and provides a high alignment precision to the other integrated circuit components. Additionally, the interconnection with other waveguide technologies is substantially simplified on the same substrate. It is important to note that the analysis presented in [4] was based on data extracted from Ansys HFSS, an electromagnetic (EM) simulation software.

Recently, a hybrid planar dielectric waveguide named Substrate-Integrated Hybrid Metallo-Dielectric (SIHMD) [81] waveguide has been proposed by Liu et al. This structure is made by connecting the Substrate-Integrated Dielectric Waveguide (SIDW) and the Substrate-Integrated Non-Radiative Dielectric (SINRD) waveguide [46]. The integration of such waveguides on a planar substrate offers advantages in terms of high alignment precision with other integrated circuit components, reduced overall loss of guided-wave structures, and simplified interconnection with other waveguides on the same substrate. However, SIHMD may present a more complex structure compared to the Substrate-Integrated Image Guide (SIIG) on a comparable loss scale. The fabrication process for the SIHMD waveguide involves metal coating, which adds complexity and increases both cost and time required for fabrication. Moreover, the SIHMD waveguide suffers from potential mode conversion and disturbing interference at the SIDW and SINRD interfaces. It is important to highlight that the SINRD section exhibits significantly higher transmission losses in comparison to the SIDW section [81]. Upon conducting a detailed analysis of both sections, it becomes evident that the discrepancy in insertion losses primarily arises from the conductor losses, which escalate with the length of the SINRD section. Consequently, the length of the SINRD section has intentionally been kept short to ensure that the total insertion loss remains within an acceptable range.

In this paper, we investigate and demonstrate the SIIG technology as a promising candidate



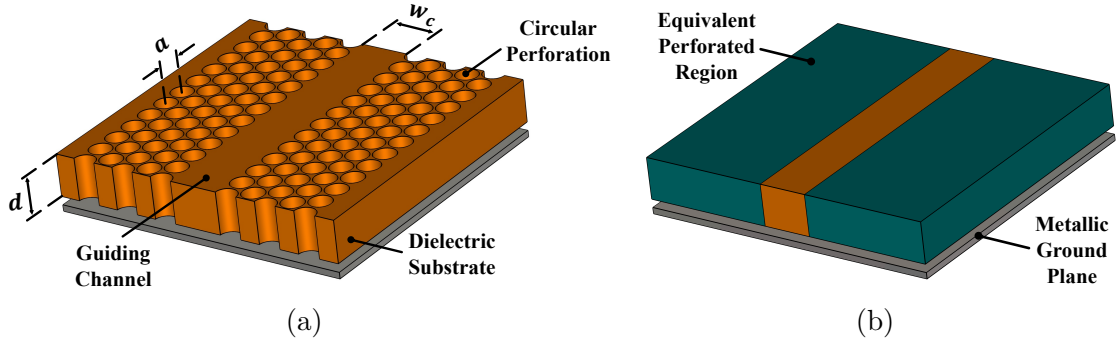


Figure 3.1 Exposed view of (a) actual Substrate Integrated Image Guide (SIIG) structure and (b) its equivalent model.

for THz applications. Due to its guiding mechanism, the SIIG possesses very low transmission losses. Further, since the metallic ground plane is not involved in the wave guidance process, this technology produces very low conductor losses, which is critical in the THz regime. The investigated SIIG structure offers the advantage of incorporating an optional low-permittivity insulation film between the ground plane and the high-permittivity substrate. This additional film effectively minimizes conductor losses, as it mitigates the intensity of magnetic fields at the ground plane surface, leading to reduced induced current densities. Through the removal of the insulating layer, the investigated SIIG structure provides an easier fabrication and a potential for seamless integration with other circuit components for substrate-integrated circuit (SIC) applications. The elimination of the optional insulating layer simplifies integration with different technologies by allowing them to share the same substrate and ground plane. The effects of the structural parameters on the wave guidance behavior of the SIIG are analytically studied. Two prototype waveguides operating within the frequencies of 150 GHz and 300 GHz are fabricated by choosing the best available structural parameters. The responses of the fabricated waveguides are measured and compared with the analytical method and the commercial EM software. The provided comparisons demonstrate excellent agreement between the measurements and the simulations.

Accordingly, the rest of the paper is organized as follows: Section 3.2 presents two analytical methods required for conducting the modal analysis for SIIG waveguides. Section 3.3 introduces SIIG design parameters and proposes the design procedure in detail. Section 3.4 provides information on the fabricated SIIG prototypes and recorded measured results. Section 3.5 provides a comprehensive comparison between the fabricated SIIG prototypes and existing technologies at THz regime. A brief conclusion is presented in Section 3.6.

### 3.2 Substrate Integrated Image Guide (SIIG) Analysis

In Fig. 3.1a, the illustrated SIIG topology reveals the formation of a guiding channel within a high-permittivity dielectric substrate through the incorporation of periodic perforations. It is important to note that the size, shape, and arrangement of these perforations are carefully selected to precisely control the resulting effective permittivity. While the effective medium theory is a well-established and widely-used approach, it provides an average effective permittivity based on a filling factor of perforations in substrate [82,83]. Accordingly, different perforation shapes (or patterns) with the same filling factor are considered to have equal effective permittivity. Additionally, the effective permittivity obtained from effective medium theory is typically frequency independent. However, as studied in [84], different perforation shapes and patterns could lead to varying effective permittivity values. Furthermore, the resulting effective permittivity may exhibit a significant frequency dispersion. This dispersion indicates that the effective permittivity is not a constant value but varies with frequency. By considering these air holes as periodic perforations and applying the *Floquet theory* and the *Fourier Series* expansion, these bilateral sections' effective permittivity and dissipation factor can be extracted, which are essential for analyzing the SIIG waveguide. According to the analytical method presented in [84], the periodically perforated substrate has anisotropic behavior meaning that the structure has different responses (in terms of permittivity and loss tangent) for vertically (i.e.,  $E_{pq}^y$ ) and horizontally (i.e.,  $E_{pq}^x$ ) polarized modes.

It is important to emphasize that while the effectiveness of full-wave simulation software (e.g., *Ansys HFSS* and *CST Studio Suite*) in providing valuable insights into waveguide behavior, their usage becomes impractically time-consuming when dealing with intricate structures like SIHMD and SIIG waveguides. In contrast, the analytical model presents a highly advantageous solution, offering exceptional speed and efficiency, allowing parameter sweeps to be completed in a matter of minutes. As a result, the analytical model excels in swiftness, making it the ideal choice for conducting parameter studies and expediting the design process [84].

According to the analytical method, the cut-off frequency of each propagating mode inside this periodically perforated substrate can be achieved by solving the corresponding eigensystem problem. The eigenvalue equation for the vertically polarized mode (i.e.,  $E_{pq}^y$ ) inside a substrate with circular perforations is expressed as:

$$a_{(l,n)} \left[ \left( \frac{2\pi l}{a} + k_{x_0} \right)^2 + \left( \frac{2\pi n}{c} + k_{y_0} \right)^2 \right] = k_0^2 \sum_k \sum_m a_{(k,m)} b_{(l-k,n-m)} \quad (3.1)$$

where  $a_{(l,n)}$  is the field-related *Fourier Series* unknown coefficient.  $k$ ,  $l$ ,  $m$ , and  $n$  are the numbers of summed terms that define the approximation's accuracy. To be specific, more summed terms produce more accurate results. Accordingly, these variables should be an integer number ranging from  $-N$  to  $N$ .  $a$  is the periodicity along the  $x$  direction,  $c$  is the periodicity along the  $y$  direction,  $k_{x_0}$  is the propagation constant along the  $x$  direction, and  $k_{y_0}$  is the propagation constant along the  $y$  direction.  $b_{(l-k,n-m)}$  is the permittivity-related *Fourier Series* coefficient, which can be found by applying the *Fourier Series* coefficient on a unit-cell as:

$$b_{(i,j)} = \varepsilon_r \delta_{(i,j)} - (\varepsilon_r - 1) \frac{\pi b^2}{a^2} \frac{2J_1 \left( \sqrt{\left(\frac{2\pi i b}{a}\right)^2 + \left(\frac{2\pi j b}{a}\right)^2} \right)}{\sqrt{\left(\frac{2\pi i b}{a}\right)^2 + \left(\frac{2\pi j b}{a}\right)^2}} \quad (3.2)$$

where  $b$ ,  $\delta_{(i,j)}$ , and  $J_1$  are the perforation diameter, *Kronecker Delta*, and the *Bessel function of the first kind*, respectively. The relative permittivity ( $\varepsilon_r$ ) of a lossy dielectric medium can be expressed in a complex form as  $\varepsilon_r = \varepsilon' - j\varepsilon''$ , in which the ratio of the imaginary and the real parts defines the tangent of dielectric loss angle (i.e.,  $\tan \delta$ ) [55].

By substituting (3.2) into (3.1), it turns into a generalized linear eigensystem problem, which can provide us with the cut-off frequencies of vertically polarized modes. We can calculate the effective permittivity of each corresponding mode from its cut-off frequency. In other words, we should specify the wavenumber (i.e.,  $k_{x_0}$  and  $k_{y_0}$ ) and calculate the corresponding eigenvalue. The effective permittivity and the effective dissipation factor of each mode can be calculated as [55]:

$$\varepsilon_{\text{eff}} = \left( \frac{c_0}{2\pi} \frac{\partial k_0}{\partial \Re\{f\}} \right)^2 \quad (3.3)$$

$$\tan \delta_{\text{eff}} = \left( \frac{c_0}{2\pi} \frac{\partial k_0}{\partial \Im\{f\}} \right)^2 \quad (3.4)$$

where  $c_0$ ,  $k_0$ ,  $\Re\{f\}$ , and  $\Im\{f\}$  are the speed of light, defined wavenumber, and real and imaginary parts of the extracted cut-off frequency, respectively. The eigenvector of (3.1) will provide the field distribution of each mode inside the unit-cell.

The eigenvalue equation for the horizontally polarized mode (i.e.,  $E_{pq}^x$ ) inside a substrate

with circular perforations is expressed as:

$$\begin{aligned}
k_0^2 a_{(l,n)} = & - \sum_k \sum_m a_{(k,m)} b_{(k,m)} \left[ \left( \frac{2\pi l}{a} + k_{x_0} \right)^2 \right. \\
& + \left( \frac{2\pi n}{c} + k_{y_0} \right)^2 - \frac{2\pi(l-k)}{a} \left( \frac{2\pi l}{a} + k_{x_0} \right) \\
& \left. - \frac{2\pi(n-m)}{c} \left( \frac{2\pi n}{c} + k_{y_0} \right) \right]
\end{aligned} \tag{3.5}$$

where

$$b_{(i,j)} = \frac{1}{\varepsilon_r} \delta_{(i,j)} - \left( \frac{1}{\varepsilon_r} - 1 \right) \frac{\pi b^2}{a^2} \frac{2J_1 \left( \sqrt{\left( \frac{2\pi i b}{a} \right)^2 + \left( \frac{2\pi j b}{a} \right)^2} \right)}{\sqrt{\left( \frac{2\pi i b}{a} \right)^2 + \left( \frac{2\pi j b}{a} \right)^2}} \tag{3.6}$$

By substituting (3.6) into (3.5), it turns into an ordinary eigensystem problem, which can provide us with the cut-off frequencies of horizontally polarized modes. This procedure is similar to the case of vertically polarized modes as described before. To provide a better insight into the behavior of this periodically perforated substrate, an alumina substrate with a thickness of  $d = 254 \mu m$ , which has relative permittivity equal to  $\varepsilon' = 9.4$  and loss tangent of  $\tan \delta = 6 \times 10^{-3}$  is considered to have two different circular periodic perforations. One with a periodicity of  $a = 290 \mu m$  and diameter of  $b = 264.6 \mu m$ , and the other with a periodicity of  $a = 170 \mu m$  and diameter of  $b = 144.6 \mu m$ . The extracted effective permittivity and dissipation factor of these two cases are plotted in Fig. 3.2 and 3.3. The demonstrated results reveal that the structure has different responses (in terms of permittivity and loss tangent) for vertically and horizontally polarized modes meaning that the structure has anisotropic behavior [57]. It is worth mentioning that the effective permittivity and dissipation factor of an alumina substrate in the frequency ranges up to 335 GHz was measured at the *Poly-Grames Research Center*. The achieved results demonstrate that the alumina has constant permittivity and dissipation factor over the WR-5.1 and WR-3.5 band.

Accurate extraction of the effective permittivity and dissipation factor of the perforated regions enables us to use an equivalent model instead of the original SIIG structure. As shown in Fig. 3.1b, an equivalent model can be constructed by replacing the perforated regions with equivalently uniform dielectric layers with relative permittivity equal to the calculated effective permittivity. It is worth mentioning that the effective permittivity and dissipation factor of the perforated regions are highly dispersive (i.e., resulting effective permittivity and dissipation factor changes with frequency). Therefore, values of the effective permittivity and

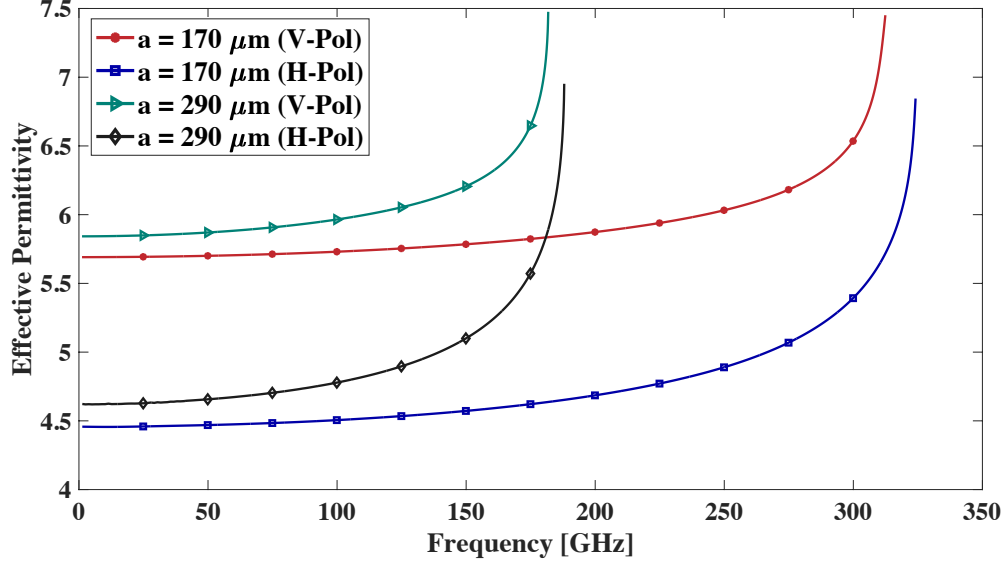


Figure 3.2 Extracted effective permittivity of the alumina substrate with different size of circular perforations.

dissipation factor should be selected according to the corresponding frequency. We can use this equivalent structure for the next step and apply the proposed modal analysis to extract all propagating modes through the guiding channel.

As shown in Fig. 3.4a, the equivalent model has material variation in two directions (here  $x$ , and  $y$  directions). The *modified effective dielectric constants* approach is used to extract the propagating modes [84]. This approach splits the original structure into two simple sub-structures, which can be analyzed much more straightforwardly. The first sub-structure is considered to have material variation only along the  $y$  direction, as shown in Fig. 3.4b. The effective dielectric constant of this combination (i.e., the lossy dielectric layer plus the top free-space layer) and the propagation constant along the  $y$  direction (i.e.,  $k_y$ ) will be extracted through the first stage. In the second stage, this combination will be replaced by a single uniform layer with relative permittivity equal to the extracted effective dielectric constant, which enables us to calculate the propagation constant along the  $x$  direction (i.e.,  $k_x$ ). Having the propagation constants along the  $x$  and  $y$  directions allows us to calculate the propagation constant along the  $z$  direction. The extracted  $k_z$  is a complex number that provides phase and attenuation constants (i.e.,  $\beta$  and  $\alpha$ ) along the guiding channel.

SIIG structure and its equivalent waveguide can support wave propagation in two possible field configurations:  $E_{pq}^y$  (vertically polarized) and  $E_{pq}^x$  (horizontally polarized) modes. The subscripts  $p$  and  $q$  indicate the number of electric field extrema along the  $x$ , and  $y$  directions,

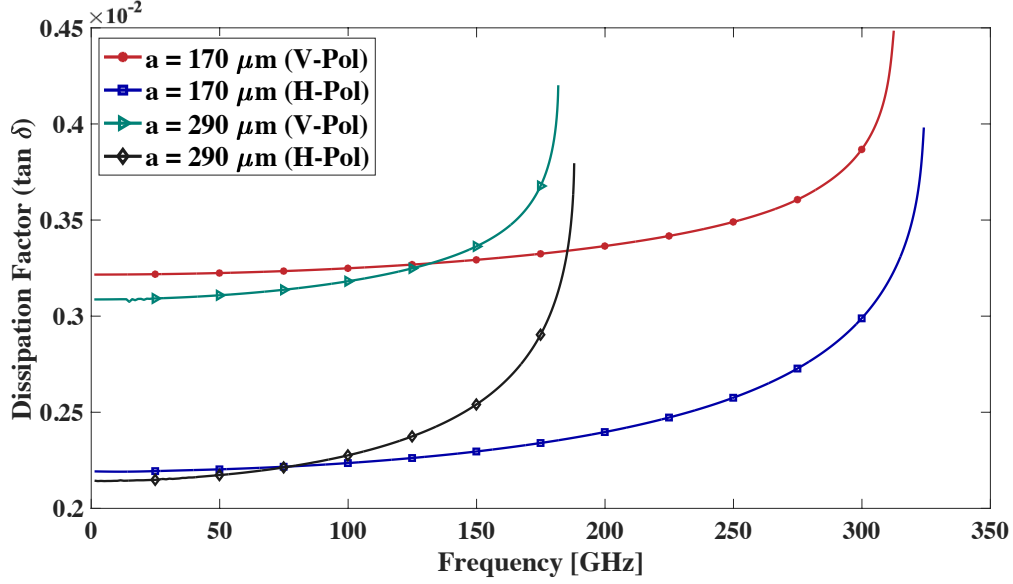


Figure 3.3 Extracted dissipation factor of the alumina substrate with different size of circular perforations.

respectively. According to the procedure proposed in [84], for the vertically polarized mode (i.e.,  $E_{pq}^y$ ) in *Region II*, solution of (3.7) provides the propagation constant along the  $y$  direction. The lowest value of  $k_y$  corresponds to the fundamental mode  $E_{p1}^y$ , the second value corresponds to the  $E_{p2}^y$  mode, and so on.

$$(\eta_0 \varepsilon_1 + \eta_m \varepsilon_0 \varepsilon_1) \cdot k_y \cdot \cos(k_y \cdot d) + (\eta_0 \eta_m \varepsilon_1^2 - \varepsilon_0 k_y^2) \sin(k_y \cdot d) = 0 \quad (3.7)$$

where  $\eta_0 = \sqrt{\mu_0 / \varepsilon_0}$  is the free-space impedance.  $\varepsilon_0$ ,  $\varepsilon_1$ ,  $k_y$ , and  $d$  are the free-space permittivity, the relative permittivity of the perforation region, the propagation constant along the  $y$  direction, and the thickness of the substrate, respectively.  $\eta_m$  is the intrinsic impedance of the ground plane and can be expressed as:

$$\eta_m = \sqrt{\frac{j\omega\mu_m}{\sigma_m + j\omega\varepsilon_m}} \quad (3.8)$$

where  $\mu_m$ ,  $\varepsilon_m$ , and  $\sigma_m$  are the permeability, permittivity, and conductivity of the metal, respectively. After achieving the values of  $k_y$ , the effective permittivity of the structure can be calculated by [84]:

$$\varepsilon_{e1} = \varepsilon_1 - \frac{k_y^2}{k_0^2} \quad (3.9)$$

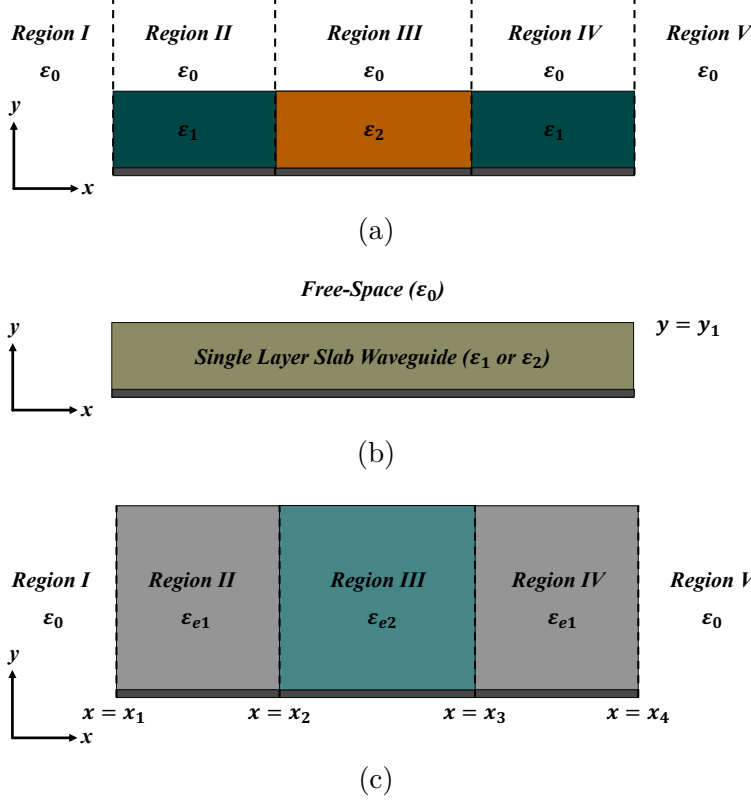


Figure 3.4 Modal analysis structures: (a) SIIG equivalent model, (b) the first stage sub-structure, and (c) the second stage sub-structure.

where  $\epsilon_{e1}$  and  $k_0$  are the effective permittivity of the perforated region and the free-space wave-number. Since the structure is considered to have dielectric and conductor losses, the extracted propagation constant  $k_y$  is a complex number that provides phase and attenuation constants along the  $y$  direction. Consequently, the extracted effective permittivity (i.e.,  $\epsilon_{e1}$ ) is a complex number that includes the effective permittivity and dissipation factor. Here it is worth mentioning that since the SIIG has two different substrate sections (i.e.,  $\epsilon_1$  and  $\epsilon_2$ ), the effective permittivity of the guiding channel (i.e.,  $\epsilon_{e2}$ ) should be calculated through repeating the same procedure.

Through the aforementioned procedure, the effect of the top free-space layer was studied and considered in the calculated  $\epsilon_e$ . In this stage, the dielectric layer and the free-space layer are replaced with a single uniform dielectric layer having a relative permittivity equal to the calculated effective permittivity (see Fig. 3.4c). The eigenvalue equation (3.10) for  $k_x$  will be achieved after applying the boundary conditions and executing some mathematical

manipulations, as:

$$\cosh(\xi w_p) \left( T_3 + \frac{\eta_0}{k_x} T_4 \right) + \sinh(\xi w_p) \left( \frac{\eta_0}{\xi} T_3 + \frac{\xi}{k_x} T_4 \right) = 0 \quad (3.10)$$

where

$$T_1 = \cosh(\xi w_p) + \frac{\xi}{\eta_0} \sinh(\xi w_p) \quad (3.11a)$$

$$T_2 = \sinh(\xi w_p) + \frac{\xi}{\eta_0} \cosh(\xi w_p) \quad (3.11b)$$

$$T_3 = T_1 \cdot \cos(k_x w_g) - T_2 \cdot \frac{k_x}{\xi} \sin(k_x w_g) \quad (3.11c)$$

$$T_4 = T_1 \cdot \sin(k_x w_g) + T_2 \cdot \frac{k_x}{\xi} \cos(k_x w_g) \quad (3.11d)$$

$\xi$ ,  $w_p$ ,  $w_g$ , and  $k_x$  are the propagation constant in the perforation region, the width of the perforation region, the width of the guiding channel, and the propagation constant in the guiding channel along the  $x$ -direction, respectively. The propagation constant along the  $x$ -direction in the guiding channel can be achieved by finding the eigenvalue solutions of (3.10). The lowest value of  $k_x$  corresponds to the fundamental mode  $E_{1q}^y$ , the second value corresponds to the  $E_{2q}^y$  mode and so on. The relation between propagation constants in different regions can be expressed as:

$$\eta_0 = \sqrt{(\varepsilon_{e2} - \varepsilon_0)k_0^2 - k_x^2} \quad (3.12a)$$

$$\xi = \sqrt{(\varepsilon_{e2} - \varepsilon_{e1})k_0^2 - k_x^2} \quad (3.12b)$$

Finally, the propagation constant  $k_z$  can be calculated as:

$$k_z^2 = \varepsilon_0 k_0^2 + \eta_0^2 = \varepsilon_{e1} k_0^2 + \xi^2 = \varepsilon_{e2} k_0^2 - k_x^2 \quad (3.13)$$

The same procedure can be followed to extract the propagation constant  $k_z$  for the horizontally polarized modes (i.e.,  $E_{pq}^x$ ). In order to provide a better insight into the behavior of the SIIG structure, an alumina substrate with a thickness of  $d = 254 \mu m$ , which has relative permittivity equal to  $\varepsilon' = 9.4$  and loss tangent of  $\tan \delta = 6 \times 10^{-3}$  is considered to be placed on an aluminum ground plane which has electric conductivity equal to  $\sigma_m = 3.56 \times 10^7 S/m$ , relative permeability equal to  $\mu_m = 1$ , and relative permittivity equal to  $\varepsilon_m = 1.000021$ . The aforementioned materials were used to create two different SIIG structures: one with a guiding channel of  $w_c = 450 \mu m$ , and five rows of circular perforations with a periodicity



equal to  $a = 290 \mu m$  and a diameter of  $b = 264.6 \mu m$ , and the other with a guiding channel of  $w_c = 330 \mu m$ , and five rows of circular perforations with a periodicity equal to  $a = 170 \mu m$  and a diameter of  $b = 144.6 \mu m$ . The phase constant ( $\beta$ ) and attenuation constant ( $\alpha$ ) of different propagating modes of the above SIIG structures are extracted and shown in Figs. 3.5 and 3.6, respectively.

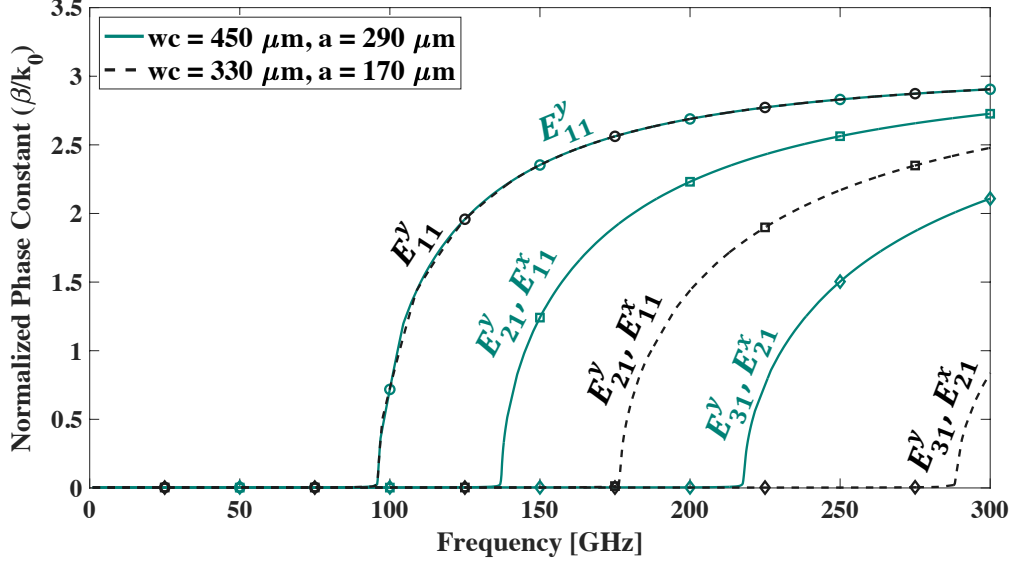


Figure 3.5 Extracted normalized phase constant of a few first modes of mentioned SIIG structures.

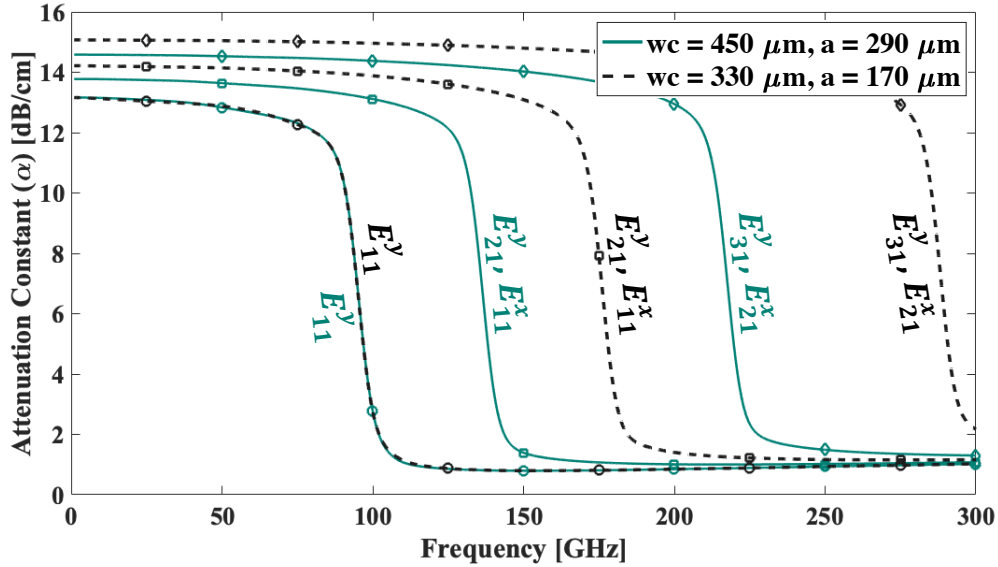


Figure 3.6 Attenuation constant of a few first modes of mentioned SIIG structures.

### 3.3 SIIG Design Parameters And Procedure

As shown in Fig. 3.1a, the SIIG structure includes several design parameters which can be controlled independently. A large number of design parameters provide enormous flexibility for the SIIG structure while making the design procedure more complicated. In the following sections, we study the effects of these parameters on the bandwidth, attenuation, and substrate leakage of the SIIG waveguide.

To avoid mode conversion and disturbing interference, it is usually a good idea to operate in the frequency range where only the fundamental mode of the waveguide propagates. Field confinement in the guiding channel determines the lower frequency limit. Weak field confinement produces high radiation levels at discontinuities and must be avoided. The cut-off frequency of the next higher-order mode (i.e.,  $E_{21}^y$ ) determines the upper frequency limit. It is worth mentioning that the transition from divergence to guidance is not sharp.

The operating frequency range of the SIIG strongly depends on the substrate's permittivity and thickness, along with the width of the guiding channel. According to [84], the substrate's permittivity determines all modes' cut-off frequencies, which defines the lower bandwidth limit. To demonstrate this effect, a dielectric substrate with a thickness of  $d = 254 \mu m$ , which has a loss tangent of  $\tan \delta = 6 \times 10^{-3}$ , is considered to have a relative permittivity that varies from 6 to 14. The circular perforations with a periodicity of  $a = 290 \mu m$  and diameter of  $b = 264.6 \mu m$  were added to the substrate. As demonstrated in Fig. 3.7, the cut-off frequency of the fundamental mode decreases by increasing the permittivity of the substrate. The thickness of the substrate (i.e.,  $d$ ) is another parameter that determines the propagating modes' cut-off frequency. As shown in Fig. 3.8, the cut-off frequencies increase by decreasing the substrate's thickness.

The upper limit of the single-mode bandwidth can be defined by the cut-off frequency of the next higher-order mode. The width of the guiding channel (i.e.,  $w_c$ ) is the parameter that strongly affects this cut-off frequency. As shown in Fig. 3.9, a wider guiding channel gives the next higher-order mode a lower cut-off frequency while the fundamental mode's cut-off frequency remains the same. Ideally, a narrower guiding channel provides a wider usable single-mode bandwidth. The unloaded line  $Q$ -factor is another parameter that can provide useful information on the cut-off frequencies of the propagating modes. Fig. 3.10 demonstrates the unloaded  $Q$ -factor of the first and second modes. When the  $Q$  factor for the fundamental mode has nearly reached its quasi-constant value, the lower bandwidth limit is reached. As the  $Q$  factor for the second mode starts to increase rapidly, the upper bandwidth

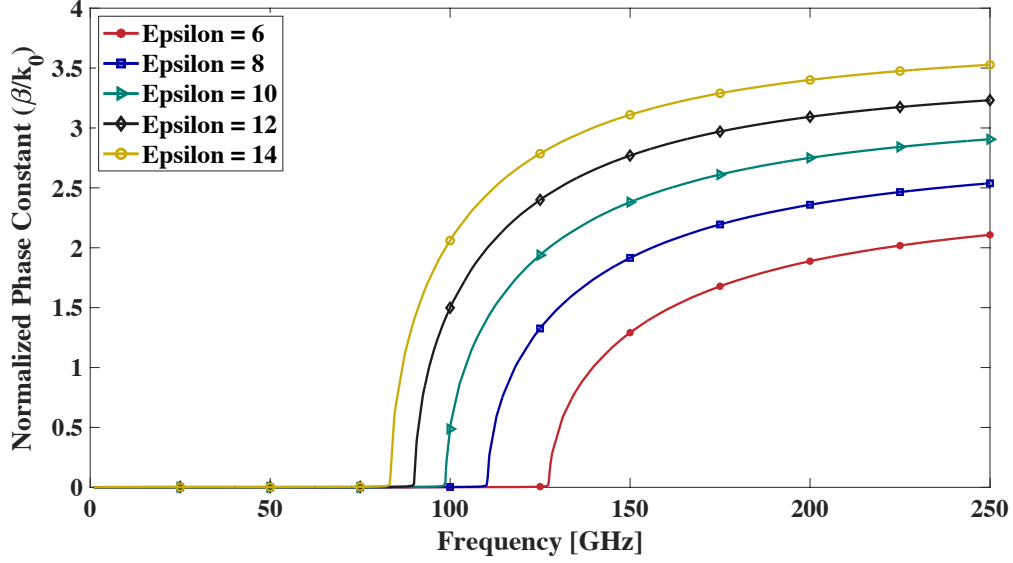


Figure 3.7 Extracted normalized phase constant of the fundamental mode of the mentioned SIIG structure with different substrate permittivity.

limit is reached. This indicates that the mode has crossed the divergence frequency.

The loss tangent of the substrate (i.e.,  $\tan \delta$ ) is one of the primary sources of attenuation in the SIIG waveguide. As shown in Fig. 3.11, according to equation (3.7), the total attenuation of the SIIG structure increases by increasing the dielectric loss tangent. However, due to the material availability, we have limited options in selecting the substrate materials. Conductor loss is another source of attenuation in the SIIG structure. As shown in Fig. 3.12 and according to (3.7), the total attenuation of the SIIG waveguide decreases by increasing the conductivity of the ground plane (i.e.,  $\sigma_m$ ). It is worth mentioning that the dielectric loss of the substrate and conductor loss of the ground plane have no impact on the operating bandwidth of the SIIG waveguides.

Typically, high contrast of permittivity of the guiding channel and the adjacent regions should be realized to achieve the highest possible power transmission along dielectric waveguides [33]. As mentioned before, in the SIIG waveguide, this contrast is realized by adding periodic air perforations in the bilateral regions. Periodicity, size, and pattern of the perforations (i.e.,  $a$  and  $b$ ) are set to define the resulting permittivity and the consequent field leakage into the bilateral regions. To be specific, lower effective permittivity for the perforation region (which is a function of the  $a$ , and  $b$ ) allows higher power transmission along the SIIG's guiding channel. Accordingly, based on the fabrication limitation, the maximum achievable size should be considered for the perforations.

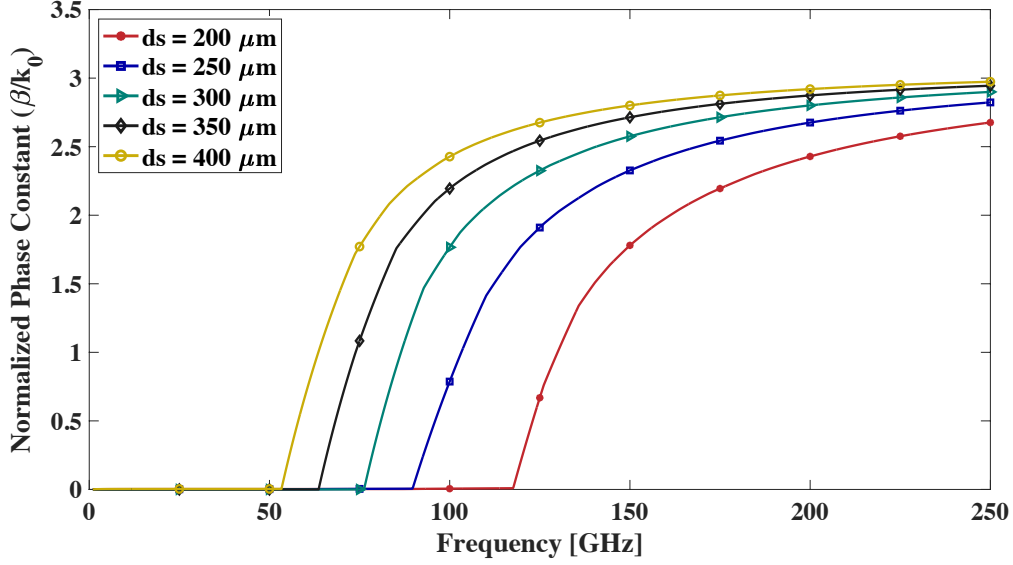


Figure 3.8 Extracted normalized phase constant of the fundamental mode of the mentioned SIIG structure with different substrate thickness.

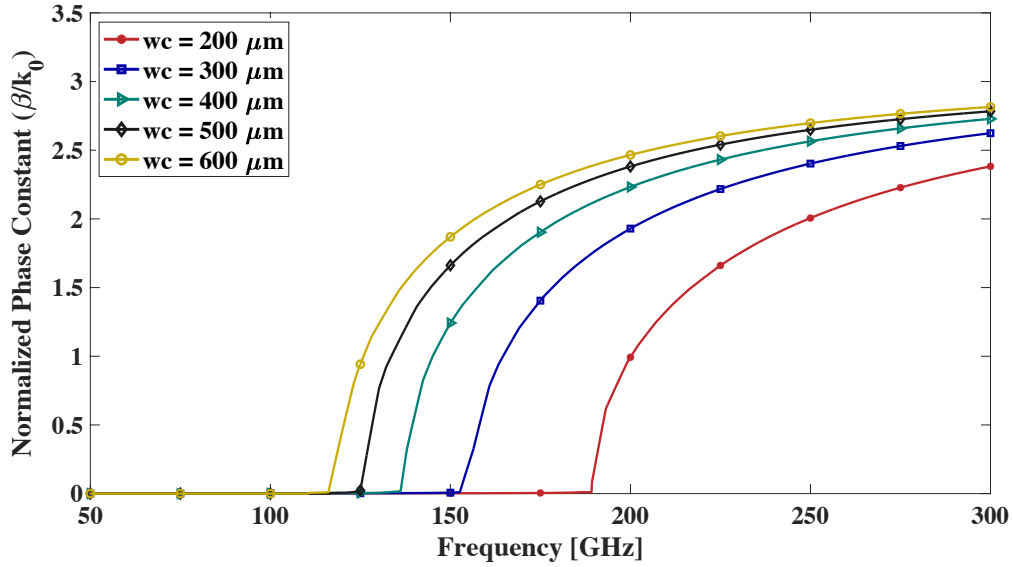


Figure 3.9 Extracted normalized phase constant of the second order mode of the mentioned SIIG structure with different guiding channel width.

The presence of periodic perforations in the guiding direction of the SIIG waveguide results in an electromagnetic band gap (EBG) caused by the *distributed Bragg reflection* of the guided mode [85]. The lowest EBG occurs when the guided wavelength  $\lambda_g$  equals twice the periodic interval  $a$  (i.e.,  $\lambda_g = 2a$ ). Accordingly, the perforations' periodicity must be chosen small enough to avoid the aforementioned stopband in the operating frequency range of

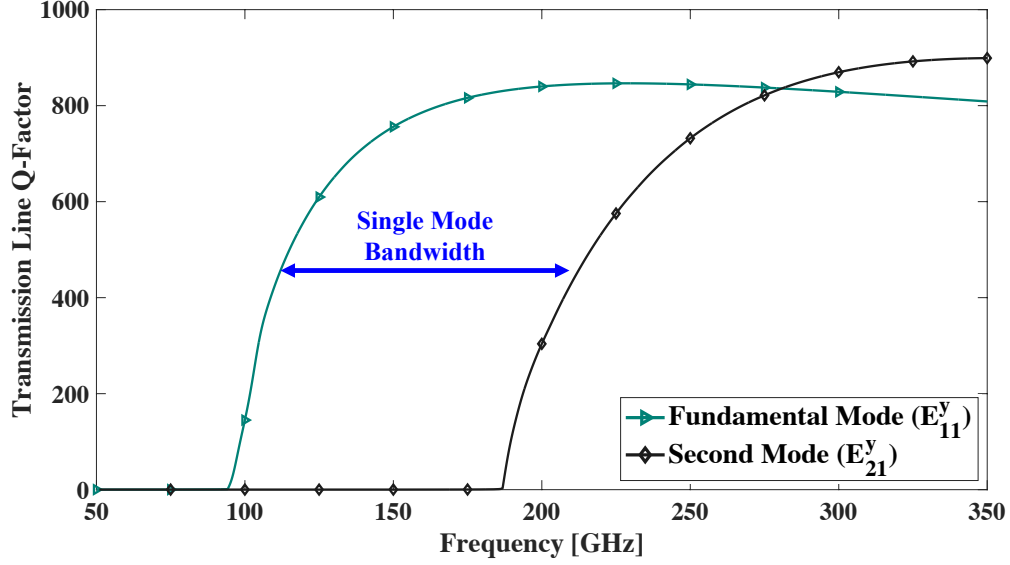


Figure 3.10 Extracted usable single mode bandwidth based on the unloaded Q-factor of the fundamental and second mode.

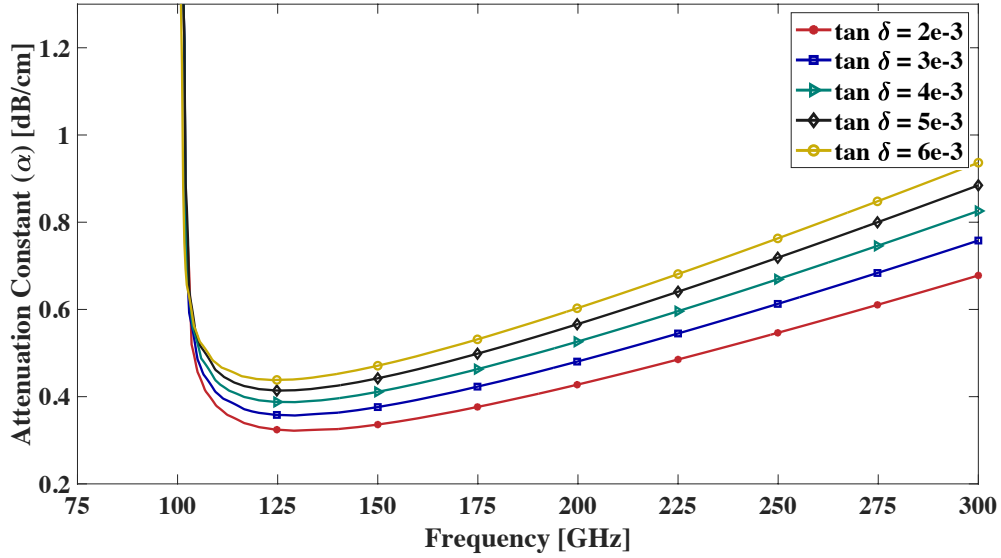


Figure 3.11 Extracted attenuation constant of the fundamental mode of the mentioned SIIG structure with different substrate dissipation factor.

the SIIG waveguide. Undoubtedly, the perforation periodicity could always be chosen finer than required, which would, however, increase the fabrication complexity and decrease the mechanical stability. A regular triangular perforation pattern and maximum obtainable perforation diameter (i.e.,  $b$ ) should be considered, which allows the highest substrate removal. This way, the maximum permittivity contrast can be achieved, thus yielding the best guiding

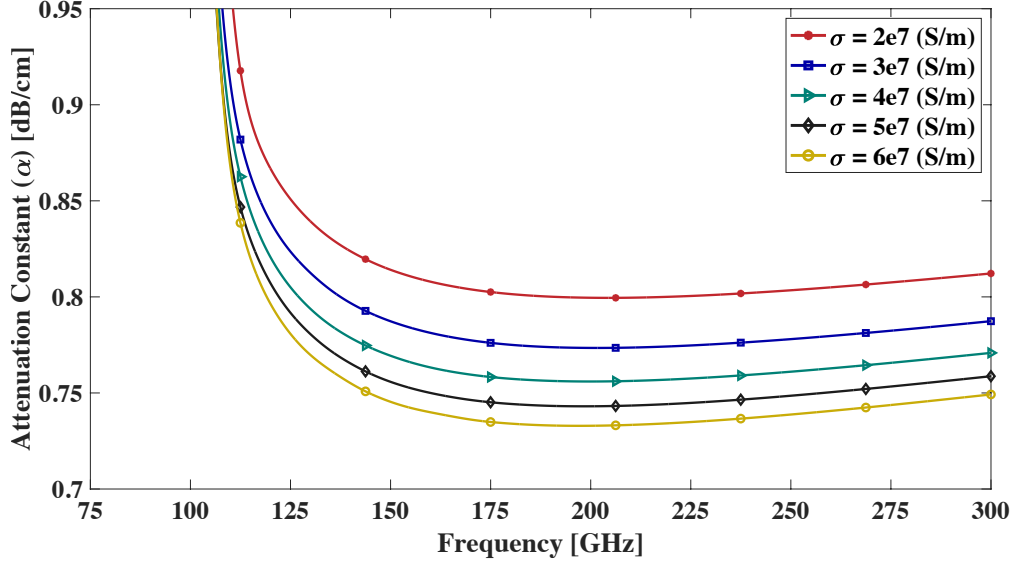


Figure 3.12 Extracted attenuation constant of the fundamental mode of the mentioned SIIG structure with different ground plane's conductivity.

properties possible.

### 3.4 Fabrications And Measurements

According to the above parameters study and based on the material available at the *Poly-Grames Research Center*, an alumina ( $\epsilon_r = 9.4$  and  $\tan \delta = 6 \times 10^{-3}$ ) substrate with a thickness of  $d = 254 \mu m$  is utilized to create two SIIG structures. The circular perforation and the regular triangular pattern are chosen as the most efficient pattern to achieve the highest possible substrate removal. For the first prototype, the operating frequency range of the proposed SIIG waveguide is considered to be in the WR-5.1 band (i.e., 135 to 225 GHz). To have the Bragg electromagnetic bandgap accrued far away from the operating region, the perforation periodicity is considered to be equal to  $a = 290 \mu m$ , which leads the lowest EBG to have a central frequency of 245 GHz. Larger perforations provide a higher permittivity contrast between the perforated regions and the guiding channel, which leads to higher power transmission. However, due to the fabrication limitation, a minimum 1 mil (i.e.,  $25.4 \mu m$ ) wall should be kept between adjacent perforations to ensure the mechanical stability of the fabricated structure. According to the analytical model, these perforation properties lead the bilateral regions to have effective permittivity and dissipation factor equal to the values shown in Figs. 3.2 and 3.3. The proposed SIIG structure is considered to have a guiding channel width of  $w_c = 450 \mu m$ . Although the SIIG is a planar waveguide, as shown in Fig.

3.13, the structure is fed with a WR-5.1 rectangular waveguide.

To achieve an efficient transition between these two waveguides, it is essential to design a well-optimized interface that seamlessly connects the SIIG structure and the rectangular waveguide. To minimize return loss, a smoothly tapered dielectric section can be employed. The taper can be considered as a special case of stepped transformers, where the number of steps is infinite, and their individual reflections are infinitesimally small. The design objective is to achieve the widest possible bandwidth with the shortest possible tapers. Accordingly, the SIIG waveguide is tapered with a length of 3.07 mm at both ends. It is worth mentioning that most parts of the losses in the fabricated prototype are due to the feeding mismatch. To remove this loss and accurately measure the transmission loss, the dual-line technique is used [4]. Two SIIG structures differing in length (i.e., 20mm and 30mm) are fabricated, and the propagation constant is extracted subsequently from the pair of measured S-parameters, as:

$$\beta = \frac{|\angle \mathbf{S}_{21,\text{long}} - \angle \mathbf{S}_{21,\text{short}}|}{\Delta l} \quad (3.14a)$$

$$\alpha = \frac{-\ln(|\mathbf{S}_{21,\text{long}}| / |\mathbf{S}_{21,\text{short}}|)}{\Delta l} \quad (3.14b)$$

where  $\Delta l$  is the length difference,  $\angle \mathbf{S}_{21,\text{long}}$  and  $\angle \mathbf{S}_{21,\text{short}}$  denote the absolute phase (in radians) of the measured complex S-parameters of the long and the short fabricated SIIG sections, respectively. As shown in Fig. 3.14, the mentioned SIIG waveguide was fabricated and tested at the *Poly-Grames Research Center*. The measured S-parameters of the fabricated SIIG structures are shown in Fig. 3.15, which demonstrates an excellent agreement with the simulation results. The *CST Studio Suite 2022* software was employed to simulate the aforementioned SIIG structure. The simulations were performed in the frequency domain using a broadband sweep with 5000 data sample points. To maintain precision, a tetrahedral meshing technique combined with activated adaptive mesh refinement was adopted. Since the measurement equipment (i.e., WR-5.1 waveguide and measurement extender) has a recommended operating frequency band of 135 GHz to 225 GHz, the frequency range plotted in Fig. 3.15 is thus limited. Taking into account that the simulated reflection coefficient (i.e.,  $S_{11}$ ) remains consistently below -17 dB across the bandwidth of interest, this value has been omitted from this figure to enhance the visibility of other depicted parameters. It is worth mentioning that the measured results include feeding mismatch losses. However, it is important to note that in the context of substrate-integrated circuit (SIC) applications for which the SIIG does not require rectangular waveguide feeding, the feeding mismatch losses

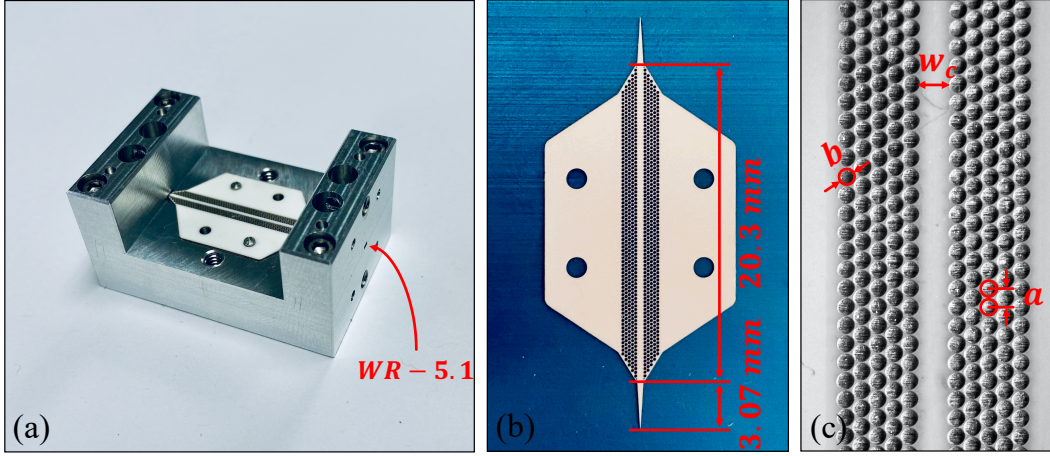


Figure 3.13 a) The fabricated SIIG structure fed by WR-5.1 waveguide, b) the fabricated alumina substrate having 5 rows of circular perforations, c) zoomed view of the guiding channel and adjacent perforated regions.

can be eliminated. According to the measurement and based on the dual-line technique, the fabricated SIIG has a mean insertion loss of  $IL = 0.578$  dB/cm in the WR-5.1 band. Here it is worth mentioning that the achieved insertion loss can be reduced by using a substrate with smaller dielectric losses. Through careful selection of appropriate dimensions, the WR-5.1 rectangular waveguide, which serves as the feeding mechanism for the investigated SIIG structures, has been tailored to possess specific cut-off frequencies for its first and second modes (i.e., 115.714 GHz and 231.429 GHz) [86]. As a result, this waveguide operates in a single mode consistently within the specified frequency range (i.e., 135GHz to 225 GHz). To ensure optimal performance, we meticulously adjusted the parameters of the SIIG structure (i.e.,  $w_c$  and  $d$ ), aligning its first and second mode cut-off frequencies with those of the WR-5.1 rectangular waveguide. This alignment effectively prevents the excitation of higher-order modes, promoting reliable and accurate operation. Furthermore, in line with the dual-line technique, identical feeding structures (i.e., WR-5.1 rectangular waveguide and taper) for both SIIG structures were employed. This strategic choice offers the advantage of eliminating return losses caused by any potential misalignment between the rectangular waveguide and the investigated SIIG.

To demonstrate a true potential of the SIIG waveguide for use in the THz applications, the



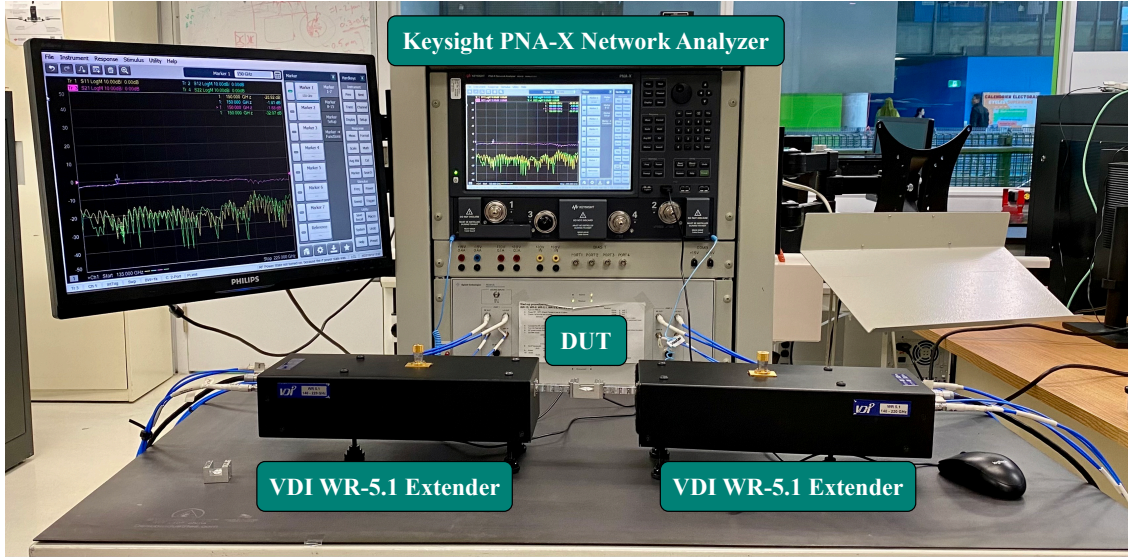


Figure 3.14 Measurement setup used to extract the S-parameters of the SIIG waveguide in WR-5.1 Band.

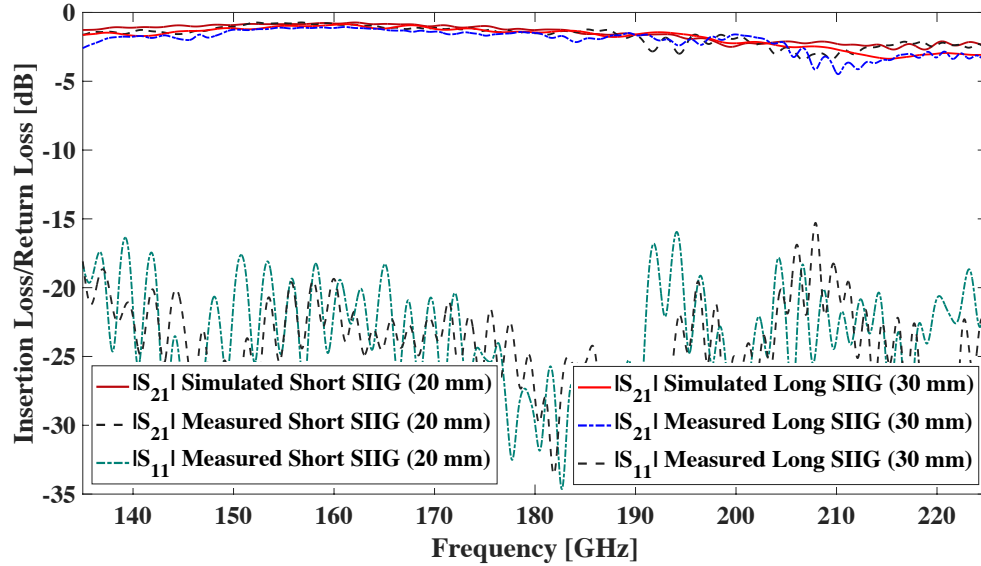


Figure 3.15 Simulated and measured insertion loss and return loss of the SIIG prototype in the WR-5.1 band.

other SIIG prototype structure is fabricated for the WR-3.5 frequency band (i.e., 215 GHz to 335 GHz). The same alumina substrate ( $\epsilon_r = 9.4$  and  $\tan \delta = 6 \times 10^{-3}$ ) with a thickness of  $d = 254 \mu\text{m}$  is utilized to create this prototype. As shown in Fig. 3.16, five rows of circular

perforation with a periodicity of  $a = 170 \mu m$  are added to the bilateral regions which makes the lowest EBG to have a central frequency of 410 GHz. Based on the fabrication limitation a minimum  $25.4 \mu m$  wall is considered between the perforations which forces a maximum size of  $b = 144.6 \mu m$  for the air holes. According to the analytical model, these perforation properties lead the bilateral regions to have effective permittivity and dissipation factor equal to the values shown in Figs. 3.2 and 3.3. The proposed SIIG structure is considered to have a guiding channel width of  $w_c = 330 \mu m$ . The SIIG waveguide is tapered with a length of 2.72 mm at both ends for impedance matching between the air-filled standard WR-3.5 rectangular waveguide and the SIIG section. Similar to the previous fabrication, the same SIIG structures with two different lengths (i.e., 15mm and 25mm) are fabricated to remove the feeding loss from the measurement using the aforementioned dual-line technique. S-parameters of the SIIG prototypes measured using the same measurement setup and WR-3.5 waveguide and measurement extender and shown in Fig. 3.17. It is worth mentioning that, since the WR-3.5 measurement extender has a recommended operating frequency range of 215 GHz to 335 GHz, the frequency range of this figure is limited to these values. It is worth mentioning that the measured results include feeding mismatch losses. According to the measurement and based on the dual-line technique, the fabricated SIIG has a mean insertion loss of  $IL = 1.431 \text{ dB/cm}$  over the WR-3.5 band.

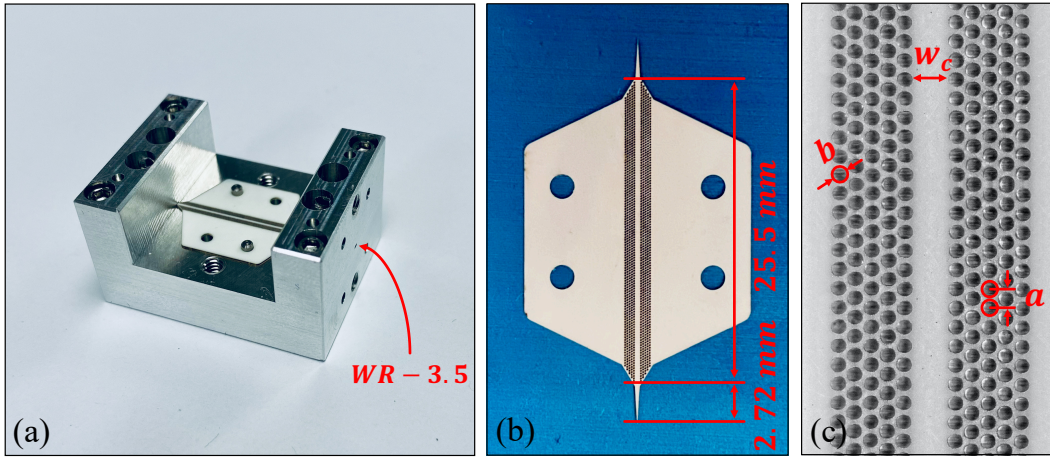


Figure 3.16 a) The fabricated SIIG structure fed by WR-3.5 waveguide, b) the fabricated alumina substrate having 5 rows of circular perforations, c) zoomed view of the guiding channel and adjacent perforated regions.

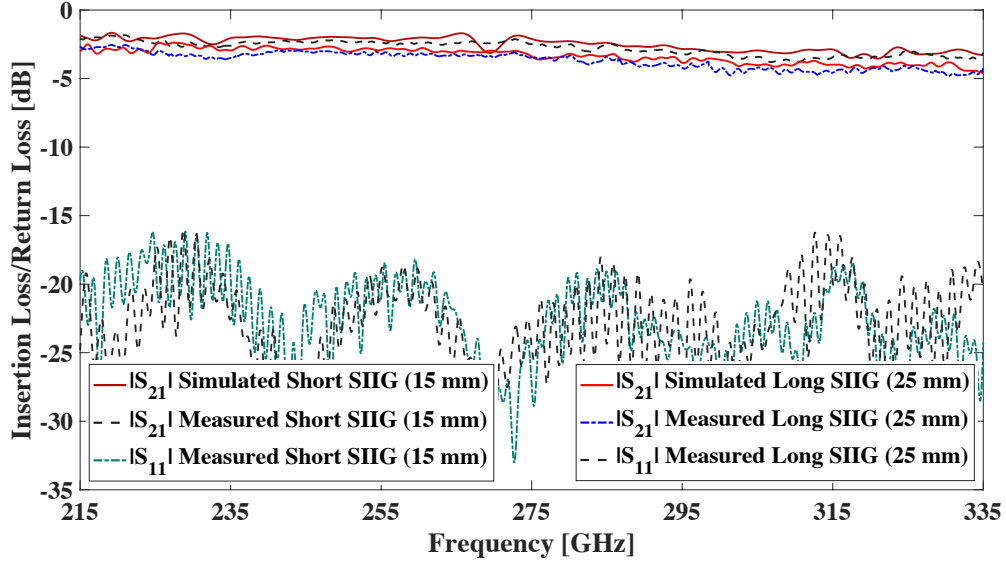


Figure 3.17 Simulated and measured insertion loss and return loss of the SIIG prototype in the WR-3.5 band.

### 3.5 Comparison

In this section, a comparison between the achieved results from the proposed SIIG and other existing technologies at THz bands is conducted and reported in TABLE 3.1. Although conventional rectangular waveguides (RW) provide low-loss wave transmission, they suffer from a lack of compactness which is critical for integrated circuit applications. Additionally, due to the strict requirement of electrical contacts between the waveguide blocks, RWs require a precise and costly manufacturing process [60]. Another low transmission loss THz technology is Gap waveguides. However, similar to rectangular waveguides, gap waveguides suffer from a lack of compactness. Furthermore, a small air gap of  $\lambda/4$  needs to be maintained all over the parallel plates, which becomes extremely small and very difficult to realize at such frequencies [65]. Cavity-backed Coplanar Waveguide (CBCPW) proved to have an acceptable transmission loss in the THz regime, however, similar to the RW and Gap waveguides, it suffers from bulkiness and lack of compactness [87]. Pure dielectric waveguides exhibit excellent potential for developing THz circuits and antennas due to their relatively low transmission losses. As shown in TABLE 3.1, Silicon Dielectric Ribbon [44], Effective-Medium-Clad Dielectric Waveguides [43], Silicon-on-Glass Dielectric [88], and Narrowed Dielectric Microstrip Line [45] provide low-loss wave transmission. However, the aforementioned dielectric waveguides suffer from complex and costly fabrication which prevents them from being used for large-scale industrial production. These waveguides are extremely fragile, and their low

field confinement yields considerable leakage around the guiding channel. Since no metallic ground plane is used in their structure, their integration with other circuit components will be challenging to realize. Due to its planar structure, the Substrate-Integrated Hybrid Metallo-Dielectric (SIHMD) [81] waveguide offers excellent alignment precision, compromised loss performance, and simplified interconnection with other SIC components. However, its fabrication process is complex, expensive, and time-consuming. Additionally, the SIHMD waveguide experiences challenges such as potential mode conversion and disturbing interference at the SIDW and SINRD interfaces. It is important to highlight that the SINRD section exhibits significantly higher transmission losses in comparison to the SIDW section [81]. This discrepancy in insertion losses primarily arises from the conductor losses, which escalate with the length of the SINRD section. Consequently, the length of the SINRD section has intentionally been kept short to ensure that the total insertion loss remains within an acceptable range. When evaluating waveguides, it is crucial to consider diverse trade-offs they offer in terms of performance, fabrication complexity, compactness, and cost. In the realm of substrate-integrated circuit (SIC) applications, where the integration of multiple circuit components and overall system compactness are of paramount importance, certain factors become particularly important. Despite its higher loss, the investigated SIIG waveguide emerges as a practical and cost-effective solution that aligns well with the requirements of SIC technology.

### 3.6 Conclusion

Substrate-Integrated Image Guide (SIIG) can deliver the highest performance for the THz applications when properly designed. Due to its low-loss wave transmission, planar structure, and shared ground plane, the SIIG is an excellent candidate for THz integrated circuits and systems. Through structural analysis, we realized that high performance in the THz regime can be achievable by choosing proper values for the structural design parameters. In this work, we presented two wide-band and low-loss SIIG designs for the WR-5.1 and WR-3.5 frequency bands. The experimental results indicate that the first fabricated prototype exhibits a mean insertion loss of 0.578 dB/cm over a frequency range of 135 GHz - 225 GHz using the dual-line parameter extraction technique. The second fabricated prototype of SIIG achieved an average insertion loss of  $IL = 1.431$  dB/cm in the frequency range of 215 GHz - 335 GHz. The results demonstrate a true potential of the SIIG waveguides for use in the THz applications.

Table 3.1 Comparison of Measured Results among Different THz Transmission Lines.

Ref.	Type of Transmission Line	Test Band [GHz]	Fabrication Technology	Fabrication Cost	Integration Capability	Insertion Loss [dB/cm]
[60]	Rectangular Waveguide	220-330	Finish Machining	High	Low	$\leq 0.2$
[65]	Groove Gap Waveguide	220-320	Dry Film Photoresist Metal Coating	High	Low	0.48 (avg.)
[65]	Ridge Gap Waveguide	220-320	Dry Film Photoresist Metal Coating	High	Low	0.75 (avg.)
[87]	Cavity-Backed Coplanar Waveguide	220-325	DRIE Technology Metal Coating	High	Medium	$\geq 1.2$
[44]	Silicon Dielectric Ribbon Waveguide	140-220	DRIE Technology	Medium	Low	$\leq 0.087$
[43]	Effective-Medium-Clad Dielectric Waveguides	220-330	DRIE Technology	Medium	Medium	0.075 (avg.)
[88]	Silicon-on-Glass Dielectric Waveguide	140-170	DRIE Technology	Medium	Low	0.52 (avg.)
[45]	Narrowed Dielectric Microstrip Line	220-280	PCB	Low	Low	0.52 (avg.)
[81]	Substrate-Integrated Hybrid Metallo-Dielectric	240-330	YAG Laser Metal Coating	High	Medium	2.2 (avg.)
This Work	Substrate-Integrated Image Guide	135-225 215-335	YAG Laser	Low	High	0.578 (avg.) 1.431 (avg.)

## CHAPTER 4 SUBSTRATE-INTEGRATED HYBRID DIELECTRIC-METALLIC IMAGE GUIDE (SIHDMIG) ARCHITECTURE AND ITS APPLICATIONS IN DEVELOPING SUB-THZ/THZ POWER DIVIDER

### 4.1 Introduction

The demand for rapid data transfer in modern telecommunications and data communication systems, the need for enhanced precision and sensitivity in scientific research [27], medical imaging [28, 29], and industrial applications, as well as the requirement for high-capacity wireless communication in densely populated areas, collectively drive the utilization of THz signals, emphasizing their vital role in meeting these critical needs [89]. Moreover, the THz spectrum offers an exceptionally integrated system framework, a crucial element for developing smart devices that require the installation of a multitude of sensors and communication components.

While THz communication shares several foundational principles with its microwave counterpart, it grapples with a range of unique challenges. Notably, one of these challenges concerns the substantial transmission loss experienced in frontends, a challenge that is particularly pronounced in the THz spectrum. It's crucial to emphasize that as frequency increases, conductive losses escalate significantly, and the skin effect exacerbates these losses. Consequently, attenuation can extend to several tens of dB/cm [30–32]. Owing to this limitation, conventional metal-based technologies, such as microstrip, co-planar, and substrate integrated waveguide (SIW), prove unsuitable for high-frequency THz band circuit, antenna, and system applications.

Dielectric waveguides, well-established in photonic circuits, hold substantial promise for developing THz circuits and antennas thanks to their freedom from metallic losses. Various photonic-inspired guiding structures, such as hollow-core [36, 39], solid-core [40, 41], and porous-core waveguides [42, 43, 46], have demonstrated impressively low attenuation, ranging from 1.0 to 0.1 dB/cm in the THz region. Typically, metallic waveguides rely on field interactions with conducting currents to guide waves. However, in dielectric waveguides, wave guidance hinges on total internal reflections at the dielectric-dielectric (or air) interface.

It's worth noting that the hollow and porous-core waveguides inherently have larger geometries, limiting their utility in highly integrated THz systems. In contrast, the planar variants of solid-core waveguides, including silicon-on-insulator (SOI) waveguides [47, 48], di-

electric microstrip lines (DMLs) [49, 50], and dielectric photonic crystal waveguides [51–53], represent promising candidates for THz system applications. Nonetheless, these waveguides exhibit extreme fragility, and their low field confinement leads to considerable leakage around the guiding channel.

To enhance their structural stability, planar dielectric waveguides can be reinforced by adding a metallic ground plane. Beyond providing mechanical support, this metallic ground plane serves as one-sided shielding, capable of dissipating heat generated by active devices. Moreover, it expands the usable single-mode bandwidth by shifting higher-order modes to higher frequencies.

In the work detailed in [90], Knox et al. proposed a hybrid guiding structure named "Image Guide." This structure involves placing a high-permittivity rectangular dielectric line on a metallic ground plane and is among the simplest and most commonly employed dielectric waveguides. Image guide technology has been instrumental in the realization of a wide array of passive and active circuit components, underscoring the advantages of integrated dielectric technology [56, 58, 91]. While image guide structures offer the advantage of very low transmission losses, they do present certain challenges related to fabrication and integration. Particularly at high frequencies, the single dielectric strip possesses extremely small dimensions, necessitating a precise fabrication process. Additionally, ensuring the precise alignment of this small dielectric strip with other circuit components is crucial in integrated circuit applications.

The recently investigated "Substrate-Integrated Image Guide (SIIG)" takes inspiration from the "substrate-integrated circuit" concept and represents a streamlined adaptation of the image guide [84]. Much like the traditional image guide, the SIIG comprises a planar high-permittivity substrate positioned above a continuous metallic ground plane. To create the desired permittivity contrast between the guiding channel and the surrounding areas, periodic air perforations are introduced in these regions, effectively reducing the effective permittivity of these sections. Consequently, the SIIG achieves a guiding effect similar to the standard image guide, with the exception of specific characteristics attributed to the periodic perforations. The planar substrate simplifies the fabrication process, enhancing alignment precision with other integrated circuit components. Additionally, it streamlines the interconnection with other waveguide technologies on the same substrate.

While the SIIG waveguide demonstrates exceptional performance in straight-line configurations, it experiences issues with leakage at sharp bends. When the guided wave encounters these sharp turns, it begins to leak into the perforated regions, resulting in a degradation of performance, particularly with respect to insertion loss. These issues may limit the applica-

tions of SIIG technologies, especially in applications requiring sharp discontinuities, such as compact power dividers/combiners.

In this paper, a solution is presented to tackle the leakage challenges at sharp bends in SIIG waveguides. This solution involves the integration of a hybrid waveguide, formed by introducing a Substrate-Integrated Metallic Image Guide (SIMIG) waveguide into the SIIG structure. This innovation effectively prevents the guided wave from leaking into the perforated regions and enhances the overall performance of SIIG at sharp bends. Consequently, this breakthrough allows for the creation of a highly compact power divider/combiner using SIIG technology.

Accordingly, the rest of the paper is organized as follows: Section 4.2 conducts a comprehensive examination of the integration feasibility of the SIIG section and SIMIG section, employing mode matching, impedance matching and field matching techniques. Section 4.3 introduces the resultant hybrid waveguide and showcases its performance in handling sharp bends within the frequency bands of WR-5.1 and WR-3.5. Section 4.4 provides insights into the designed power divider/combiner prototypes and the corresponding extracted results. Finally, a brief conclusion is presented in Section 4.5.

## 4.2 Feasibility of Substrate-Integrated Hybrid Dielectric-Metallic Image Guide

### 4.2.1 Substrate-Integrated Image Guide (SIIG) Structure

As shown in Fig. 4.1a, the SIIG waveguide consists of a high-permittivity planar substrate placed on a metallic ground plane. Wave guidance happens in this waveguide due to the total internal reflections at the dielectric-air interface. To realize the permittivity contrast between the guiding channel and the bilateral sections, some air perforations are added to these regions, which artificially reduces their effective permittivity. It is worth mentioning that the size, shape, and pattern of these perforations are set to define the realized effective permittivity. This configuration exhibits excellent wave-guiding performance for the SIIG structure [92]. The field distribution of the fundamental mode (i.e.,  $E_{11}^y$ ) of the SIIG waveguide along the guiding channel and at the cross-section is presented in Fig. 4.2.

As illustrated in Fig. 4.1a, the SIIG structure encompasses several design parameters that can be adjusted independently. While these parameters offer considerable flexibility for the SIIG structure, they also introduce complexity to the design process. These variables encompass substrate material ( $\epsilon_r$  and  $\tan \delta$ ), substrate thickness ( $d$ ), guiding channel width ( $w_c$ ), perforation size ( $b$ ), perforation pattern, perforation periodicity ( $a$ ), and the ground plane material ( $\sigma_m$ ). It is crucial to emphasize that the selection of these design parameters



must be carried out with meticulous consideration to optimize the bandwidth, minimize attenuation, and mitigate substrate leakage in the SIIG section.

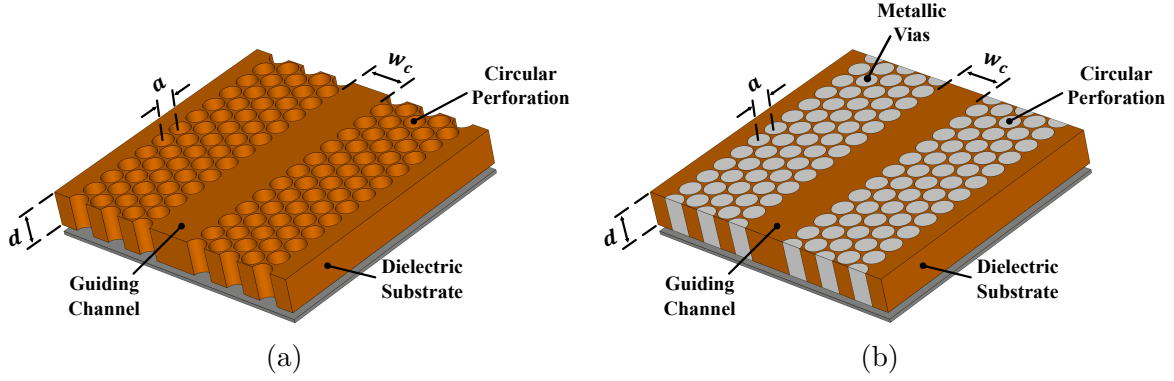


Figure 4.1 Exposed view of (a) Substrate-Integrated Image Guide (SIIG) structure and (b) Substrate-Integrated Metallic Image Guide (SIMIG) structure.

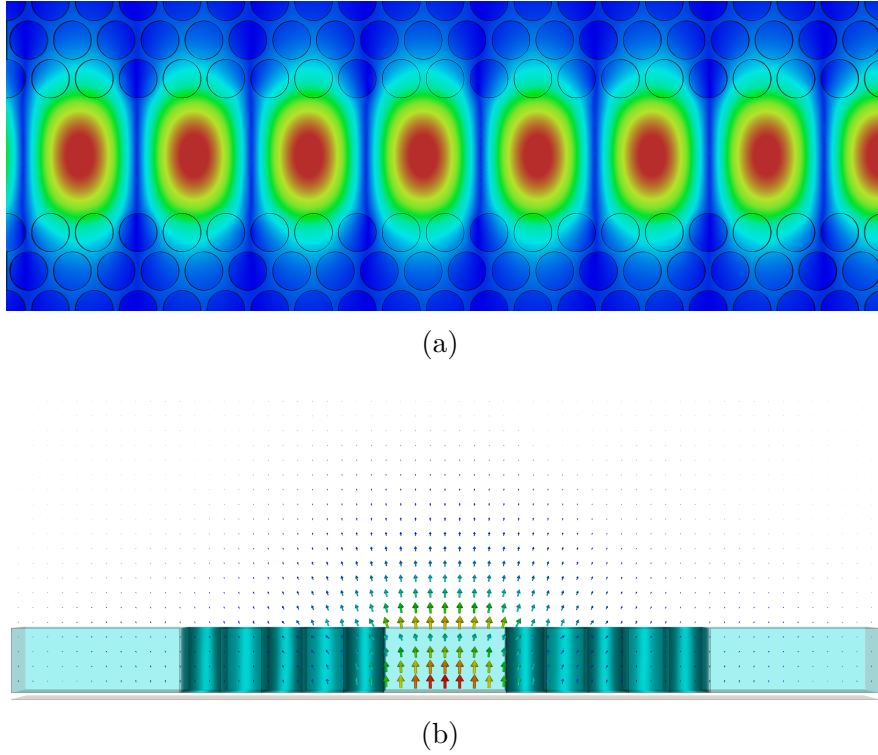


Figure 4.2 Field distribution of the fundamental mode (i.e.,  $E_{11}^y$ ) of the SIIG structure at the frequency of 150 GHz, (a) magnitude of the electric field along the guiding channel and (b) electric field distribution on the cross-section.

As studied in [92], an alumina substrate with a thickness of  $d = 254 \mu m$ , which has relative permittivity equal to  $\epsilon' = 9.4$  and loss tangent of  $\tan \delta = 6 \times 10^{-3}$  is considered to be placed on an aluminum ground plane which has electric conductivity equal to  $\sigma_m = 3.56 \times 10^7 S/m$ , relative permeability equal to  $\mu_m = 1$ , and relative permittivity equal to  $\epsilon_m = 1.000021$ . The aforementioned materials were used to create an SIIG structures with a guiding channel of  $w_c = 480 \mu m$ , and five rows of circular perforations with a periodicity equal to  $a = 185 \mu m$  and a diameter of  $b = 159.6 \mu m$ . Following the methodology outlined in reference [84], the phase constant ( $\beta$ ) and wave impedance of different propagating modes within the SIIG structure mentioned above are extracted and shown in Fig. 4.3, and 4.4, respectively.

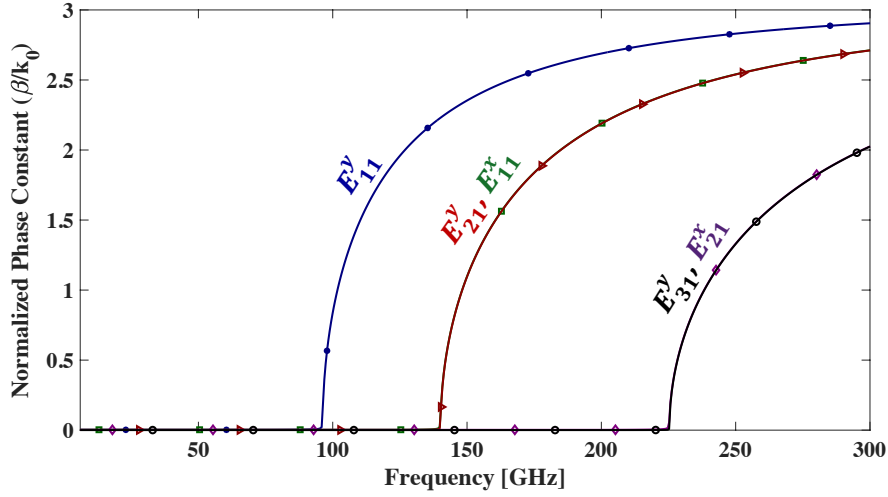


Figure 4.3 Extracted normalized phase constant of a few first modes of mentioned SIIG structures.

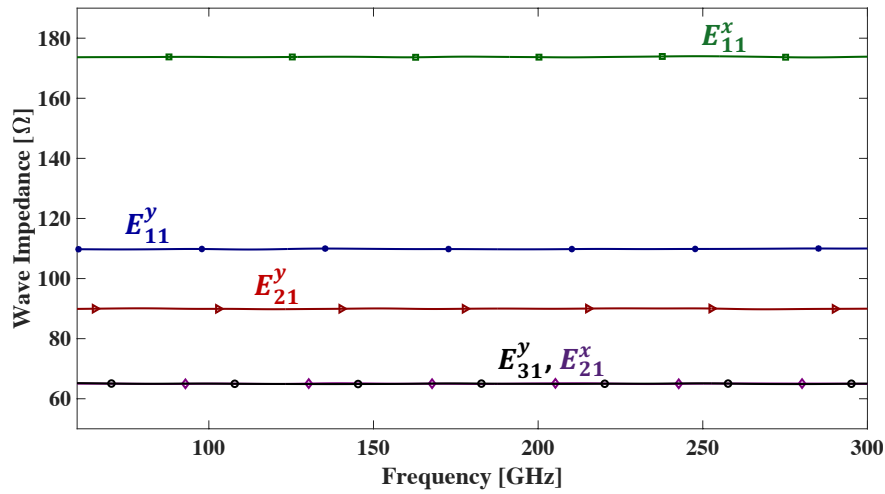


Figure 4.4 Wave impedance of a few first modes of mentioned SIIG structures.

#### 4.2.2 Substrate-Integrated Metallic Image Guide (SIMIG) Structure

As illustrated in Fig. 4.1b, by filling the air perforations with a highly conductive material, such as good conductors, a novel waveguide type known as the Substrate-Integrated Metallic Image Guide (SIMIG) Structure will be produced. In contrast to the guiding mechanism in dielectric waveguides, these conductive vias serve to efficiently maintain the guided wave's trajectory, preventing any leakage into the perforated region. This results in outstanding performance. The field distribution of the  $E_{11}^y$  mode of the SIMIG waveguide along the guiding channel and at the cross-section is presented in Fig. 4.5.

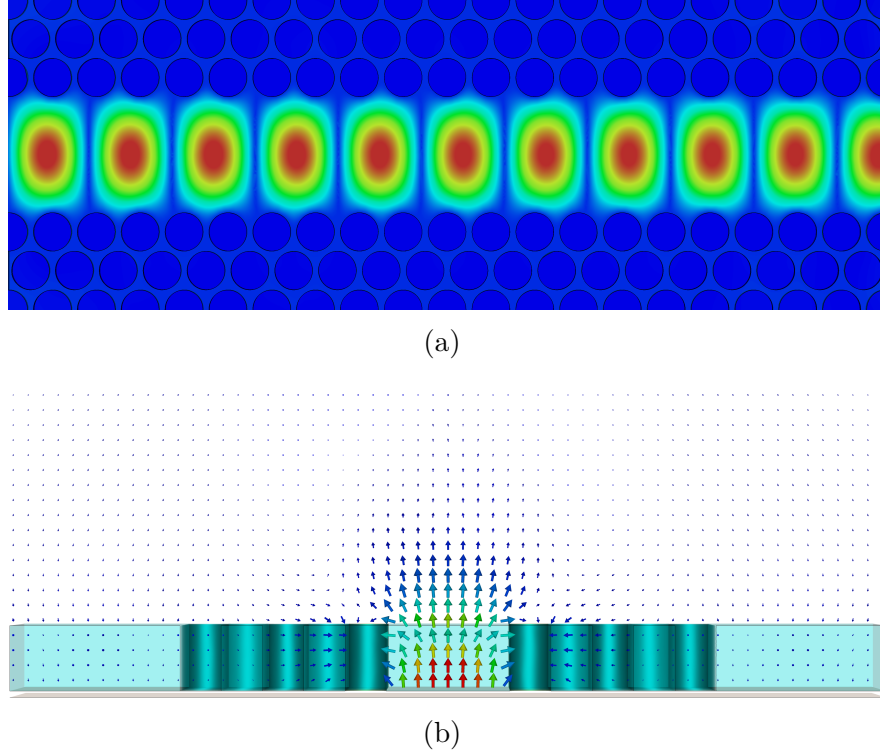


Figure 4.5 Field distribution of the  $E_{11}^y$  mode of the SIMIG structure at the frequency of 190 GHz, (a) magnitude of the electric field along the guiding channel and (b) electric field distribution on the cross-section.

As depicted in Fig. 4.1b, much like the SIIG waveguide, the SIMIG structure features various design parameters that can be independently adjusted. While these parameters offer substantial flexibility for the SIMIG structure, they simultaneously introduce a level of complexity similar to that of the SIIG waveguide. In addition to the shared structural parameters with the SIIG structure, such as  $w_c$ ,  $d$ , and others, the SIMIG introduces an additional design parameter: the material of the filled vias. It is paramount to underscore that the selection of these design parameters must be undertaken with meticulous consideration to

optimize bandwidth, minimize attenuation, and alleviate substrate leakage within the SIMIG section.

While it is feasible to create an analytical model for the investigated SIMIG structure by substituting the air perforation with metallic material and applying a similar procedure as used for SIIG modal development, the utilization of commercial EM simulation software, namely CST Studio Suite 2022, for extracting the initial set of propagating modes in the SIMIG structure offers greater convenience. The previously mentioned SIIG structure was utilized to create an SIMIG structure. In this process, the perforation rows were considered to be filled with a conductive material having an electric conductivity equal to  $\sigma_m = 2 \times 10^5 \text{ S/m}$ , relative permeability equal to  $\mu_m = 1$ , and relative permittivity equal to  $\varepsilon_m = 1$ . The investigated structure was designed in CST software, and the frequency domain solver was used to extract a subset of its initial propagating modes. The phase constant( $\beta$ ) and wave impedance of different propagating modes within the SIMIG structure mentioned above are extracted and shown in Fig. 4.6 and 4.7, respectively.

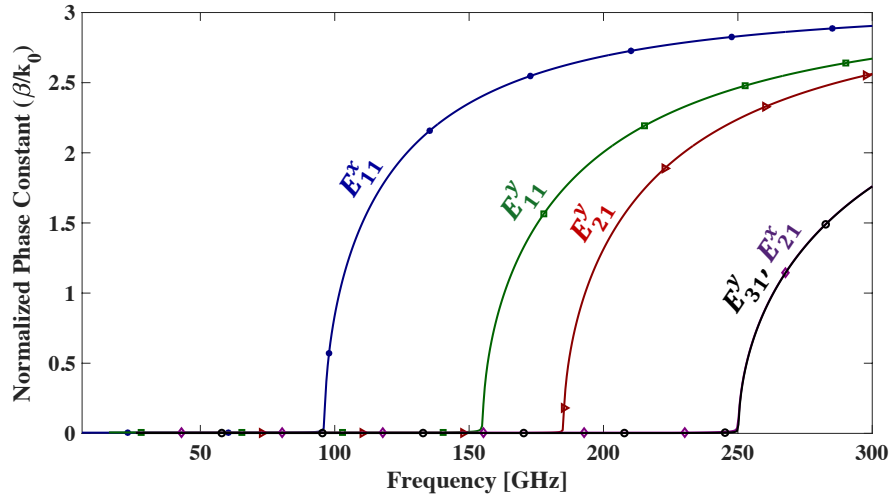


Figure 4.6 Extracted normalized phase constant of a few first modes of mentioned SIMIG structures.

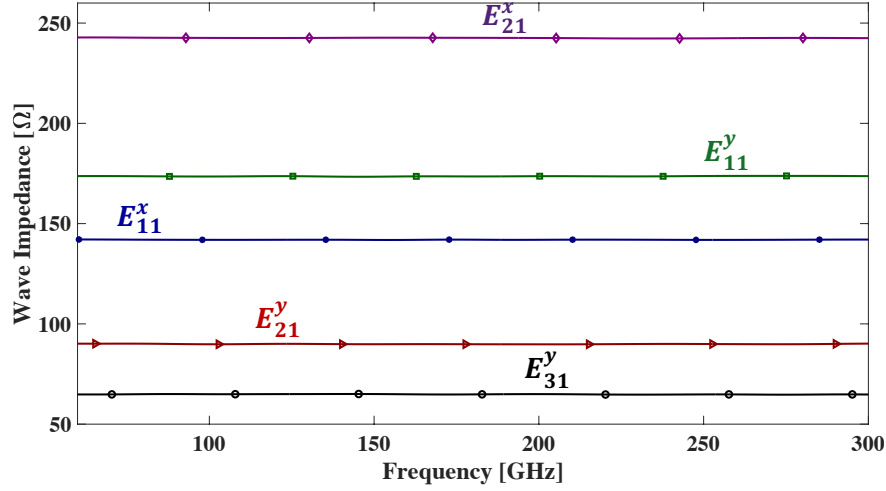


Figure 4.7 Wave impedance of a few first modes of mentioned SIMIG structures.

### 4.2.3 Substrate-Integrated Hybrid Dielectric-Metallic Image Guide

We prioritize SIIG technology as the primary technology for developing our substrate-integrated circuit. Consequently, we carefully select structural parameters to optimize the performance of the SIIG sections. To achieve a seamless transition, the SIMIG structure should accurately replicate the field distribution of the SIIG section. A thorough examination of the obtained results indicates that the fundamental mode propagating in the SIIG structure is the  $E_{11}^y$  mode, which exhibits a similar distribution to the  $E_{11}^y$  mode in SIMIG. This resemblance provides an opportunity to seamlessly connect the SIIG and SIMIG, thereby creating a Substrate-Integrated Hybrid Dielectric-Metallic Image Guide (SIHDMIG) structure.

Upon examining the results displayed in Figs. 4.3, and 4.6, it becomes apparent that a disparity exists in the cut-off frequencies of the  $E_{11}^y$  modes between the SIIG and SIMIG structures. To ensure the widest possible bandwidth and prevent mode convergence, it is imperative to conduct a thorough modal analysis on both the SIIG and SIMIG sections after matching their field distributions. This analysis is essential for implementing effective mode matching. To facilitate a smooth transition and simplify the fabrication process, it's crucial to use the same substrate and ground plane for both the SIIG and SIMIG sections. Furthermore, the perforation size and periodicity should be determined based on fabrication limitations [84]. Considering the preceding discussion, the width of the guiding channel (i.e.,  $w_c$ ) stands out as the primary design parameter that can be adjusted to achieve the most effective transition.

To find the optimal width for the guiding channel in the SIMIG section, one that can yield the smoothest transition and the broadest achievable operating range, the same SIMIG structure as in the previous example was employed. The width of the guiding channel (i.e.,  $w_c$ ) was considered to vary from  $400\ \mu\text{m}$  to  $560\ \mu\text{m}$ , and the resulting phase constants of the fundamental mode and the second mode are illustrated in Figs. 4.8 and 4.9, respectively. As evident in these figures, the change of the guiding channel's width exhibits no discernible impact on the cut-off frequency of the fundamental mode. However, it does exhibit a notable impact on the second mode, with a decrease in the width of the guiding channel resulting in an increment of the cut-off frequency for the second modes. After a thorough analysis of the results obtained from the simulated SIIG and SIMIG structures, it was determined that the width of the guiding channel in the SIMIG section should be set at  $w_c = 510\ \mu\text{m}$ .

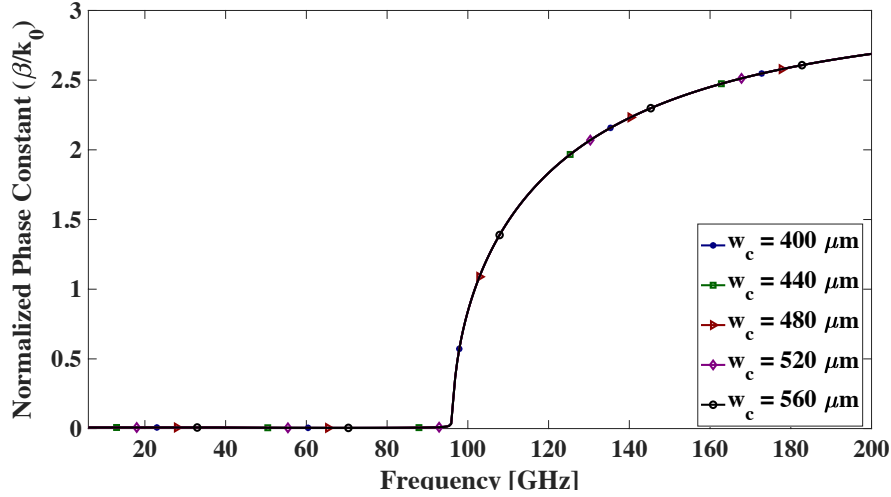


Figure 4.8 Extracted normalized phase constant of the fundamental mode of mentioned SIMIG structure.

To offer a more thorough insight into these transitions, we interconnected a SIIG waveguide with an SIMIG waveguide. The width of the guiding channel gradually expanded from  $480\ \mu\text{m}$  in the SIIG section to  $510\ \mu\text{m}$  in the SIMIG section. The transition performance was evaluated in terms of return loss and field distribution, as depicted in Figs. 4.10 and 4.11, respectively. These figures clearly illustrate a seamless transformation of the propagated field from the SIIG section to the SIMIG section, with no notable reflections at the interface. A comparison of the insertion loss and return loss of this combined structure with the original SIIG waveguide [92] further underscores the absence of significant reflections at the interface.

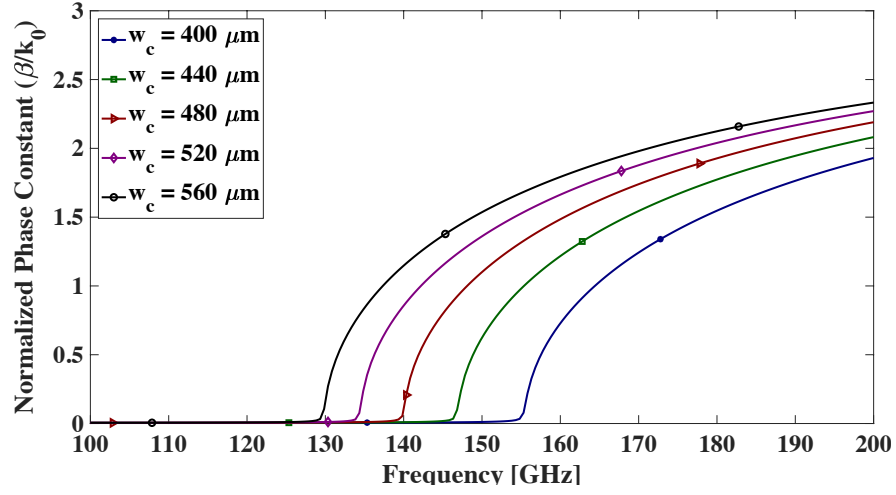


Figure 4.9 Extracted normalized phase constant of the second mode of mentioned SIMIG structure.

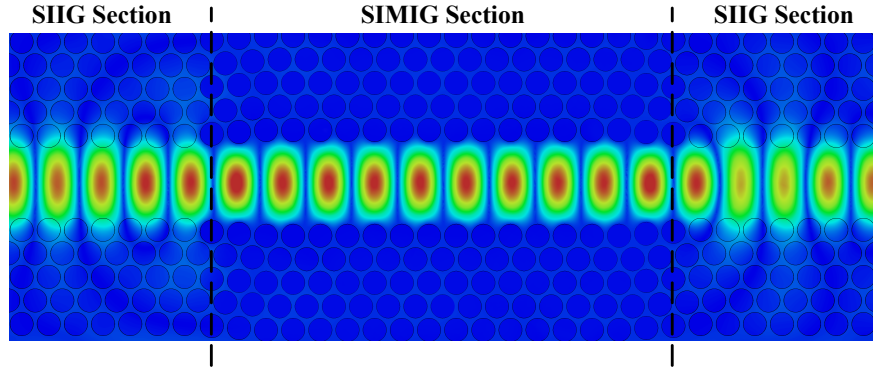


Figure 4.10 Field distribution of mentioned SIIG/SIMIG transition at the frequency of 200 GHz.

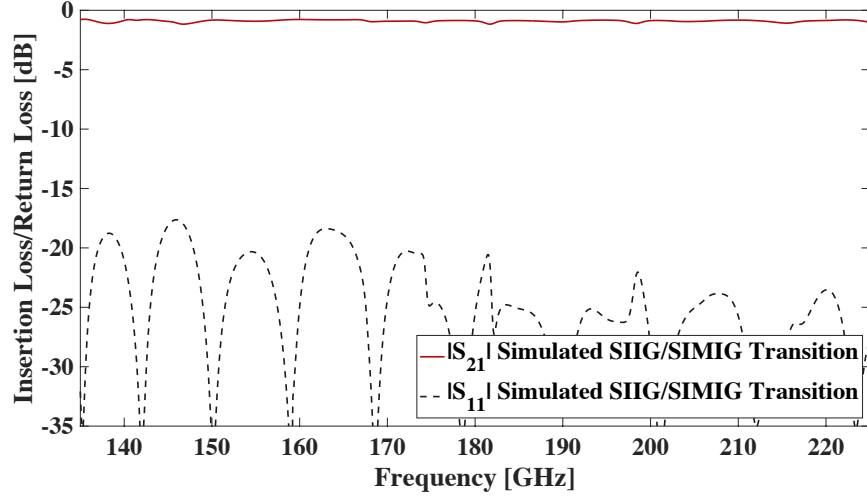


Figure 4.11 Extracted S-parameter of mentioned SIIG/SIMIG transition.

### 4.3 Substrate-Integrated Hybrid Dielectric-Metallic Image Guide Performance at Sharp Bends

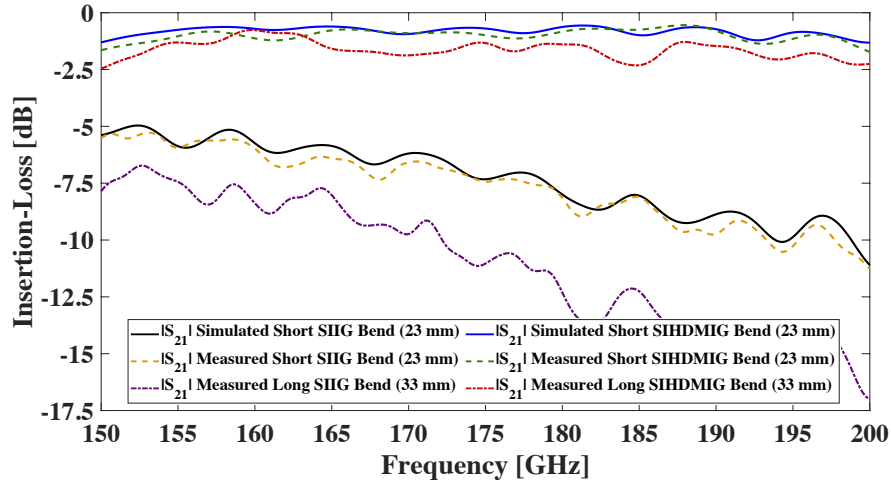
While the SIMIG exhibits commendable performance, it is associated with higher conductor losses compared to the SIIG structure. To keep the overall attenuation of the guiding structure within an acceptable range, a hybrid approach is suggested. This approach involves the integration of the SIIG waveguide with the SIMIG waveguide. In this combination, the use of metallic vias is primarily limited to sharp bends, effectively reducing conductor losses within the resulting structure. Following an examination of the feasibility of achieving a smooth transition from the SIIG waveguide to the SIMIG waveguide, this configuration can now be applied to sharp bends.

According to the above discussion and based on the material available at the *Poly-Grames Research Center*, an alumina ( $\epsilon_r = 9.4$  and  $\tan \delta = 6 \times 10^{-3}$ ) substrate with a thickness of  $d = 254 \mu m$  is utilized to create two SIIG structures featuring a 60-degree bend along its transmission direction. The circular perforation and the regular triangular pattern are chosen as the most efficient pattern to achieve the highest possible substrate removal. For the first prototype, the operating frequency range of the proposed SIIG waveguide is considered to be in the WR-5.1 band (i.e., 135 to 225 GHz). To have the Bragg electromagnetic bandgap accrued far away from the operating region, the perforation periodicity is considered to be equal to  $a = 185 \mu m$ , which leads the lowest EBG to have a central frequency of 380 GHz. Larger perforations provide a higher permittivity contrast between the perforated regions and the guiding channel, which leads to higher power transmission. However, due to the fabrication limitation, a minimum  $25.4 \mu m$  wall should be kept between adjacent perforations



to ensure the mechanical stability of the fabricated structure. The proposed SIIG structure is considered to have a guiding channel width of  $w_c = 480 \mu m$ . Although the hybrid structure is a planar waveguide, the structure is fed with a WR-5.1 rectangular waveguide. To achieve an efficient transition between these two waveguides, it is essential to design a well-optimized interface that seamlessly connects the SIIG structure and the rectangular waveguide. To minimize return loss, a smoothly tapered dielectric section can be employed. The taper can be considered as a special case of stepped transformers, where the number of steps is infinite, and their individual reflections are infinitesimally small. The design objective is to achieve the widest possible bandwidth with the shortest possible tapers. Accordingly, the SIIG waveguide is tapered with a length of 3.53 mm at both ends.

It is worth mentioning that most parts of the losses in the designed prototype are due to the feeding mismatch. To remove this loss and accurately measure the transmission loss, the dual-line technique is used [4]. Two SIIG structures differing in length (i.e., 23.3mm and 12.21mm) are designed and fabricated, and the propagation constant is extracted subsequently from the pair of measured S-parameters. The mentioned SIIG waveguide was fabricated and tested at the *Poly-Grames Research Center* and the extracted S-parameters are shown in Fig. 4.12. To provide a better insight about the SIIG performance, the simulated field distribution is shown in Fig. 4.13. Since the measurement equipment (i.e., WR-5.1 waveguide and measurement extender) has a recommended operating frequency band of 135 GHz to 225 GHz, the frequency range plotted in Fig. 4.12 is thus limited.



(a)

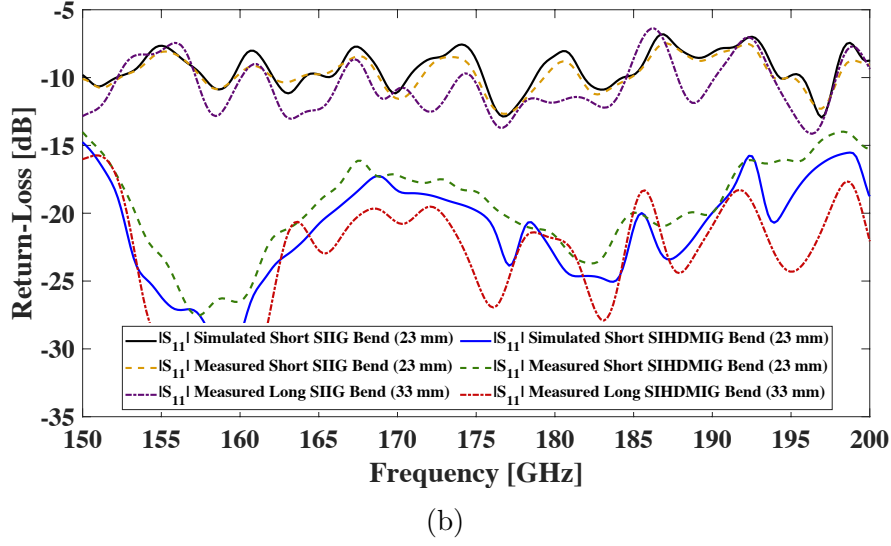


Figure 4.12 Extracted performance of the different technologies at a 60-degree bend. (a) insertion loss and (b) return loss .

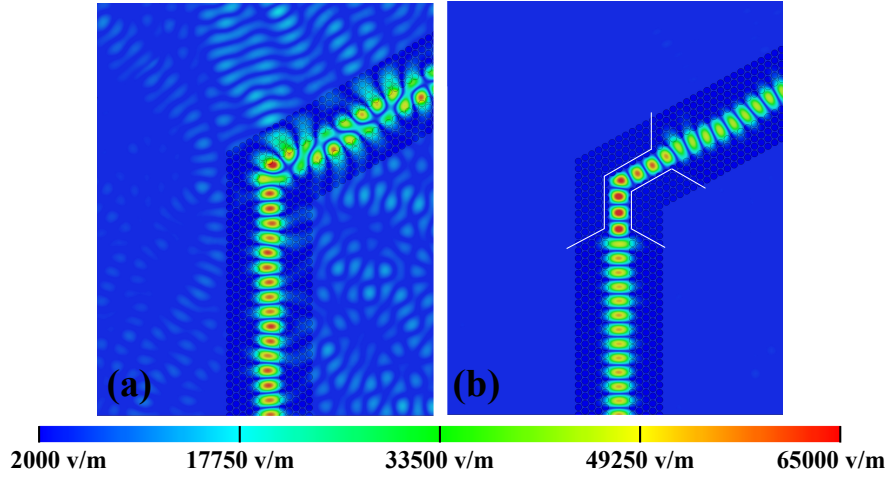


Figure 4.13 Field distribution of different technology at a 60-degree bend at the frequency of 180 GHz, a) SIIG waveguide, b) proposed SIHDMIG waveguide along with tapering opening.

As depicted in Fig. 4.14, the same SIIG structure was employed to construct a hybrid dielectric-metallic image guide structure, incorporating an identical 60-degree bend along its transmission direction. To ensure a seamless transition, the guiding channel smoothly tapers from  $480 \mu\text{m}$  in the SIIG section to  $510 \mu\text{m}$  in the SIMIG section. As shown in Fig. 4.15, the mentioned SIIG waveguide was fabricated and tested at the *Poly-Grames Research Center*. The field distribution and measured S-parameters of the designed SIHDMIG structure are illustrated in Figs. 4.12 and 4.13, respectively.

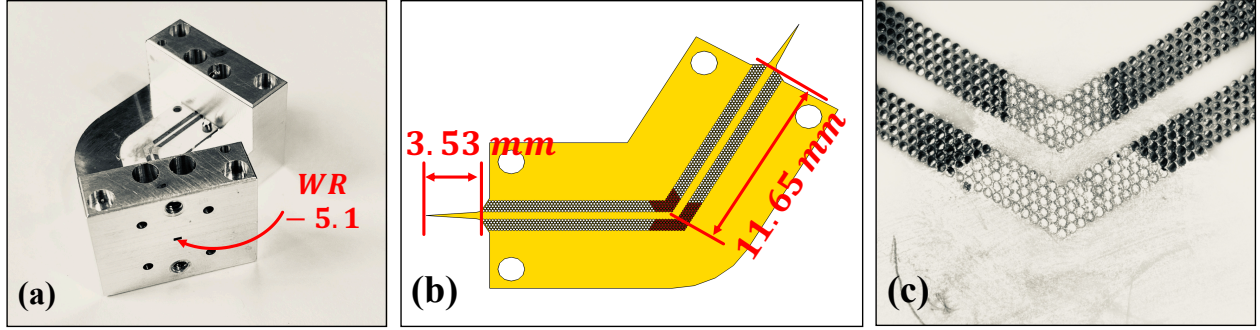


Figure 4.14 a) The fabricated hybrid waveguide featuring a 60 degree bend fed by WR-5.1 waveguide, b) the fabricated alumina substrate having 5 rows of circular perforations, c) zoomed view of the guiding channel and adjacent perforated regions.

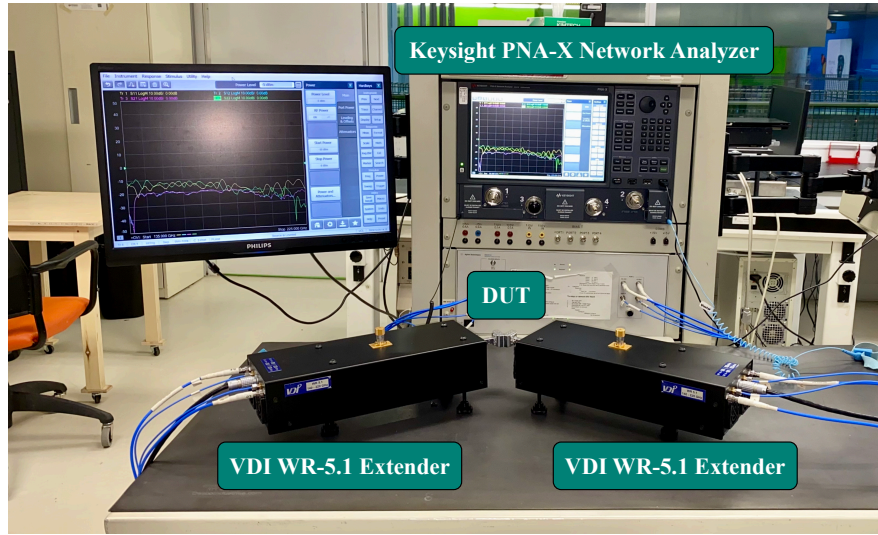


Figure 4.15 Measurement setup used to extract the S-parameters of the SIHDMIG waveguide in WR-5.1 Band.

As depicted in Fig. 4.12a, the SIIG structure exhibits a substantial average insertion loss of 3.478 dB/cm when subjected to a 60-degree bend within the WR-5.1 frequency band, indicating poor performance. However, the integration of the SIMIG structure at this bend enhances the SIHDMIG waveguide's performance, achieving an average insertion loss of 0.834 dB/cm, which is considered highly favorable. Notably, when comparing the insertion loss of the straight SIIG waveguide ( $IL = 0.578$  dB/cm) with that of the proposed SIHDMIG waveguide ( $IL = 0.834$  dB/cm), the difference is primarily attributed to conductor losses within the SIMIG section and minor reflection/leakage at sharp bends.

As depicted in Fig. 4.13, the underperformance of the SIIG structure at sharp bends is attributed to significant leakage into the perforated regions. In contrast, the metallic vias

in the SIMIG section effectively confine the guided wave, preventing it from leaking into the perforated region and maintaining it on the intended path. Consequently, the SIMIG section demonstrates superior performance. To further enhance the architecture's performance, the metallic vias' patterns at the beginning and end were designed to create a horn-like guiding shape, facilitating improved guidance and direction of the guided wave into the SIMIG section. It is important to note that a closer examination of the extracted insertion loss reveals a reduction in the operating bandwidth of the proposed hybrid waveguide. The original straight SIIG structure had an operating bandwidth spanning from 135 GHz to 225 GHz, whereas the proposed hybrid waveguide's operating bandwidth now ranges from 140 GHz to 200 GHz.

To assess the applicability of the proposed waveguide in THz applications, as shown in Fig. 4.16, we designed and fabricated an additional set of prototypes for both the SIIG waveguide and the proposed hybrid waveguide on an alumina substrate, with the ground plane constructed from aluminum. These structures featured identical 60-degree bends in their transmission direction, tailored for the WR-3.5 frequency band. The periodicity of the perforations was consistently set at  $a = 150 \mu m$ , and the perforation size remained constant at  $b = 124.6 \mu m$ . In this design, the SIIG section possessed a guiding channel with a width of  $w_c = 330 \mu m$ , which gracefully expanded to  $w_c = 370 \mu m$  in the SIMIG section. Measured S-parameters is depicted in Fig. 4.17, while Fig. 4.18 displays the simulated field distribution of the designed SIIG and SIHDMIG structures. A comparative analysis of the results demonstrates that the guided wave is efficiently contained and directed along the guiding channel and at the sharp bend, with no observable leakage into the substrate. Notably, when comparing insertion losses, it is evident that the proposed hybrid waveguide has achieved a notable 2.8 dB/cm improvement in insertion loss. However, the operating bandwidth has been reduced to a range of 215 GHz to 275 GHz.

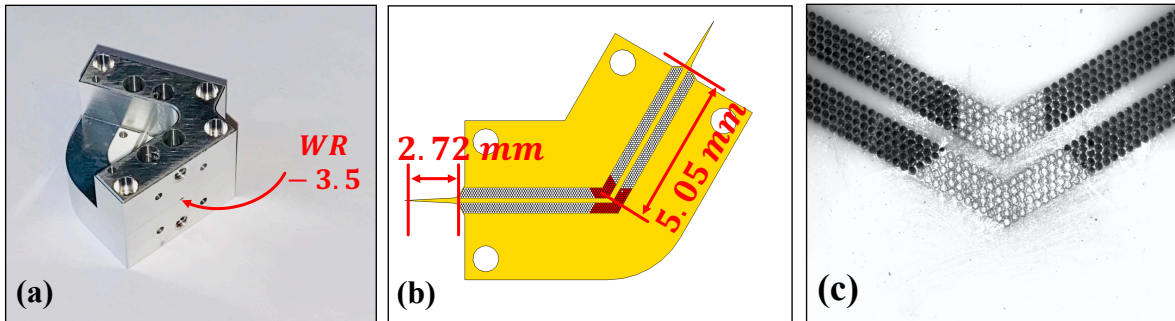
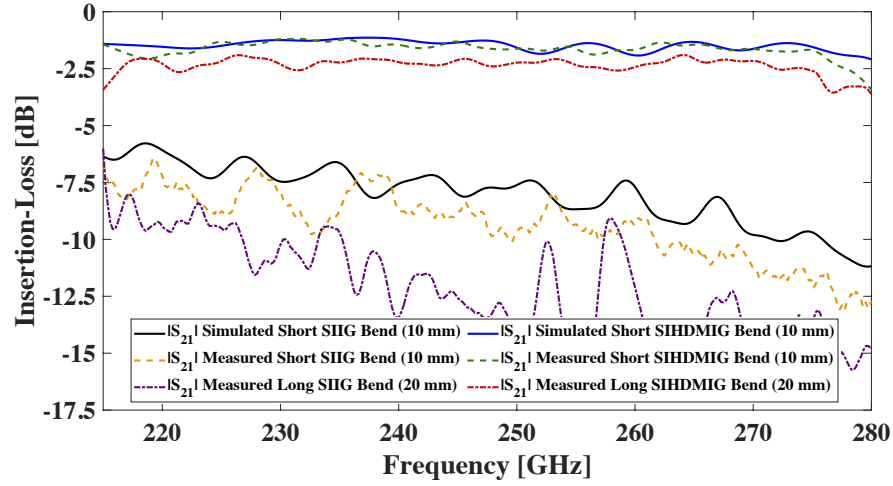
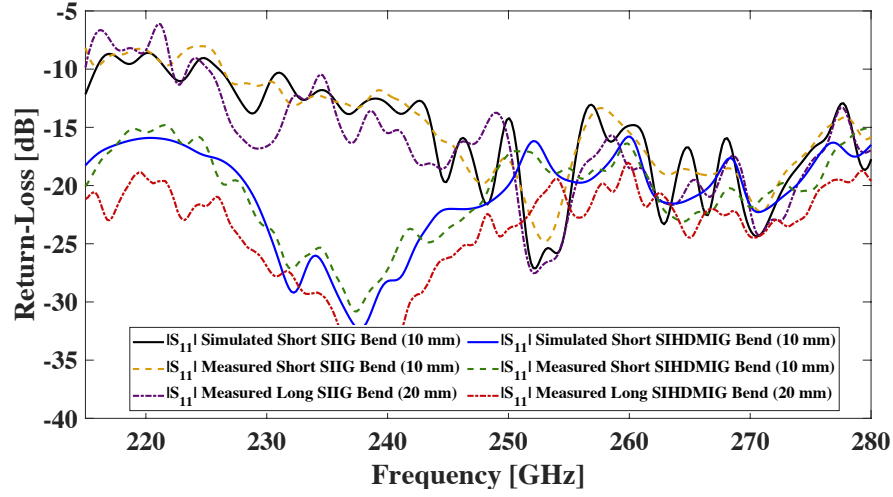


Figure 4.16 a) The fabricated hybrid waveguide featuring a 60 degree bend fed by WR-3.5 waveguide, b) the fabricated alumina substrate having 5 rows of circular perforations, c) zoomed view of the guiding channel and adjacent perforated regions.



(a)



(b)

Figure 4.17 Extracted performance of the different technologies at a 60-degree bend. (a) insertion loss and (b) return loss .



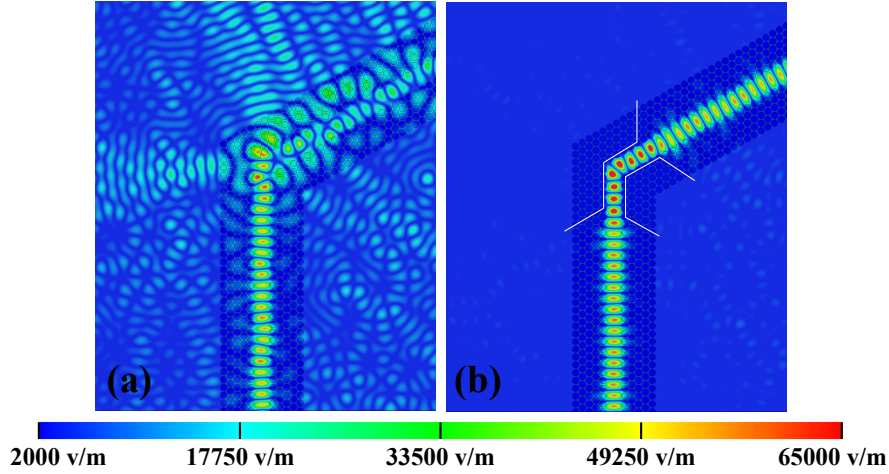


Figure 4.18 Field distribution of different technology at a 60-degree bend at the frequency of 180 GHz, a) SIIG waveguide, b) proposed SIHDMIG waveguide along with tapering opening.

#### 4.4 Developing Compact Power/Divider for SIIG Technology

A compact power divider/combiner is instrumental in advancing highly integrated THz systems. Within the terahertz technology field, the primary objective is achieving compactness and seamless integration to effectively address the increasing demands of emerging applications. The power divider/combiner assumes a pivotal role in these systems, streamlining the efficient management and distribution of high-frequency signals. By reducing the footprint of this essential component, it becomes possible to design and deploy compact THz systems that are both space-efficient and deliver enhanced performance. These capabilities align seamlessly with the intricate demands of advanced applications across diverse sectors.

Principally, sub-THz/THz technologies often present challenges in achieving satisfactory performance at sharp discontinuities, such as sharp bends. Their effectiveness tends to be more pronounced when navigating extended, gradual curved bends. Nevertheless, these extended curved bends impose limitations on their utility within highly compact system development endeavors. As demonstrated in the preceding section, the examined substrate-integrated hybrid metallic-dielectric image guide structure excels in its performance at sharp bends. This exceptional performance has spurred the utilization of this hybrid architecture for the creation of a significantly compact power divider/combiner for the SIIG technology within the context of substrate-integrated circuits (SICs).

Consequently, as shown in Fig. 4.19, an alumina substrate with material properties  $\epsilon_r = 9.4$  and  $\tan \delta = 6 \times 10^{-3}$ , and possessing a thickness of  $d = 254 \mu m$ , has been chosen for the design of the power divider/combiner prototype. In order to optimize the removal of

substrate material, a circular perforation design along with a regular triangular pattern has been selected as the most effective configuration. The perforation periodicity chosen is  $a = 185 \mu m$ , which leads to the electromagnetic band gap (EBG) centering around 380 GHz. The SIIG section is designed with a guiding channel width of  $w_c = 480 \mu m$ , while the SIMIG section features a guiding channel width of  $w_c = 510 \mu m$ . Just as in our previous fabrication process, this prototype is intended to be fed with a WR-5.1 rectangular waveguide. The total length of the guiding channel in the designed power divider/combiner considered to be equal to 21.46mm. Its performance, encompassing factors such as insertion loss and return loss, is visually represented in Fig. 4.20.

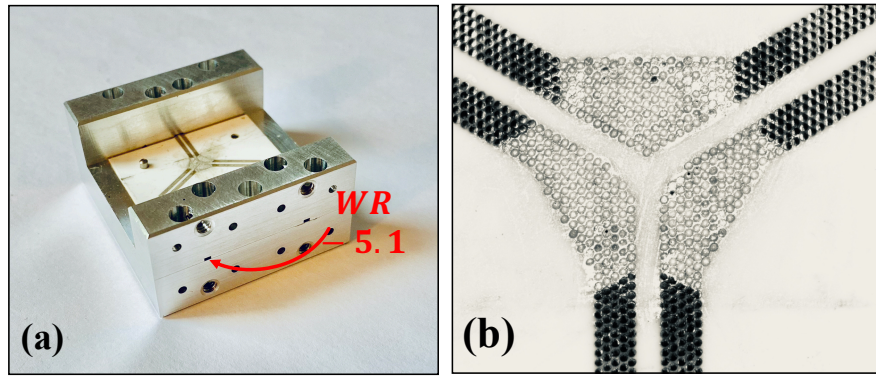


Figure 4.19 a) The fabricated power divider/combiner fed by WR-5.1 waveguide, b) zoomed view of the guiding channel and adjacent perforated regions.

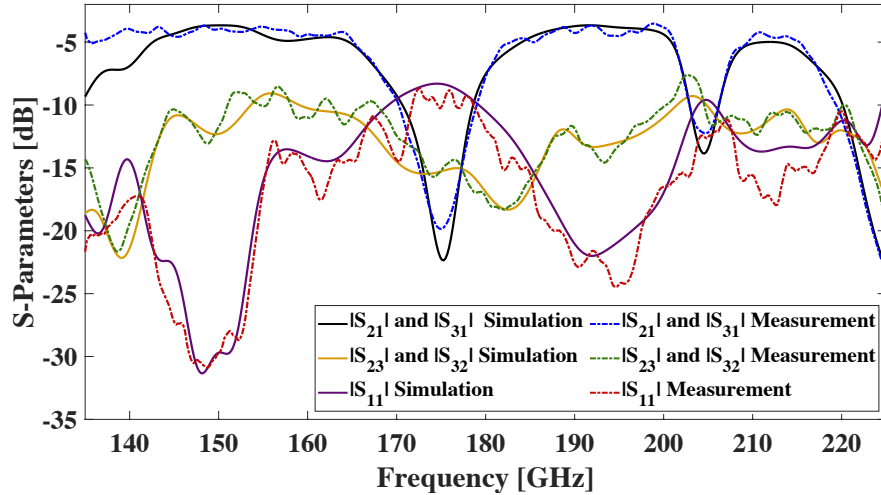


Figure 4.20 Extracted performance of the designed power divider/combiner in term of insertion/return loss.

From Fig. 4.20, it is evident that the operating bandwidth of the power divider/combiner design has been narrowed down to two distinct segments: one spanning from 135 GHz to 165 GHz and the other from 185 GHz to 200 GHz. Input signals originating from Port 1 are evenly distributed to both Port 2 and Port 3. Taking into account the inherent insertion loss of the hybrid structure and the splitting ratio, the output signals at Ports 2 and 3 exhibit practically identical amplitudes, affirming the suitability of the designed power divider.

Figure 4.21 displays the field distribution of the designed divider at various frequencies. A comparative analysis of the field distribution and the extracted S-parameters reveals that at a frequency of 150 GHz, the divider excels in efficiently splitting the input signal. Conversely, at 175 GHz, nearly no signals traverse the divider, with the majority of the signal being reflected to the input port. Furthermore, at 190 GHz, the power divider adeptly partitions the input signals.

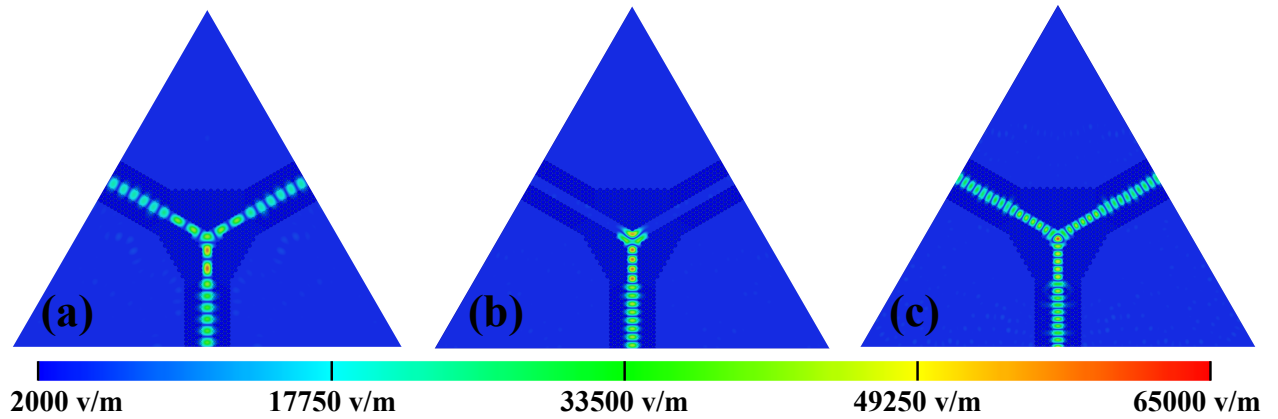


Figure 4.21 Field distribution of the designed power divider/combiner at, a) 150 GHz , b) 175 GHz, and c) 190 GHz.

To demonstrate the applicability of the proposed hybrid waveguide in the THz regime, as shown in Fig. 4.22, we utilized the same alumina substrate and aluminum ground plane to design two compact power divider/combiners within the WR-3.5 frequency band. The chosen perforation periodicity was set at  $a = 150 \mu m$ , with a guiding channel width of  $w_c = 330 \mu m$  for one structure, while the SIMIG section featured a guiding channel width of  $w_c = 370 \mu m$ . Similar to our previous design process, this prototype is intended to be fed with a WR-3.5 rectangular waveguide. The total length of the guiding channel in the designed power divider/combiner considered to be equal to 19.71mm. Its performance, encompassing factors such as insertion loss and return loss, is visually represented in Fig. 4.23.



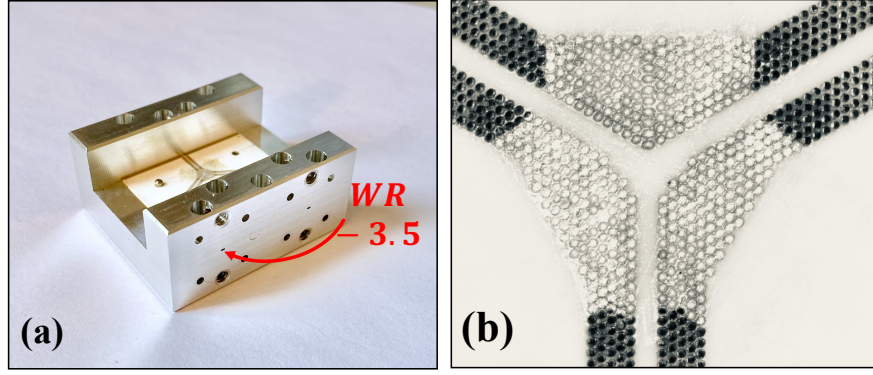


Figure 4.22 a) The fabricated power divider/combiner fed by WR-3.5 waveguide, b) zoomed view of the guiding channel and adjacent perforated regions.

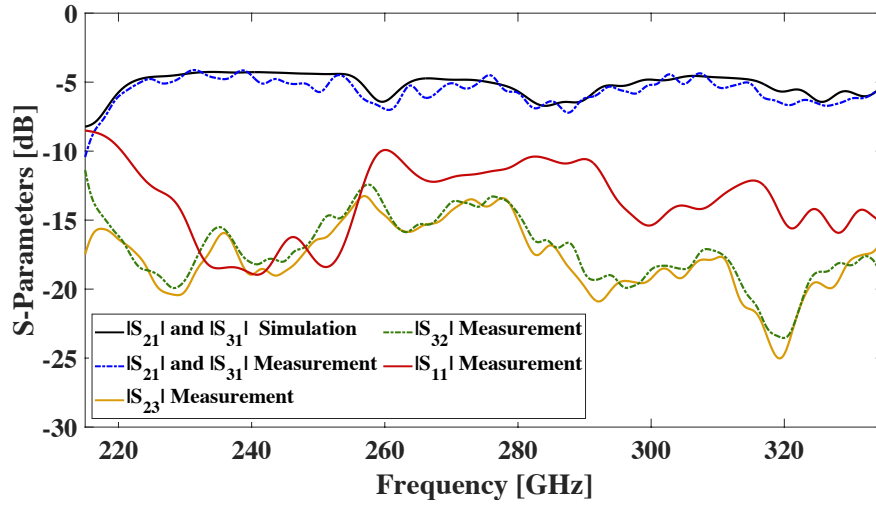


Figure 4.23 Extracted performance of the designed power divider/combiner in term of insertion/return loss.

As shown in Fig. 4.23, the operating bandwidth of the power divider/combiner design has been constrained to two distinct segments: one ranging from 225 GHz to 250 GHz and the other from 295 GHz to 315 GHz. Input signals originating from Port 1 are evenly distributed to both Port 2 and Port 3. Considering the inherent insertion loss of the hybrid structure and the splitting ratio, the output signals at Ports 2 and 3 exhibit nearly identical amplitudes, confirming the effectiveness of the designed power divider.

Figure 4.24 illustrates the field distribution of the designed divider at different frequencies. A comparative examination of the field distribution and the extracted S-parameters indicates that at a frequency of 235 GHz, the divider excels at efficiently splitting the input signal. Conversely, at 260 GHz, minimal signal transmission occurs through the divider, with the

majority of the signal being reflected back to the input port. Moreover, at 310 GHz, the power divider adeptly partitions the input signals.

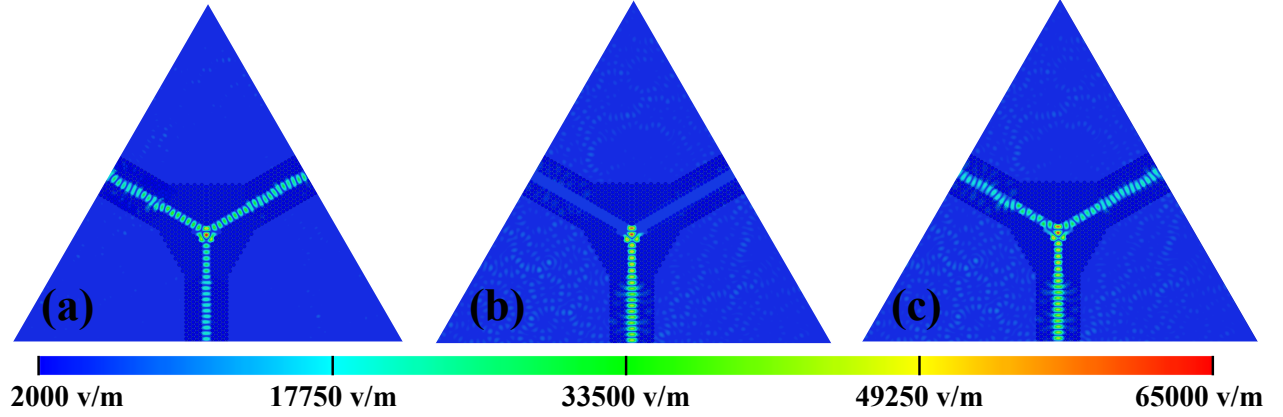


Figure 4.24 Field distribution of the designed power divider/combiner at, a) 235 GHz , b) 260 GHz, and c) 310 GHz.

#### 4.5 Conclusion

While the substrate-integrated image guide (SIIG) waveguide demonstrates outstanding performance in straight-line configurations, it encounters challenges related to leakage at sharp bends. These limitations can restrict the practical applications of SIIG technologies, particularly in scenarios demanding sharp discontinuities, such as compact power dividers/combiners. In this paper, we introduce a novel waveguide, the Substrate-Integrated Metallic Guide (SIMIG), which, when combined with SIIG, enables the creation of a hybrid waveguide known as the Substrate-Integrated Hybrid Dielectric-Metallic Image Guide (SIHDMIG) technology. SIHDMIG effectively mitigates wave leakage into the substrate and exhibits exceptional performance at sharp bends. The experimental results reveal that the proposed SIHDMIG structure enhances SIIG performance at sharp bends by 3 dB. Subsequently, we leverage this innovative technology to design a highly compact power divider/combiner. Based on the obtained results, the designed power divider/combiner demonstrates good performance across various frequency bands within the WR-5.1 frequency range.

## CHAPTER 5 CONCLUSION AND RECOMMENDATION

### 5.1 Conclusion

In the course of this doctoral thesis, we have delved into three distinct projects, each contributing significantly to the advancement of high-frequency technology, with a particular focus on the demanding sub-THz/THz regime. These projects collectively have deepened our comprehension of dielectric waveguides, Substrate-Integrated Image Guide (SIIG) structures, and the challenges they confront in practical applications.

In the first project, we introduced a novel analytical model for accurately analyzing dielectric waveguides in the sub-THz/THz spectrum. Recognizing the importance of dielectric losses, we departed from existing analytical methods that considered the substrate as a lossless pure dielectric. Our innovative approach encompassed a comprehensive consideration of dielectric losses in the substrate, treating the perforations as a periodic structure. We applied the *Floquet theory* and *Fourier series expansion* to develop an eigenequation that accurately modeled the effective permittivity of the structure. This modification allowed us to account for dielectric losses in our analysis and greatly enhanced the accuracy of the obtained results.

Moreover, we extended our analysis to include conductor losses, a crucial consideration in the sub-THz/THz regime. This led to the development of a modified modal analysis that could accurately extract the propagation constants of propagating modes within dielectric waveguides. Our method's accuracy and efficiency were demonstrated through rigorous comparisons with commercial electromagnetic simulation software and validated through experimental testing of a fabricated SIIG waveguide prototype. This project has contributed a valuable analytical tool for the precise modeling of dielectric waveguides in high-frequency applications.

In the second project, we applied the analytical model developed in the first project to study the effects of structural parameters on SIIG waveguide performance. Recognizing that the SIIG waveguide, with its low-loss wave transmission, planar structure, and shared ground plane, held tremendous potential for sub-THz/THz applications, we sought to optimize its design. By choosing the most suitable structural parameters, we designed, fabricated, and tested two prototypes for the WR-5.1 and WR-3.5 frequency bands.

The results of these experiments were highly promising. The first prototype exhibited a mean insertion loss of 0.578 dB/cm over a frequency range of 135 GHz to 225 GHz, demonstrating the SIIG waveguide's suitability for high-frequency applications. The second prototype

achieved an average insertion loss of  $IL = 1.431 \text{ dB/cm}$  in the frequency range of 215 GHz to 335 GHz, further affirming the potential of SIIG waveguides for sub-THz/THz applications. This project showcased the practicality of optimized SIIG waveguide designs and their significance in future high-frequency technology.

In our third and final project, we addressed a significant challenge faced by SIIG waveguides - leakage at sharp bends. We introduced an innovative solution through the integration of a hybrid waveguide that incorporated Substrate-Integrated Metallic Image Guide (SIMIG) into the SIIG structure. This innovation effectively prevented guided wave leakage and enhanced SIIG's performance at sharp bends. This breakthrough not only addressed a longstanding issue but also enabled the development of highly compact power divider/combiner devices using SIIG technology.

To accomplish this, we conducted a comprehensive investigation to achieve field, impedance and mode matching between the SIIG and SIMIG sections. Additionally, a detailed study of structural parameters led to the selection of optimal values for the width of the guiding channels in both sections. Subsequently, we designed and simulated two power divider structures for the WR-5.1 and WR-3.5 frequency bands, followed by successful prototype fabrication. The measured performance of these prototypes closely aligned with our simulation results, validating the effectiveness of our innovative approach.

## 5.2 Recommendation

In my quest to harness the full potential of SIIG technology for developing Substrate-integrated circuits (SICs), I strongly recommend that fellow researchers explore the development of other essential circuit components using this technology, such as couplers and filters. Given that SIIG technology inherently employs perforations to form the guiding channel, these perforations can serve as discontinuities suitable for developing filters tailored for the sub-THz/THz regime. The open structure of the investigated SIIG waveguide provides an ideal platform for designing efficient feeding mechanisms for dielectric antennas and even the creation of leaky-wave antennas.

To further enhance the practicality and versatility of the investigated technology, I highly encourage other researchers to work on developing efficient transitions to existing technologies in the sub-THz/THz regime, including Substrate-Integrated Nonradiative Dielectric (SINRD), gap waveguide, rectangular waveguides, and pure dielectric waveguides. The ease of integration will facilitate the utilization of this technology alongside other established technologies, thereby increasing its applicability and expanding its utility in the field. This collaborative

effort holds the potential to revolutionize the way we approach high-frequency technology and its myriad applications.

## REFERENCES

- [1] C. Corsi and F. Sizov, *THz and security applications: detectors, sources and associated electronics for THz applications*. Springer, 2014.
- [2] (2022, Feb). [Online]. Available: <https://www.microwavejournal.com/blogs/1-rog-blog/post/36467-concerning-pcbs-and-the-transition-from-microwaves-to-millimeter-waves>
- [3] G. S. Wiederhecker, P. Dainese, and T. P. Mayer Alegre, “Brillouin optomechanics in nanophotonic structures,” *APL Photonics*, vol. 4, no. 7, 2019.
- [4] A. Patrovsky and K. Wu, “Substrate integrated image guide (siig)-a planar dielectric waveguide technology for millimeter-wave applications,” *IEEE transactions on Microwave Theory and Techniques*, vol. 54, no. 6, pp. 2872–2879, 2006.
- [5] T. C. Edwards and M. B. Steer, *Foundations for microstrip circuit design*. John Wiley & Sons, 2016.
- [6] R. N. Simons, *Coplanar waveguide circuits, components, and systems*. John Wiley & Sons, 2004.
- [7] B. Bhat and S. K. Koul, *Stripline-like transmission lines for microwave integrated circuits*. New Age International, 1989.
- [8] F. Xu and K. Wu, “Guided-wave and leakage characteristics of substrate integrated waveguide,” *IEEE Transactions on microwave theory and techniques*, vol. 53, no. 1, pp. 66–73, 2005.
- [9] S. Koenig, D. Lopez-Diaz, J. Antes, F. Boes, R. Henneberger, A. Leuther, A. Tessmann, R. Schmogrow, D. Hillerkuss, R. Palmer *et al.*, “Wireless sub-thz communication system with high data rate,” *Nature photonics*, vol. 7, no. 12, pp. 977–981, 2013.
- [10] D. Hondros and P. Debye, “Elektromagnetische wellen an dielektrischen drähten,” *Annalen der Physik*, vol. 337, no. 8, pp. 465–476, 1910.
- [11] G. Southworth, “Hyper-frequency wave guides—general considerations and experimental results,” *Bell System Technical Journal*, vol. 15, no. 2, pp. 284–309, 1936.
- [12] J. R. Carson, S. P. Mead, and S. Schelkunoff, “Hyper-frequency wave guides—mathematical theory,” *Bell System Technical Journal*, vol. 15, no. 2, pp. 310–333, 1936.

- [13] G. Saffold, "Theory and application of dielectric rod antennas and arrays," Ph.D. dissertation, University of South Florida, 2021.
- [14] C. Chandler, "An investigation of dielectric rod as wave guide," *Journal of Applied Physics*, vol. 20, no. 12, pp. 1188–1192, 1949.
- [15] W. M. Elsasser, "Attenuation in a dielectric circular rod," *Journal of Applied Physics*, vol. 20, no. 12, pp. 1193–1196, 1949.
- [16] N. Kapany, *Optical waveguides*. Elsevier, 2012.
- [17] D. King, "Dielectric image line," *Journal of Applied Physics*, vol. 23, no. 6, pp. 699–700, 1952.
- [18] R. Knox and P. Toullos, "Integrated circuits for the millimeter through optical frequency range," in *Proc. Symp. Submillimeter Waves*, vol. 20. Brooklyn, NY, 1970, pp. 497–515.
- [19] T. Itoh, "Inverted strip dielectric waveguide for millimeter-wave integrated circuits," *IEEE transactions on Microwave Theory and Techniques*, vol. 24, no. 11, pp. 821–827, 1976.
- [20] T. Yoneyama and S. Nishida, "Nonradiative dielectric waveguide for millimeter-wave integrated circuits," *IEEE transactions on Microwave Theory and Techniques*, vol. 29, no. 11, pp. 1188–1192, 1981.
- [21] T. Rozzi and S. Hedges, "Rigorous analysis and network modeling of the inset dielectric guide," *IEEE transactions on Microwave Theory and Techniques*, vol. 35, no. 9, pp. 823–834, 1987.
- [22] K. Wu, M. Bozzi, and N. J. Fonseca, "Substrate integrated transmission lines: Review and applications," *IEEE Journal of Microwaves*, vol. 1, no. 1, pp. 345–363, 2021.
- [23] R. M. Knox, "Dielectric waveguide microwave integrated circuits-an overview," *IEEE Transactions on Microwave Theory and Techniques*, vol. 24, no. 11, pp. 806–814, 1976.
- [24] Y. J. Cheng, Y. X. Guo, X. Y. Bao, and K. B. Ng, "Millimeter-wave low temperature co-fired ceramic leaky-wave antenna and array based on the substrate integrated image guide technology," *IEEE Transactions on Antennas and Propagation*, vol. 62, no. 2, pp. 669–676, 2013.
- [25] Y. Chang and L. Yuan, "Ic's for 94 ghz radar applications in dielectric image guide," *Microwave Journal*, vol. 24, p. 81, 1981.

- [26] K. Wu, "Integration and interconnect techniques of planar and non-planar structures for microwave and millimeter-wave circuits-current status and future trend," in *APMC 2001. 2001 Asia-Pacific Microwave Conference (Cat. No. 01TH8577)*, vol. 2. IEEE, 2001, pp. 411–416.
- [27] H. Sarieddeen, N. Saeed, T. Y. Al-Naffouri, and M.-S. Alouini, "Next generation terahertz communications: A rendezvous of sensing, imaging, and localization," *IEEE Communications Magazine*, vol. 58, no. 5, pp. 69–75, 2020.
- [28] N. Laman, S. S. Harsha, D. Grischkowsky, and J. S. Melinger, "High-resolution waveguide thz spectroscopy of biological molecules," *Biophysical journal*, vol. 94, no. 3, pp. 1010–1020, 2008.
- [29] H.-G. Von Ribbeck, M. Brehm, D. Van der Weide, S. Winnerl, O. Drachenko, M. Helm, and F. Keilmann, "Spectroscopic thz near-field microscope," *Optics Express*, vol. 16, no. 5, pp. 3430–3438, 2008.
- [30] K. Murano, I. Watanabe, A. Kasamatsu, S. Suzuki, M. Asada, W. Withayachumnankul, T. Tanaka, and Y. Monnai, "Low-profile terahertz radar based on broadband leaky-wave beam steering," *IEEE Transactions on Terahertz Science and Technology*, vol. 7, no. 1, pp. 60–69, 2016.
- [31] A. M. Eblabla, X. Li, D. J. Wallis, I. Guiney, and K. Elgaid, "Gan on low-resistivity silicon thz high-q passive device technology," *IEEE Transactions on Terahertz Science and Technology*, vol. 7, no. 1, pp. 93–97, 2016.
- [32] O. Mitrofanov, R. James, F. A. Fernández, T. K. Mavrogordatos, and J. A. Harrington, "Reducing transmission losses in hollow thz waveguides," *IEEE Transactions on Terahertz Science and Technology*, vol. 1, no. 1, pp. 124–132, 2011.
- [33] C. Yeh and F. I. Shimabukuro, *The essence of dielectric waveguides*. Springer New York, NY, 2008.
- [34] F. Xu and K. Wu, "Substrate integrated nonradiative dielectric waveguide structures directly fabricated on printed circuit boards and metallized dielectric layers," *IEEE Transactions on Microwave Theory and Techniques*, vol. 59, no. 12, pp. 3076–3086, 2011.
- [35] D. Li, P. Yang, and K. Wu, "An order-reduced volume-integral equation approach for analysis of nrd-guide and h-guide millimeter-wave circuits," *IEEE transactions on microwave theory and techniques*, vol. 53, no. 3, pp. 799–812, 2005.



- [36] D. Li and K. Wu, "A generalized surface-volume integral-equation (svie) approach for analysis of hybrid planar/nrd-guide integrated circuits," *IEEE transactions on microwave theory and techniques*, vol. 53, no. 9, pp. 2732–2742, 2005.
- [37] V. Lombardi, M. Bozzi, and L. Perregrini, "Analysis of dielectric waveguides with the variational meshless method," in *2019 European Microwave Conference in Central Europe (EuMCE)*. IEEE, 2019, pp. 475–478.
- [38] E. A. Marcatili, "Dielectric rectangular waveguide and directional coupler for integrated optics," *Bell System Technical Journal*, vol. 48, no. 7, pp. 2071–2102, 1969.
- [39] J. Attari, H. Boutayeb, and K. Wu, "A simplified implementation of substrate integrated non-radiative dielectric waveguide at millimeter-wave frequencies," *Progress In Electromagnetics Research C*, vol. 55, pp. 83–94, 2014.
- [40] K. Fujimoto, *Mobile antenna systems handbook*. Artech House, 2008.
- [41] M. Z. A. A. Aziz and M. K. A. Rahim, "Wireless mimo channel capacity using double stage diversity technique," *Wireless Personal Communications*, vol. 85, pp. 2067–2081, 2015.
- [42] H.-C. Lo, D.-B. Lin, T.-C. Yang, H.-J. Li *et al.*, "Effect of polarization on the correlation and capacity of indoor mimo channels," *International Journal of Antennas and Propagation*, vol. 2012, 2012.
- [43] W. Gao, W. S. Lee, X. Yu, M. Fujita, T. Nagatsuma, C. Fumeaux, and W. Withayachumnankul, "Characteristics of effective-medium-clad dielectric waveguides," *IEEE Transactions on Terahertz Science and Technology*, vol. 11, no. 1, pp. 28–41, 2020.
- [44] A. Malekabadi, S. A. Charlebois, D. Deslandes, and F. Boone, "High-resistivity silicon dielectric ribbon waveguide for single-mode low-loss propagation at f/g-bands," *IEEE Transactions on Terahertz Science and Technology*, vol. 4, no. 4, pp. 447–453, 2014.
- [45] H.-T. Zhu, Q. Xue, S.-W. Liao, S. W. Pang, L. Chiu, Q.-Y. Tang, and X.-H. Zhao, "Low-cost narrowed dielectric microstrip line—a three-layer dielectric waveguide using pcb technology for millimeter-wave applications," *IEEE Transactions on Microwave Theory and Techniques*, vol. 65, no. 1, pp. 119–127, 2016.
- [46] Y. Cassivi and K. Wu, "Substrate integrated nonradiative dielectric waveguide," *IEEE Microwave and wireless components letters*, vol. 14, no. 3, pp. 89–91, 2004.

- [47] W. V. McLevige, T. Itoh, and R. Mittra, "New waveguide structures for millimeter-wave and optical integrated circuits," *IEEE Transactions on microwave theory and techniques*, vol. 23, no. 10, pp. 788–794, 1975.
- [48] M. Boyuan, J. Pan, D. Yang, and Y.-X. Guo, "Investigation on homogenization of flat and conformal stacked dielectric resonator antennas," *IEEE Transactions on Antennas and Propagation*, vol. 70, no. 2, pp. 1482–1487, 2021.
- [49] K. Wu, Y. J. Cheng, T. Djerafi, and W. Hong, "Substrate-integrated millimeter-wave and terahertz antenna technology," *Proceedings of the IEEE*, vol. 100, no. 7, pp. 2219–2232, 2012.
- [50] S. Barone, M. Narcowich, and F. Narcowich, "Floquet theory and applications," *Physical Review A*, vol. 15, no. 3, p. 1109, 1977.
- [51] G. P. Tolstov, *Fourier series*. Courier Corporation, 2012.
- [52] D. J. Hoppe, *Impedance boundary conditions in electromagnetics*. CRC Press, 2018.
- [53] C. A. Balanis, *Advanced engineering electromagnetics*. John Wiley & Sons, 2012.
- [54] P. Griffin, P. Nagel, and R. Koshel, "The plane-wave expansion method," *Journal of Mathematical Physics*, vol. 15, no. 11, pp. 1913–1917, 1974.
- [55] K. Brakora, C. Barth, and K. Sarabandi, "A plane-wave expansion method for analyzing propagation in 3d periodic ceramic structures," in *2005 IEEE Antennas and Propagation Society International Symposium*, vol. 2. IEEE, 2005, pp. 192–195.
- [56] T.-H. E. Fields, *Time harmonic Electromagnetic fields*. McGraw-Hill, 1961.
- [57] A. A. Sakr, W. Dyab, and K. Wu, "Modeling effective anisotropy of substrate integrated dielectric waveguides for polarization diversity," *IEEE Transactions on Microwave Theory and Techniques*, vol. 66, no. 6, pp. 2953–2966, 2018.
- [58] A. Patrovsky, *Hybrid integration of synthesized dielectric image waveguides in substrate integrated circuit technology and its millimeter wave applications*. École Polytechnique de Montréal, 2008.
- [59] G. Gallot, S. Jamison, R. McGowan, and D. Grischkowsky, "Terahertz waveguides," *JOSA B*, vol. 17, no. 5, pp. 851–863, 2000.
- [60] [Online]. Available: [https://www.vadiodes.com/images/AppNotes/VDI\\_Waveguide\\_Designations.pdf](https://www.vadiodes.com/images/AppNotes/VDI_Waveguide_Designations.pdf)

- [61] P.-S. Kildal, E. Alfonso, A. Valero-Nogueira, and E. Rajo-Iglesias, “Local metamaterial-based waveguides in gaps between parallel metal plates,” *IEEE Antennas and wireless propagation letters*, vol. 8, pp. 84–87, 2008.
- [62] D. Li, N. Khaddaj Mallat, and K. Wu, “Quasi-tem rectangular waveguides with frequency selective surface walls: Part i—electrical properties and geometrical characteristics,” *International Journal of Numerical Modelling: Electronic Networks, Devices and Fields*, vol. 27, no. 2, pp. 334–352, 2014.
- [63] —, “Quasi-tem rectangular waveguides with frequency selective surface walls: Part ii—physical mechanism,” *International Journal of Numerical Modelling: Electronic Networks, Devices and Fields*, vol. 27, no. 2, pp. 353–368, 2014.
- [64] E. Rajo-Iglesias, M. Ferrando-Rocher, and A. U. Zaman, “Gap waveguide technology for millimeter-wave antenna systems,” *IEEE Communications Magazine*, vol. 56, no. 7, pp. 14–20, 2018.
- [65] S. Farjana, M. Ghaderi, A. U. Zaman, S. Rahiminejad, P. Lundgren, and P. Enoksson, “Low-loss gap waveguide transmission line and transitions at 220–320 ghz using dry film micromachining,” *IEEE Transactions on Components, Packaging and Manufacturing Technology*, vol. 11, no. 11, pp. 2012–2021, 2021.
- [66] F. Benabid, P. Roberts, F. Couny, and P. S. Light, “Light and gas confinement in hollow-core photonic crystal fibre based photonic microcells,” *Journal of the European Optical Society-Rapid Publications*, vol. 4, 2009.
- [67] K. J. Rowland, “Guiding light in low-index media via multilayer waveguides.” Ph.D. dissertation, 2010.
- [68] S. Jamison, R. McGowan, and D. Grischkowsky, “Single-mode waveguide propagation and reshaping of sub-ps terahertz pulses in sapphire fibers,” *Applied physics letters*, vol. 76, no. 15, pp. 1987–1989, 2000.
- [69] R. Mendis and D. Grischkowsky, “Plastic ribbon thz waveguides,” *Journal of Applied Physics*, vol. 88, no. 7, pp. 4449–4451, 2000.
- [70] A. Hassani, A. Dupuis, and M. Skorobogatiy, “Low loss porous terahertz fibers containing multiple subwavelength holes,” *Applied Physics Letters*, vol. 92, no. 7, 2008.
- [71] —, “Porous polymer fibers for low-loss terahertz guiding,” *Optics express*, vol. 16, no. 9, pp. 6340–6351, 2008.

- [72] S. Atakaramians, S. Afshar, B. M. Fischer, D. Abbott, and T. M. Monro, “Porous fibers: a novel approach to low loss thz waveguides,” *Optics Express*, vol. 16, no. 12, pp. 8845–8854, 2008.
- [73] N. Ranjkesh, M. Basha, A. Taeb, and S. Safavi-Naeini, “Silicon-on-glass dielectric waveguide—part ii: For thz applications,” *IEEE Transactions on Terahertz Science and Technology*, vol. 5, no. 2, pp. 280–287, 2015.
- [74] H. Amarloo, N. Ranjkesh, and S. Safavi-Naeini, “Terahertz silicon-bcb-quartz dielectric waveguide: An efficient platform for compact thz systems,” *IEEE Transactions on Terahertz Science and Technology*, vol. 8, no. 2, pp. 201–208, 2018.
- [75] H.-T. Zhu, Q. Xue, J.-N. Hui, and S. W. Pang, “Design, fabrication, and measurement of the low-loss soi-based dielectric microstrip line and its components,” *IEEE Transactions on Terahertz Science and Technology*, vol. 6, no. 5, pp. 696–705, 2016.
- [76] X. Yu, M. Sugeta, Y. Yamagami, M. Fujita, and T. Nagatsuma, “Simultaneous low-loss and low-dispersion in a photonic-crystal waveguide for terahertz communications,” *Applied Physics Express*, vol. 12, no. 1, p. 012005, 2019.
- [77] D. Headland, W. Withayachumnankul, W. S. L. Lee, M. Fujita, and T. Nagatsuma, “Dispersion in broadband terahertz photonic crystal waveguides employing bragg-mirror suppression,” in *2020 IEEE International Conference on Computational Electromagnetics (ICCEM)*. IEEE, 2020, pp. 23–24.
- [78] G. Matthaei, D. C. Park, Y. M. Kim, and D. Johnson, “A study of the filter properties of single and parallel-coupled dielectric-waveguide gratings,” *IEEE transactions on microwave theory and techniques*, vol. 31, no. 10, pp. 825–835, 1983.
- [79] D. I. Kim, D. Kawabe, K. Araki, and Y. Naito, “Directly connected image guide 3-db couplers with very flat couplings,” *IEEE transactions on microwave theory and techniques*, vol. 32, no. 6, pp. 621–627, 1984.
- [80] R. E. Horn, H. Jacobs, and E. Freibergs, “Integrated tunable cavity gunn oscillator for 60-ghz operation in image line waveguide,” *IEEE transactions on microwave theory and techniques*, vol. 32, no. 2, pp. 171–176, 1984.
- [81] C.-M. Liu, L.-P. Carignan, S. Xiao, Y. He, and K. Wu, “Substrate-integrated hybrid metallo-dielectric waveguide architecture for millimeter-wave and terahertz applications,” *IEEE Transactions on Microwave Theory and Techniques*, 2023.

- [82] A. V. Subashiev and S. Luryi, “Modal control in semiconductor optical waveguides with uniaxially patterned layers,” *Journal of lightwave technology*, vol. 24, no. 3, p. 1513, 2006.
- [83] J. Birman, S. Edwards, R. Friend, M. Rees, D. Sherrington, and G. Veneziano. (2009) Effective medium theory principles and applications.
- [84] M. Moradi, M. S. Sharawi, and K. Wu, “Analytical model of guided waves in periodically perforated dielectric structure and its applications to terahertz substrate-integrated image guide (siig),” *IEEE Transactions on Microwave Theory and Techniques*, vol. 71, no. 10, pp. 4236–4246, 2023.
- [85] A. Mizrahi and L. Schächter, “Bragg reflection waveguides with a matching layer,” *Optics Express*, vol. 12, no. 14, pp. 3156–3170, 2004.
- [86] [Online]. Available: <https://www.everythingrf.com/tech-resources/waveguides-sizes>
- [87] M. Moallem, J. East, and K. Sarabandi, “A broadband, micromachined rectangular waveguide to cavity-backed coplanar waveguide transition using impedance-taper technique,” *IEEE Transactions on Terahertz Science and Technology*, vol. 4, no. 1, pp. 49–55, 2013.
- [88] N. Ranjkesh, M. Basha, A. Taeb, A. Zandieh, S. Gigoyan, and S. Safavi-Naeini, “Silicon-on-glass dielectric waveguide—part i: For millimeter-wave integrated circuits,” *IEEE Transactions on Terahertz Science and Technology*, vol. 5, no. 2, pp. 268–279, 2015.
- [89] S. Koenig, D. Lopez-Diaz, J. Antes, F. Boes, R. Henneberger, A. Leuther, A. Tessmann, R. Schmogrow, D. Hillerkuss, R. Palmer *et al.*, “Wireless sub-thz communication system with high data rate,” *Nature photonics*, vol. 7, no. 12, pp. 977–981, 2013.
- [90] R. Knox and P. Toullos, “Integrated circuits for the millimeter through optical frequency range,” in *Proc. Symp. Submillimeter Waves*, vol. 20. Brooklyn, NY, 1970, pp. 497–515.
- [91] B. Hu, L. Bi, and S. Dai, “The orthogonality between complex fuzzy sets and its application to signal detection,” *Symmetry*, vol. 9, no. 9, p. 175, 2017.
- [92] M. Moradi, M. S. Sharawi, and K. Wu, “Exploring low-loss wideband substrate-integrated image guides (siig) for terahertz applications,” *IEEE Transactions on Terahertz Science and Technology*, 2023.

## APPENDIX A

### Detailed Information on Developing Eigenvalue Equation

For the  $TM_z$  modes, based on the orthogonal property of complex exponential functions, the orthogonal function of (2.7) can be considered as:

$$f_{(k,l)} = e^{j\frac{2\pi k}{a}x} e^{j\frac{2\pi l}{c}y} \quad (\text{A.1})$$

by multiplying (A.1) to (2.7) and calculating the integral over a unit-cell [91], we have:

$$\begin{aligned} \sum_n \sum_q \left[ \left( \frac{2\pi n}{a} + k_{x_0} \right)^2 + \left( \frac{2\pi q}{c} + k_{y_0} \right)^2 \right] a_{nq} \\ \delta \left( \frac{2\pi l}{c} - \frac{2\pi q}{c} \right) \delta \left( \frac{2\pi k}{a} - \frac{2\pi n}{a} \right) = \\ k_0^2 \sum_m \sum_p \sum_n \sum_q a_{nq} b_{mp} \delta \left( \frac{2\pi l}{c} - \frac{2\pi p}{c} - \frac{2\pi q}{c} \right) \\ \delta \left( \frac{2\pi k}{a} - \frac{2\pi m}{a} - \frac{2\pi p}{a} \right) \end{aligned} \quad (\text{A.2})$$

where  $\delta_{(n)}$  is the *Kronecker Delta* function, which is defined as:

$$\delta_{(n)} = \begin{cases} 1 & n = 0 \\ 0 & n \neq 0 \end{cases} \quad (\text{A.3})$$

The convolution in equation (A.2) leads to:

$$\begin{aligned} a_{(n,q)} \left[ \left( \frac{2\pi n}{a} + k_{x_0} \right)^2 + \left( \frac{2\pi q}{c} + k_{y_0} \right)^2 \right] = \\ k_0^2 \sum_m \sum_p a_{(m,p)} b_{(n-m,q-p)} \end{aligned} \quad (\text{A.4})$$

A careful review of the above equation reveals it is identical to (2.7). The unknown variable  $b_{(n,q)}$  is the *Fourier Series* coefficient, which for the rectangular perforation (as shown in Fig.

2.1a) can be calculated as:

$$\begin{aligned}
b_{(n,q)} &= \frac{1}{ac} \int_{-a/2}^{a/2} \int_{-c/2}^{c/2} \varepsilon_r e^{-j\frac{2\pi n}{a}x} e^{-j\frac{2\pi q}{c}y} dx dy \\
&\quad - \frac{1}{ac} \int_{-b/2}^{b/2} \int_{-d/2}^{d/2} \varepsilon_r e^{-j\frac{2\pi n}{a}x} e^{-j\frac{2\pi q}{c}y} dx dy \\
&\quad + \frac{1}{ac} \int_{-b/2}^{b/2} \int_{-d/2}^{d/2} e^{-j\frac{2\pi n}{a}x} e^{-j\frac{2\pi q}{c}y} dx dy \\
&= \varepsilon_r \delta_{(n,q)} - (\varepsilon_r - 1) \frac{bd}{ac} \text{sinc}\left(\frac{\pi nb}{a}\right) \text{sinc}\left(\frac{\pi qd}{c}\right)
\end{aligned} \tag{A.5}$$

where  $b$  and  $d$  are the perforation sizes along the  $x$ , and  $y$  directions, respectively. For the circular perforations (as shown in Fig. 2.1b),  $b_{(n,q)}$  can be calculated as:

$$\begin{aligned}
b_{(n,q)} &= \frac{2\pi}{a^2} \int_0^a \varepsilon_r J_0 \left( \sqrt{\left(\frac{2\pi nr}{a}\right)^2 + \left(\frac{2\pi qr}{a}\right)^2} \right) r dr \\
&\quad - \frac{2\pi}{a^2} \int_0^{b/2} \varepsilon_r J_0 \left( \sqrt{\left(\frac{2\pi nr}{a}\right)^2 + \left(\frac{2\pi qr}{a}\right)^2} \right) r dr \\
&\quad + \frac{2\pi}{a^2} \int_0^{b/2} J_0 \left( \sqrt{\left(\frac{2\pi nr}{a}\right)^2 + \left(\frac{2\pi qr}{a}\right)^2} \right) r dr \\
&= \varepsilon_r \delta_{(n,q)} - (\varepsilon_r - 1) \frac{\pi b^2}{a^2} \frac{2J_1 \left( \sqrt{\left(\frac{2\pi nb}{a}\right)^2 + \left(\frac{2\pi qb}{a}\right)^2} \right)}{\left( \sqrt{\left(\frac{2\pi nb}{a}\right)^2 + \left(\frac{2\pi qb}{a}\right)^2} \right)}
\end{aligned} \tag{A.6}$$

where  $a$  is the perforation size. It is worth mentioning that the eigenvalue equation for the  $TE_z$  modes (i.e., (2.18)) can be achieved by following the same procedure.

## APPENDIX B

### Refining Insights into Analytical Methods Solutions with MATLAB and MAPLE Software

In this section, we furnish comprehensive details on the generation and resolution procedures for the eigen-equations developed in Chapter 2.

#### Extracting the effective properties of periodic perforations for TMz mode:

To begin, Equation (2.11) can be transformed into an ordinary eigen-equation as follows:

$$k_0^{-2} \begin{bmatrix} \mathbf{a} \end{bmatrix}_{nq \times 1} = \underbrace{\begin{bmatrix} \mathbf{A} \end{bmatrix}_{nq \times nq}^{-1} \begin{bmatrix} \mathbf{B} \end{bmatrix}_{nq \times mp}}_{\begin{bmatrix} \mathbf{C} \end{bmatrix}} \begin{bmatrix} \mathbf{a} \end{bmatrix}_{mp \times 1} \quad (\text{B.1})$$

As indicated in the above equation, calculating matrix  $[\mathbf{C}]$  requires to first calculate matrix  $[\mathbf{A}]$  and matrix  $[\mathbf{B}]$ . Careful review of (2.8) reveals that developing these matrices requires first defining the number of summed terms. Accordingly, we considered  $m$ ,  $n$ ,  $p$ , and  $q$  to be an integer ranging from  $N$  to  $-N$  which make the  $[\mathbf{A}]$  and  $[\mathbf{B}]$  to have the size equal to  $(2N + 1)^2$  by  $(2N + 1)^2$ . By having the size of the unit-cell ( $a$  and  $c$ ), size of the perforation ( $b$  and  $d$ ), and the substrate material ( $\varepsilon_r$ ) we can develop matrix  $[\mathbf{B}]$ . Developing matrix  $[\mathbf{A}]$  requires definition of  $k_{x_0}$  and  $k_{y_0}$ . One way to define these values is considering the propagated field has a phase shift of  $\Delta\phi_x$  and  $\Delta\phi_y$  along the unit-cell and calculate the corresponding  $k_{x_0}$  and  $k_{y_0}$ .

Accordingly, the procedure for extracting eigenvalues can be summarized as follows:

- Defining the phase shift along the unit-cell ( $\Delta\phi_x$  and  $\Delta\phi_y$ )
- Calculating the propagating constant along  $x$ - and  $y$ -direction ( $k_{x_0}$  and  $k_{y_0}$ ) and consequently  $k_0$
- Sweeping  $m$ ,  $n$ ,  $p$ , and  $q$  from  $N$  to  $-N$  and developing the  $[\mathbf{A}]$  and  $[\mathbf{B}]$  matrices



- Calculating matrix  $[C]$
- Calculating eigen-value and eigen-vector of matrix  $[C]$
- Calculating  $\varepsilon'_{\text{eff}}$  and  $\varepsilon''_{\text{eff}}$
- Repeating the above steps for another value of phase shift ( $\Delta\phi_x$  and  $\Delta\phi_y$ )

### MATLAB Code for Analyzing the Investigated Unit-Cell

In this section, we present MATLAB code employed for extracting the effective permittivity and effective loss of a unit-cell. We considered a rectangular unit-cell made of Alumina substrate, which has relative permittivity equal to  $\varepsilon' = 9.4$  and loss tangent of  $\tan\delta = 6 \times 10^{-3}$ . The perforations have periodicity equal to  $a = c = 290 \mu\text{m}$  and dimensions of  $b = d = 200 \mu\text{m}$ . The following MATLAB code is utilized, and Figs. B.1 and B.2 display the real and imaginary parts of the cut-off frequency for various propagating modes.

```

1      %%MATLAB CODE
2      clear;
3      clc;
4
5      %% Defining the Variables
6
7      %%%% Defining the Floquet and Foruior series
           Numbers
8      N = 1;
9      M = N;
10     P = 1;
11     Q = P;
12
13     %%%% Defining Structural Parameters
14     a = 290e-6;
15     b = 200e-6;
16     c = 290e-6;
17     d = 200e-6;
18     eps_r = 9.4 + 5.6e-3*j;
19
20     %%%% First Region GAMMA to X

```

```

21     phi_x_1 = 0.01:0.01:pi;
22     kx_1 = phi_x_1 ./ a;
23     phi_y_1 = 0;
24     ky_1 = phi_y_1 ./ c;
25
26     %%%% Second Region X to M
27     phi_x_2 = pi;
28     kx_2 = phi_x_2 ./ a;
29     phi_y_2 = 0.01:0.01:pi;
30     ky_2 = phi_y_2 ./ c;
31
32     %%%% Third Region M to GAMMA
33     phi_x_3 = (pi - 0.01):-0.01:0.01;
34     kx_3 = phi_x_3 ./ a;
35     phi_y_3 = (pi - 0.01):-0.01:0.01;
36     ky_3 = phi_y_3 ./ c;
37
38     %%%% Defining the Coeficient Matrix
39     A_mat = zeros((2.*N + 1).*(2.*Q + 1), (2.*M + 1)
40         .*(2.*P + 1));
41     B_mat = zeros((2.*N + 1).*(2.*Q + 1), (2.*Q + 1)
42         .*(2.*Q + 1));
43
44     %%%% Defining the Results Matrix
45     freq_norm_1 = zeros((2.*N+1).*(2.*Q+1), (size(
46         kx_1,2)));
47     freq_norm_2 = zeros((2.*N+1).*(2.*Q+1), (size(
48         ky_2,2)));
49     freq_norm_3 = zeros((2.*N+1).*(2.*Q+1), (size(
50         kx_3,2)));
51
52     %% Calculating the Eigenvalue and Cut-off
53     Frequency
54
55     %%%% First Region GAMMA to X
56     counter = 1;

```

```

51     for kx_0 = kx_1
52     ky_0 = ky_1;
53     n_count = 0;
54     for n = -N:N
55     for q = -Q:Q
56     i = ((2.*N).* n_count) + (n + N + q + Q + 1);
57     m_count = 0;
58     for m = -M:M
59     for p = -P:P
60     j = ((2.*M).* m_count) + (m + M + p + P + 1);
61     A_mat(i,j) = b_nmqp_TMz(n,m,p,q,a,b,eps_r);
62     if i == j
63     B_mat(i,j) = (((2.*pi.*n./a) + kx_0).^2) +
        (((2.*pi.*q./c) + ky_0).^2);
64     end
65     end
66     m_count = m_count + 1;
67     end
68     end
69     n_count = n_count + 1;
70     end
71
72     C_mat = inv(A_mat) * B_mat;
73     eigen_value = sort((eig(C_mat)));
74     freq_norm_1(:,counter) = sqrt(eigen_value) ./
        (2.*pi);
75     counter = counter+1;
76     end
77
78     %%%% Second Region X to M
79     counter = 1;
80     for ky_0 = ky_2
81     kx_0 = kx_2;
82     n_count = 0;
83     for n = -N:N
84     for q = -Q:Q

```

```

85     i = ((2.*N).* n_count) + (n + N + q + Q + 1);
86     m_count = 0;
87     for m = -M:M
88     for p = -P:P
89     j = ((2.*M).* m_count) + (m + M + p + P + 1);
90     A_mat(i,j) = b_nmqp_TMz(n,m,p,q,a,b,eps_r);
91     if i == j
92     B_mat(i,j) = (((2.*pi.*n./a) + kx_0).^2) +
          (((2.*pi.*q./c) + ky_0).^2);
93     end
94     end
95     m_count = m_count + 1;
96     end
97     end
98     n_count = n_count + 1;
99     end
100
101     C_mat = inv(A_mat) * B_mat;
102     eigen_value = sort((eig(C_mat)));
103     freq_norm_2(:,counter) = sqrt(eigen_value) ./
          (2.*pi);
104     counter = counter+1;
105     end
106
107     %%%% Third Region M to GAMMA
108     counter = 1;
109     for kx_0 = kx_3
110     ky_0 = kx_0;
111     n_count = 0;
112     for n = -N:N
113     for q = -Q:Q
114     i = ((2.*N).* n_count) + (n + N + q + Q + 1);
115     m_count = 0;
116     for m = -M:M
117     for p = -P:P
118     j = ((2.*M).* m_count) + (m + M + p + P + 1);

```

```

119     A_mat(i,j) = b_nmqp_TMz(n,m,p,q,a,b,eps_r);
120     if i == j
121         B_mat(i,j) = (((2.*pi.*n./a) + kx_0).^2) +
            (((2.*pi.*q./c) + ky_0).^2);
122     end
123 end
124 m_count = m_count + 1;
125 end
126 end
127 n_count = n_count + 1;
128 end
129
130 C_mat = inv(A_mat) * B_mat;
131 eigen_value = sort((eig(C_mat)));
132 freq_norm_3(:,counter) = sqrt(eigen_value) ./
            (2.*pi);
133 counter = counter+1;
134 end
135
136 %% Attaching the Data's together
137
138 freq_norm_total = [freq_norm_1, freq_norm_2,
            freq_norm_3];
139 ka_total = 0.01:0.01:((3.*pi)-0.01);
140
141 %% Plotting the Data
142 figure;
143 grid on
144 hold on
145 plot(ka_total,real(freq_norm_total),'LineWidth',
            2)
146 xlabel('\fontname{Times New Roman} \fontsize
            {16} \bf k \times a')
147 ylabel('\fontname{Times New Roman} \fontsize
            {16} \bf Real Part of Normalized Frequency')
148 xlim([min(ka_total) max(ka_total)])

```

```

149
150     %% Plotting the Data
151     figure;
152     grid on
153     hold on
154     plot(ka_total,imag(freq_norm_total),'LineWidth'
155           ,2)
156     xlabel('\fontname{Times New Roman} \fontsize
157           {16} \bf k \times a')
158     ylabel('\fontname{Times New Roman} \fontsize
159           {16} \bf Imaginary Part of Normalized
160           Frequency')
161     xlim([min(ka_total) max(ka_total)])

```

```

1
2     function [out_putt] = b_nmqp_TMz(nn,mm,pp,qq,aa
3           ,bb,eps_rr)
4
5     if (nn==mm)&&(pp==qq)
6         out_putt = (eps_rr .* my_delta(nn-mm,qq-pp)) -
7           ((eps_rr - 1) .* (pi .* (bb .^ 2) ./ (aa .^
8             2)));
9     else
10        out_putt = (eps_rr .* my_delta(nn-mm,qq-pp)) -
11          ((eps_rr - 1) .* (pi .* (bb .^ 2) ./ (aa .^
12            2)) .* (2 .* besselj(1, sqrt(((2 .* pi .* (
13              nn - mm) .* bb ./ aa).^2) + ((2 .* pi .* (qq
14                - pp) .* bb ./ aa).^2)))) ./ sqrt(((2 .* pi
15                  .* (nn - mm) .* bb ./ aa).^2) + ((2 .* pi .*
16                    (qq - pp) .* bb ./ aa).^2)))));
17    end
18
19
20    end

```

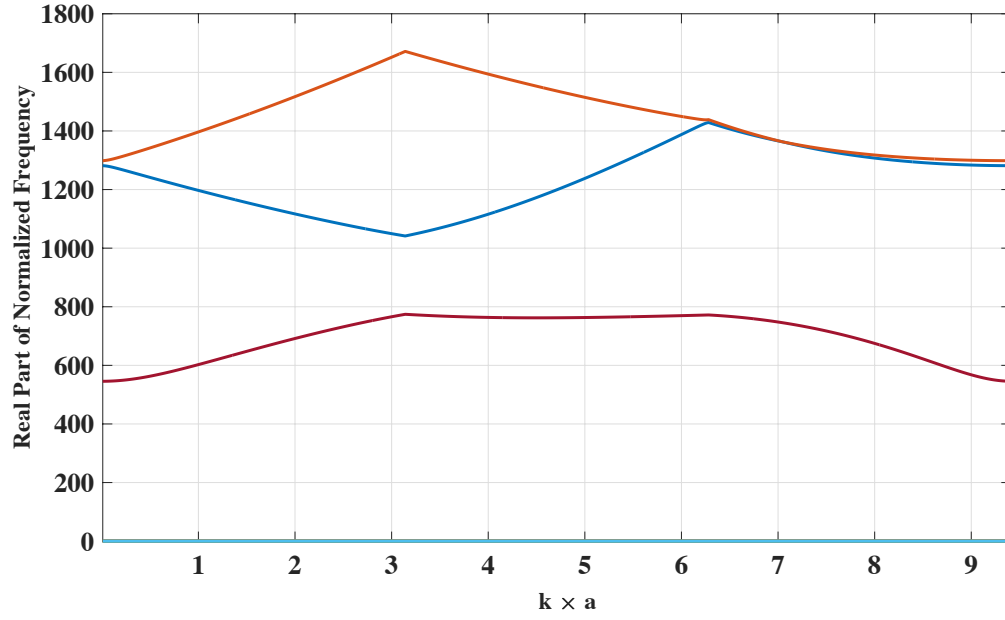


Figure B.1 Computed real part of the cut-off frequency for the initial propagating modes.

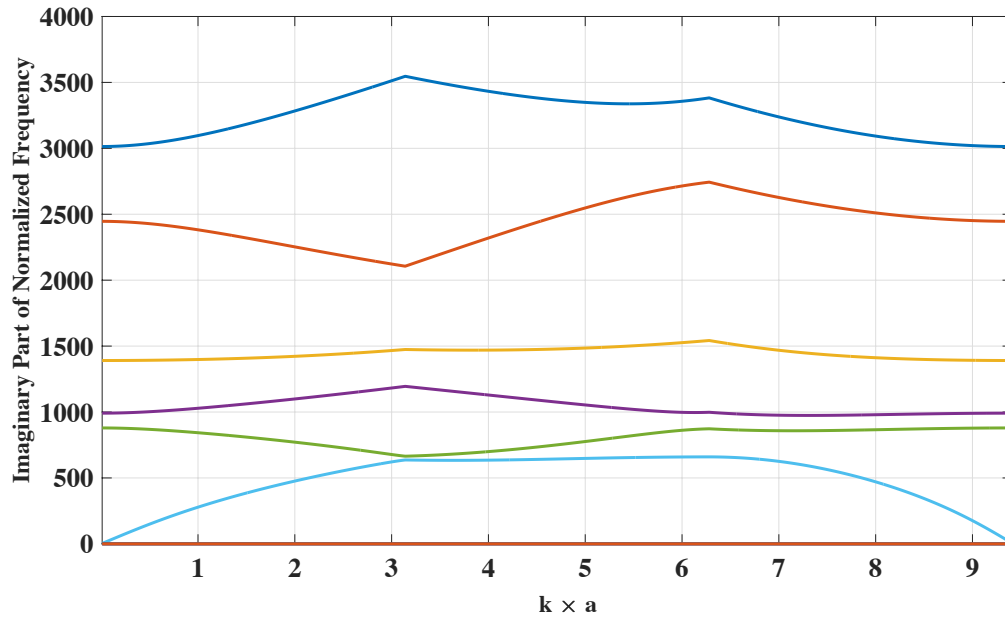


Figure B.2 Computed imaginary part of the cut-off frequency for the initial propagating modes.

Following the computation of cut-off frequencies for propagating modes, we employed the subsequent code to derive the effective permittivity and dissipation factor for each mode. The results are presented in Figs. B.3 and B.4.

```

1
2      %% Defining variables
3
4      C_0 = 299792458;
5      eps_eff_1 = zeros((2.*N+1).*(2.*Q+1), (size(
6          phi_x_1,2)));
7
8      %% Calculating Effective Permittivity
9
10     for i = 1:(2.*N+1).*(2.*Q+1)
11         eps_eff_1(i,:) = (sqrt((phi_x_1 .^ 2) + (
12             phi_y_1 .^ 2)) ./ (2 .* pi .* real(
13                 freq_norm_1(i,:))))).^2;
14         loss_eff_1(i,:) = (sqrt((phi_x_1 .^ 2) + (
15             phi_y_1 .^ 2)) ./ (2 .* pi .* imag(
16                 freq_norm_1(i,:))))).^2;
17     end
18
19     %% Plotting the Results
20
21     figure
22     grid on
23     hold on
24     xlabel('\fontname{Times New Roman} \fontsize
25         {16} \bf Normalized Frequency')
26     ylabel('\fontname{Times New Roman} \fontsize
27         {16} \bf Effective Permittivity')
28     xlim([0 800])
29
30     for i = 1:(2.*N+1).*(2.*Q+1)
31         plot(real(freq_norm_1(i,:)),eps_eff_1(i,:), '
32             LineWidth',2)
33     end

```



```

27      %%
28      figure
29      grid on
30      hold on
31      xlabel('\fontname{Times New Roman} \fontsize
          {16} \bf Normalized Frequency')
32      ylabel('\fontname{Times New Roman} \fontsize
          {16} \bf Effective Dissipation Factor')
33      xlim([0 800])
34
35      for i = 1:(2.*N+1).*(2.*Q+1)
36          plot(real(freq_norm_1(i,:)),loss_eff_1(i,:), '
              LineWidth',2)
37      end

```

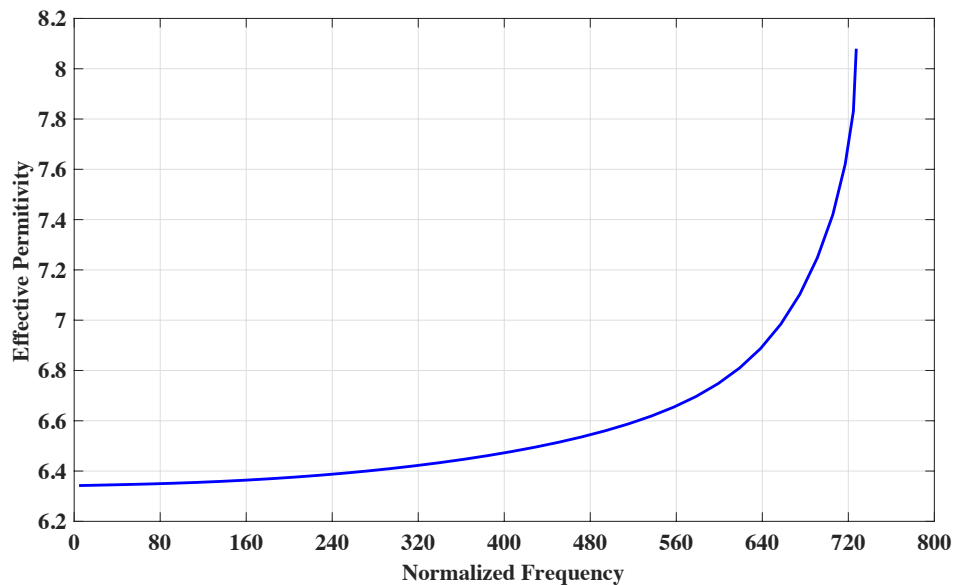


Figure B.3 Extracted effective permittivity of fundamental mode.

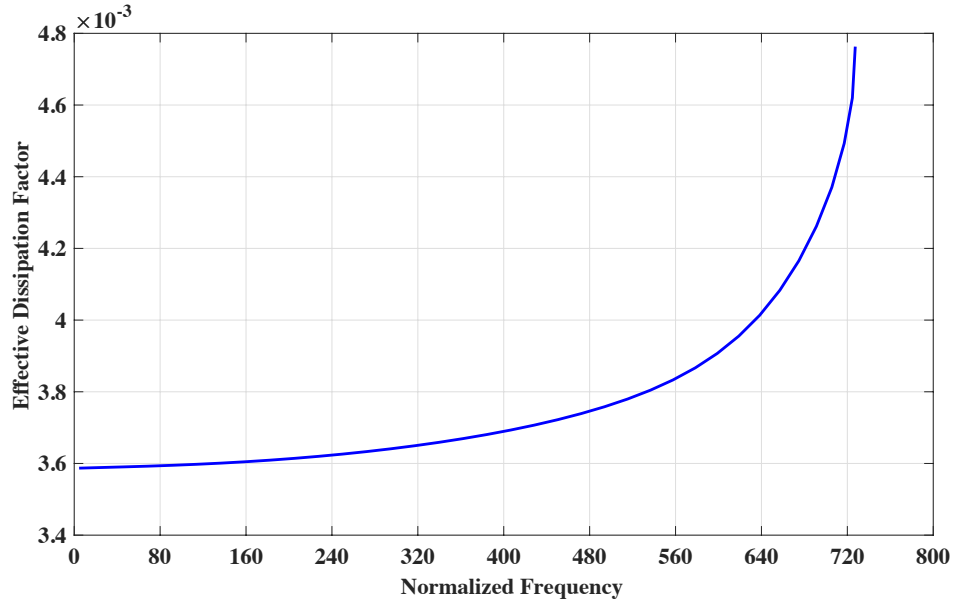


Figure B.4 Extracted effective dissipation factor of fundamental mode.

## Integrating MATLAB and MAPLE Software for Enhanced Solutions in Modified Modal Analysis

In this section, we offer comprehensive guidance on employing MATLAB and MAPLE software for implementing modified modal analysis and extracting the propagation constant along the guiding channel. To achieve this, follow the procedure outlined below:

1. The following code is employed to import the extracted effective permittivity and effective loss into MAPLE software and compute the  $k_y$  values.

```

c_0 := 299792458 :
ε_0 := 8.8542e-12 :
ε_r0 := 1 :
η_0 := 376.7303 :
μ_0 := 4·π·1e-7 :
ε_rm := 2.2 :
μ_rm := 1.000000065 :
σ_m := 35600000 :
ε_r1 := Matlab[getvar]("eps_loss_alumina"):
ε_r2 := Matlab[getvar]("eps_loss_eff"):
d := 300e-6 :
f := Vector(200) :
k_0 := Vector(200) :
η_m := Vector(200) :
k_y_sol_1 := Matrix(7, 200, fill = 1e9) :
k_y_sol_2 := Matrix(13, 200, fill = 1e9) :

```

**for**  $jj$  **from** 1 **by** 1 **to** 200 **do**:

$f[jj] := jj \cdot 1e9$  :

$\omega := 2 \cdot \pi \cdot f[jj]$  :

$k_0[jj] := 2 \cdot \pi \cdot \frac{f[jj]}{c_0}$  :

$\eta_m[jj] := \sqrt{\frac{I \cdot \omega \cdot \mu_0 \cdot \mu_{rm}}{\sigma_m + I \cdot \omega \cdot \epsilon_0 \cdot \epsilon_{rm}}}$  :

$func\_1 := (\epsilon_{r1} \cdot \eta_0 + \epsilon_{r0} \cdot \epsilon_{r1} \cdot \eta_m[jj]) \cdot k_{y1} \cdot \cos(k_{y1} \cdot d) + (\epsilon_{r1}^2 \cdot \eta_0 \cdot \eta_m[jj] - \epsilon_{r0} \cdot k_{y1}^2) \cdot \sin(k_{y1} \cdot d)$  :

$k_{y\_sol\_temp\_1} := \text{solve}(func\_1 = 0, k_{y1})$  :

**for**  $ii$  **from** 1 **by** 1 **to**  $nops([k_{y\_sol\_temp\_1}])$  **do**:

$k_{y\_sol\_1}[ii, jj] := k_{y\_sol\_temp\_1}[ii]$  :

**end do**:

$func\_2 := (\epsilon_{r2} \cdot \eta_0 + \epsilon_{r0} \cdot \epsilon_{r2} \cdot \eta_m[jj]) \cdot k_{y2} \cdot \cos(k_{y2} \cdot d) + (\epsilon_{r2}^2 \cdot \eta_0 \cdot \eta_m[jj] - \epsilon_{r0} \cdot k_{y2}^2) \cdot \sin(k_{y2} \cdot d)$  :

$k_{y\_sol\_temp\_2} := \text{solve}(func\_2 = 0, k_{y2})$  :

**for**  $iii$  **from** 1 **by** 1 **to**  $nops([k_{y\_sol\_temp\_2}])$  **do**:

$k_{y\_sol\_2}[iii, jj] := k_{y\_sol\_temp\_2}[iii]$  :

**end do**:

**end do**:

$k_{y\_sol\_1}$

2085.659625 + 0.03827850424 I	2085.675480 + 0.05413338998 I	2085.687647 + 0.06629903733 I	2085.697904
-2085.659625 - 0.03827850424 I	-2085.675480 - 0.05413338998 I	-2085.687647 - 0.06629903733 I	-2085.697904
10928.72903 + 0.01233841811 I	10928.73414 + 0.01744914252 I	10928.73807 + 0.02137073302 I	10928.74137
-10928.72903 - 0.01233841811 I	-10928.73414 - 0.01744914252 I	-10928.73807 - 0.02137073302 I	-10928.74137
-62911.68325 - 0.002229008821 I	-62911.68417 - 0.003152294409 I	-62911.68488 - 0.003860756315 I	-62911.68548
62911.68325 + 0.002229008821 I	62911.68417 + 0.003152294409 I	62911.68488 + 0.003860756315 I	62911.68548
0.	0.	0.	

$k_{y\_sol\_2}$

-3179.719105 - 0.08788843229 I	-3179.755511 - 0.1242904818 I	-3179.783447 - 0.1522217514 I	-3179.806998
3179.719105 + 0.08788843229 I	3179.755511 + 0.1242904818 I	3179.783447 + 0.1522217514 I	3179.806998
0.	0.	0.	-31881.62207
11692.44487 + 0.03261686333 I	11692.45838 + 0.04612711190 I	11692.46875 + 0.05649385102 I	31881.62207
-11692.44487 - 0.03261686333 I	-11692.45838 - 0.04612711190 I	-11692.46875 - 0.05649385102 I	
21625.34299 + 0.01874179550 I	21625.35075 + 0.02650488285 I	21625.35671 + 0.03246170189 I	21625.36173
-21625.34299 - 0.01874179550 I	-21625.35075 - 0.02650488285 I	-21625.35671 - 0.03246170189 I	-21625.36173
-63068.40511 - 0.006598546980 I	-63068.40785 - 0.009331753811 I	-63068.40994 - 0.01142901684 I	11692.47749
63068.40511 + 0.006598546980 I	63068.40785 + 0.009331753811 I	63068.40994 + 0.01142901684 I	-11692.47749
$1. \times 10^9$	$1. \times 10^9$	$1. \times 10^9$	$1. \times 10^9$
$\vdots$	$\vdots$	$\vdots$	$\vdots$

*with(Matlab)* :

`setvar("ky_1_maple",  $k_{y\_sol\_1}$ )`

`setvar("ky_2_maple",  $k_{y\_sol\_2}$ )`

`setvar("eps_r1",  $\epsilon_{r1}$ )`

`setvar("eps_r2",  $\epsilon_{r2}$ )`

`setvar("k_0",  $k_0$ )`

`setvar("f",  $f$ )`

2. The following code is used to import the calculated  $k_y$  values into MATLAB software for post-processing the data and computing the effective permittivity of each substrate section.

```

1      clear;
2      clc;
3
4
5      %% loadong file from maple and sorting to find
        the first modes
6      load("ky_maple.mat");
7      ky_1_sorted = sort(ky_1_maple);
8      ky_2_sorted = sort(ky_2_maple);
9
10     %% removing the negative roots
11     ky_1_final = [ky_1_sorted(3,:); ky_1_sorted
        (5,:); ky_1_sorted(7,:)];
12     ky_2_final = [ky_2_sorted(3,:); ky_2_sorted
        (5,:); ky_2_sorted(7,:)];
13
14     f = f';
15     k_0 = k_0';
16
17     %% Calculating the effecctive permittivity
18     eps_eff_1 = zeros(size(ky_1_final,1),size(
        ky_1_final,2));
19     eps_eff_1(1,:) = eps_r1 - ((ky_1_final(1,:) .^
        2) ./ (k_0(1,:) .^ 2));
20     eps_eff_1(2,:) = eps_r1 - ((ky_1_final(2,:) .^
        2) ./ (k_0(1,:) .^ 2));
21     eps_eff_1(3,:) = eps_r1 - ((ky_1_final(3,:) .^
        2) ./ (k_0(1,:) .^ 2));
22
23     eps_eff_2 = zeros(size(ky_2_final,1),size(
        ky_2_final,2));
24     eps_eff_2(1,:) = eps_r2 - ((ky_2_final(1,:) .^
        2) ./ (k_0(1,:) .^ 2));

```

```

25         eps_eff_2(2,:) = eps_r2 - ((ky_2_final(2,:) .^
           2) ./ (k_0(1,:) .^ 2));
26         eps_eff_2(3,:) = eps_r2 - ((ky_2_final(3,:) .^
           2) ./ (k_0(1,:) .^ 2));
27
28         %% saving the data to use in maple
29         save('C:\Program Files\MATLAB\R2022a\bin\win64\
           eps_eff.mat');

```

3. The following code is employed to import the calculated effective permittivity into MAPLE software and determine the  $k_x$  values.

```

ε_eff_1 := Matlab[getvar]("eps_eff_1") :
ε_eff_2 := Matlab[getvar]("eps_eff_2") :
k_0 := Matlab[getvar]("k_0") :
w_c := 400e-6 :
k_x_sol_1 := Matrix(9, 200, fill=1e9) :
k_x_sol_2 := Matrix(9, 200, fill=1e9) :
k_x_sol_3 := Matrix(9, 200, fill=1e9) :

for jj from 1 by 1 to 200 do:
    func_1 := 2·√((ε_eff_2[1,jj] - ε_eff_1[1,jj])·k_0[jj]2 - k_x_12·k_x_1·cos(k_x_1·w_c)
    + ((ε_eff_2[1,jj] - ε_eff_1[1,jj])·k_0[jj]2 - 2·(k_x_12))·sin(k_x_1·w_c) :
    k_x_sol_1_temp := solve(func_1=0, k_x_1) :
    for ii from 1 by 1 to nops([k_x_sol_1_temp]) do:
        k_x_sol_1[ii,jj] := k_x_sol_1_temp[ii] :
    end do:
    func_2 := 2·√((ε_eff_2[2,jj] - ε_eff_1[2,jj])·k_0[jj]2 - k_x_22·k_x_2·cos(k_x_2·w_c)
    + ((ε_eff_2[2,jj] - ε_eff_1[2,jj])·k_0[jj]2 - 2·(k_x_22))·sin(k_x_2·w_c) :
    k_x_sol_2_temp := solve(func_2=0, k_x_2) :
    for ii from 1 by 1 to nops([k_x_sol_2_temp]) do:
        k_x_sol_2[ii,jj] := k_x_sol_2_temp[ii] :
    end do:
    func_3 := 2·√((ε_eff_2[3,jj] - ε_eff_1[3,jj])·k_0[jj]2 - k_x_32·k_x_3·cos(k_x_3·w_c)
    + ((ε_eff_2[3,jj] - ε_eff_1[3,jj])·k_0[jj]2 - 2·(k_x_32))·sin(k_x_3·w_c) :
    k_x_sol_3_temp := solve(func_3=0, k_x_3) :
    for ii from 1 by 1 to nops([k_x_sol_3_temp]) do:
        k_x_sol_3[ii,jj] := k_x_sol_3_temp[ii] :
    end do:
end do:

```

[illegible]

[illegible]

$k_{x\_sol\_3}$		
0.	0.	0.
$-7239.714123 + 0.00004320279318 \text{ I}$	$-7239.714954 + 0.00006109769006 \text{ I}$	$-7239.716354 + 0.000074821111 \text{ I}$
$7239.714123 - 0.00004320279318 \text{ I}$	$7239.714954 - 0.00006109769006 \text{ I}$	$7239.716354 - 0.000074821111 \text{ I}$
$-14470.66845 + 0.00008823123555 \text{ I}$	$-14470.67015 + 0.0001247772190 \text{ I}$	$-14470.67301 + 0.00015281911 \text{ I}$
$14470.66845 - 0.00008823123555 \text{ I}$	$14470.67015 - 0.0001247772190 \text{ I}$	$14470.67301 - 0.00015281911 \text{ I}$
0.	0.	0.
$1. \times 10^9$	$1. \times 10^9$	$1. \times 10^9$
$1. \times 10^9$	$1. \times 10^9$	$1. \times 10^9$
$1. \times 10^9$	$1. \times 10^9$	$1. \times 10^9$

```
with(Matlab) :
setvar("kx_mode_1",k_x_sol_1)
setvar("kx_mode_2",k_x_sol_2)
setvar("kx_mode_3",k_x_sol_3)
```

4. The following code is used to import the calculated  $k_x$  values into MATLAB software, conduct post-processing on the data, and compute the propagation constants for each propagating modes.

```

1
2      %% loading file from maple and sorting to find
      the first modes
3      load("kx_maple.mat");
4      kx_mode_p1_sorted = sort(kx_mode_1);
5      kx_mode_p2_sorted = sort(kx_mode_2);
6      kx_mode_p3_sorted = sort(kx_mode_3);
7
8      % removing the negative roots
9      kx_mode_p1_final = [kx_mode_p1_sorted(1,:);
      kx_mode_p1_sorted(3,:); kx_mode_p1_sorted
      (5,:)];
10     kx_mode_p2_final = [kx_mode_p2_sorted(1,:);
      kx_mode_p2_sorted(3,:); kx_mode_p2_sorted
      (5,:)];
11     kx_mode_p3_final = [kx_mode_p3_sorted(1,:);
      kx_mode_p3_sorted(3,:); kx_mode_p3_sorted
      (5,:)];
12
13     % removing the added data for correct sorting
14     for i = 1:3
15         for j = 1:200
16             if kx_mode_p1_final(i,j) == 1e9
17                 kx_mode_p1_final(i,j) = 0 ;
18             end
19             if kx_mode_p2_final(i,j) == 1e9
20                 kx_mode_p2_final(i,j) = 0 ;
21             end
22             if kx_mode_p3_final(i,j) == 1e9
23                 kx_mode_p3_final(i,j) = 0 ;
24             end
25         end

```

```

26         end
27
28
29         %% Calculating Kz
30         kz_11 = sqrt((eps_eff_2(1,:).*(k_0.^2)) - (
31             kx_mode_p1_final(1,:).^2));
32         beta_11 = real(kz_11);
33         beta_11_n = beta_11 ./ k_0;
34         alpha_11 = imag(kz_11);
35         alpha_11_dB = 10*log10(alpha_11);
36
37         kz_21 = sqrt((eps_eff_2(2,:).*(k_0.^2)) - (
38             kx_mode_p1_final(1,:).^2));
39         beta_21 = real(kz_21);
40         beta_21_n = beta_21 ./ k_0;
41         alpha_21 = imag(kz_21);
42         alpha_21_dB = 10*log10(alpha_21);

```



## APPENDIX C

### Extracting the Effective Properties of Periodic Perforated Lossy Dielectric Substrate Using Ansys HFSS and CST Suite Studio Software

In this section, we present a detailed procedure for extracting the effective permittivity and effective loss of a lossy dielectric substrate with periodic perforations.

#### Ansys HFSS Simulation

Extracting the effective permittivity and effective loss of periodic perforations in a lossy dielectric substrate can be accomplished by following the procedure outlined below:

1. To begin, as shown in Fig. C.1, we initially draw a rectangular unit-cell made of Alumina substrate, which has relative permittivity equal to  $\epsilon' = 9.4$  and loss tangent of  $\tan \delta = 6 \times 10^{-3}$ . The perforations have periodicity equal to  $a = c = 290 \mu m$  and dimensions of  $b = d = 200 \mu m$ .

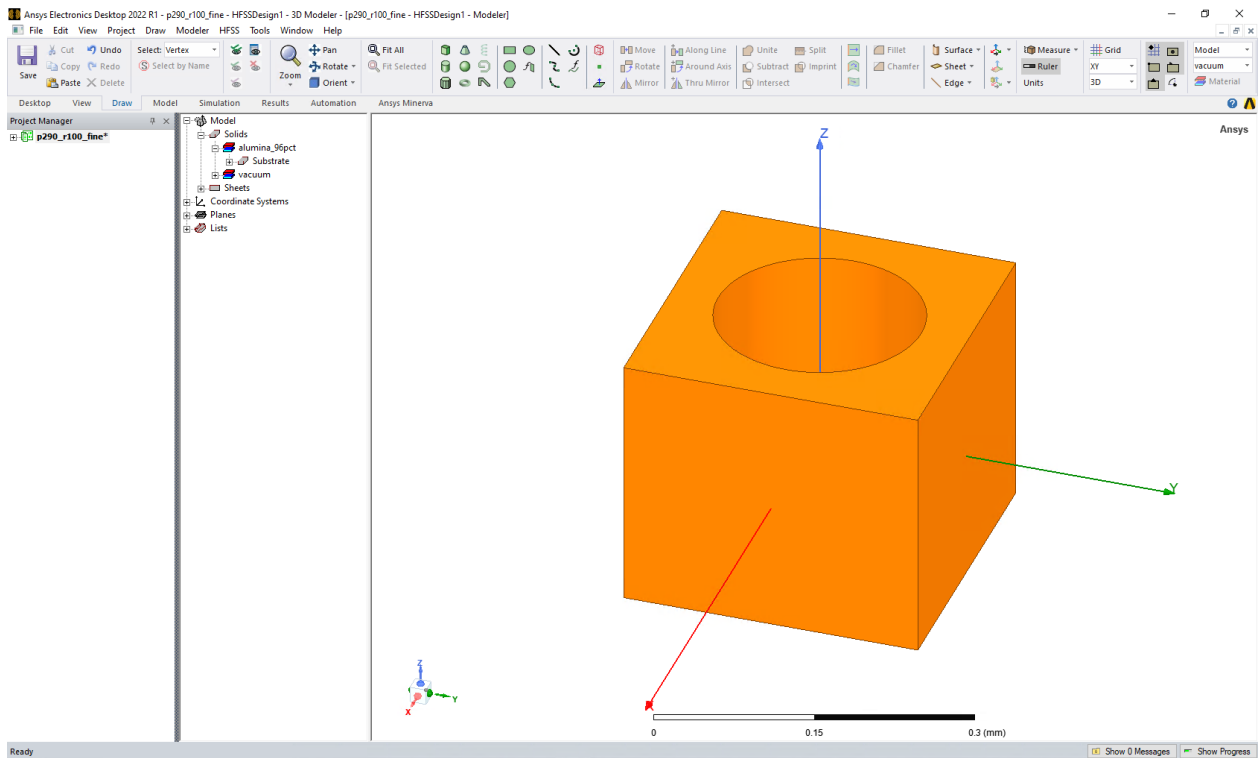


Figure C.1 Proposed unit-cell design in HFSS software.

2. As depicted in Fig. C.2, we opted for periodic boundary conditions along the  $y$ -direction. The phase difference between the specified boundaries is set as a variable and denoted as  $\phi_{y\_y}$ .

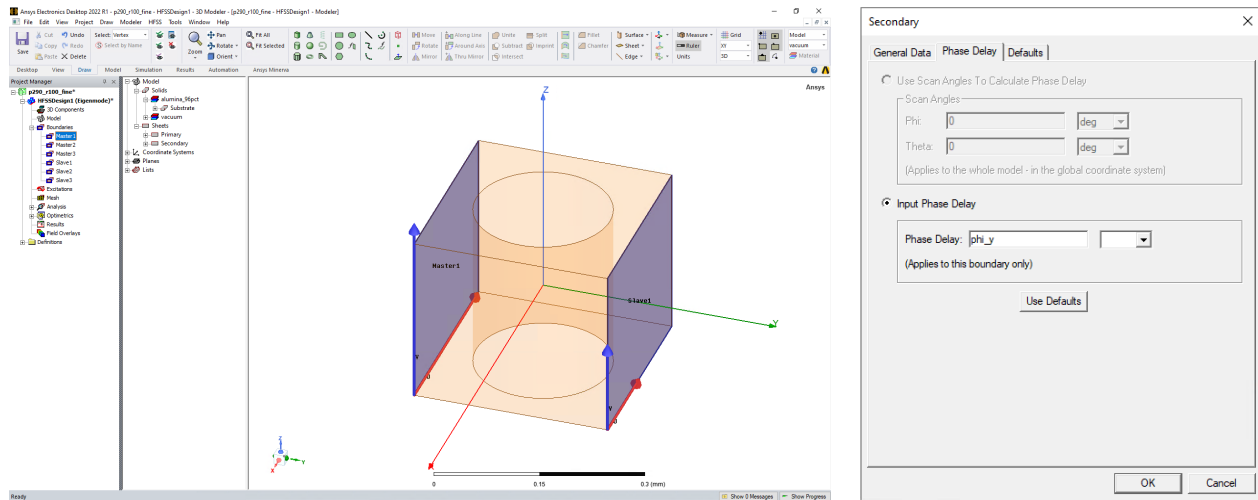


Figure C.2 Defining periodic boundary condition along  $y$ -direction.

3. As depicted in Fig. C.3, we opted for periodic boundary conditions along the  $x$ -direction. The phase difference between the specified boundaries is set as a variable and denoted as  $\phi_{x\_x}$ .

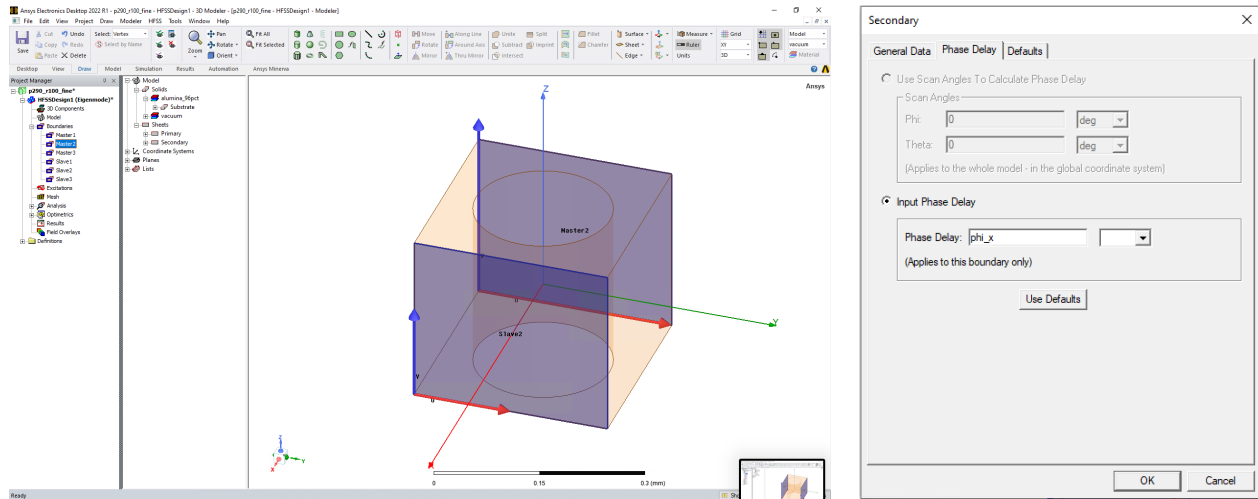


Figure C.3 Defining periodic boundary condition along  $x$ -direction.

4. As depicted in Fig. C.4, we opted for periodic boundary conditions along the  $z$ -direction. The phase difference between the specified boundaries is set as a variable and denoted as 0.

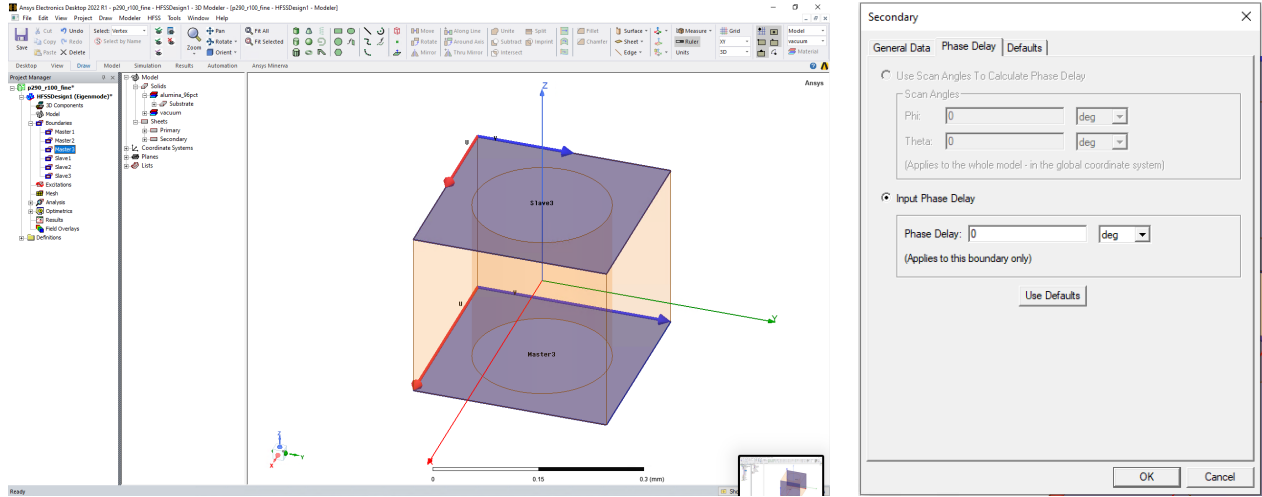


Figure C.4 Defining periodic boundary condition along  $z$ —direction.

5. As illustrated in Fig. C.5, we configured the *Eigenmode* solver to extract 9 modes. Subsequently, we employed the *Sweep Analysis* to sweep  $\phi_{i\_x}$  from 0 to  $\pi$ .

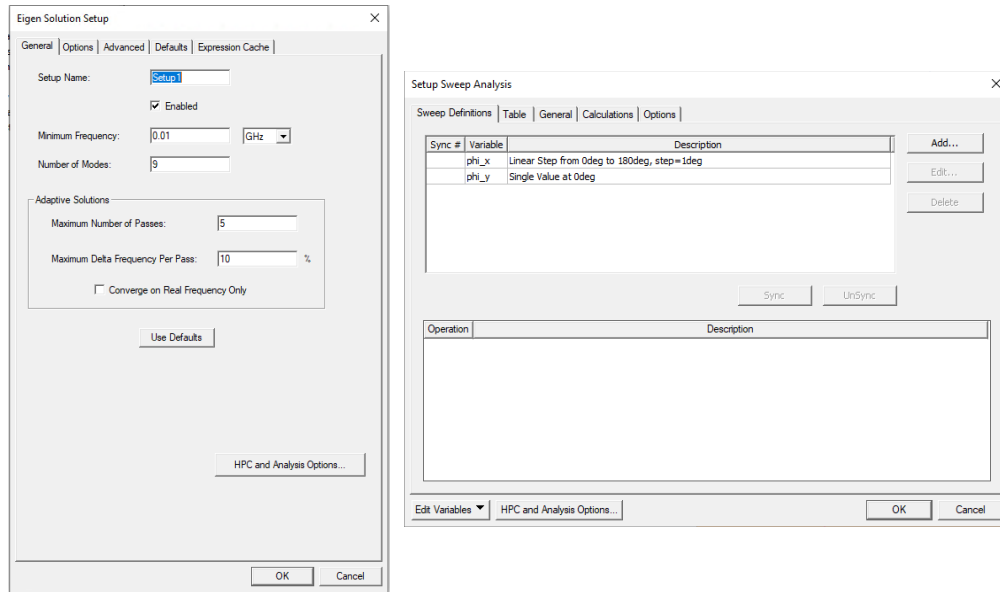


Figure C.5 Defining the *Eigenmode* solver and parameters sweep.

6. Following the completion of the simulation, as depicted in Fig. C.6, we formulated the following expressions to extract values for effective permittivity and effective dissipation factor.

$$\text{eps\_eff\_x} = ((\phi_{i\_x} \cdot c_0) / (2 \cdot \pi \cdot a \cdot \text{re}(\text{Mode}(1))))^2$$

$$\text{loss\_eff\_x} = \text{eps\_eff\_x} \cdot \text{im}(\text{Mode}(1)) / \text{re}(\text{Mode}(1))$$

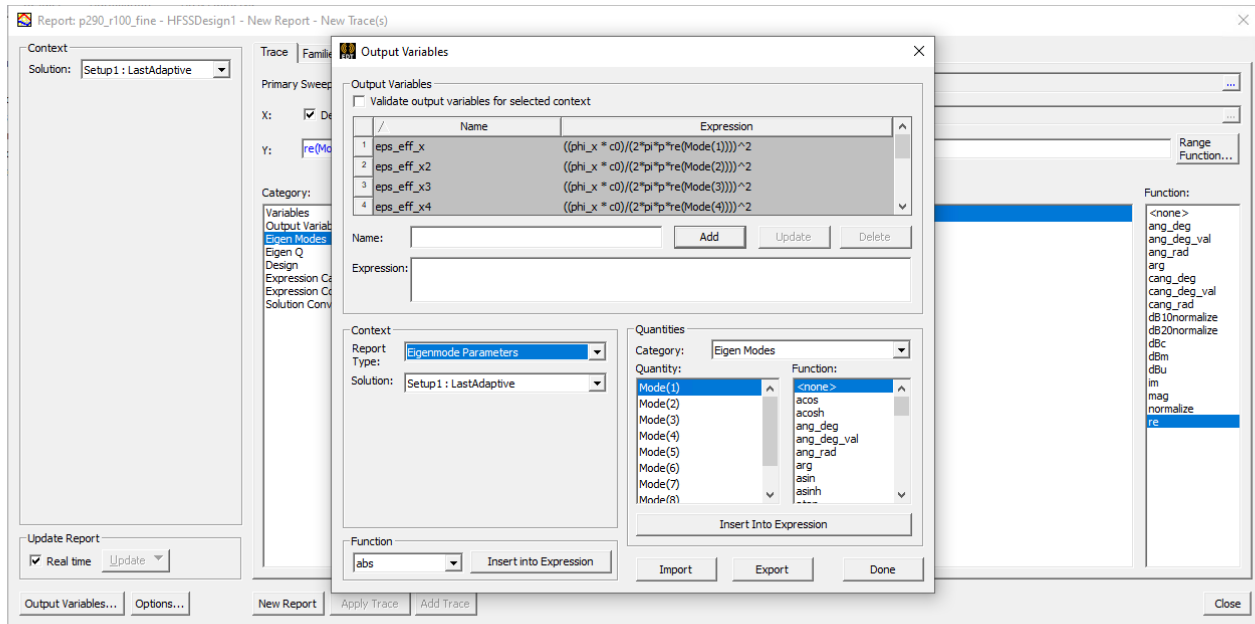


Figure C.6 Defining the formulation for effective permittivity and effective dissipation factor.

7. Subsequently, as depicted in Figs. C.7 and C.8, we generated plots for the variables  $eps\_eff\_x$  and  $loss\_eff\_x$  as defined.

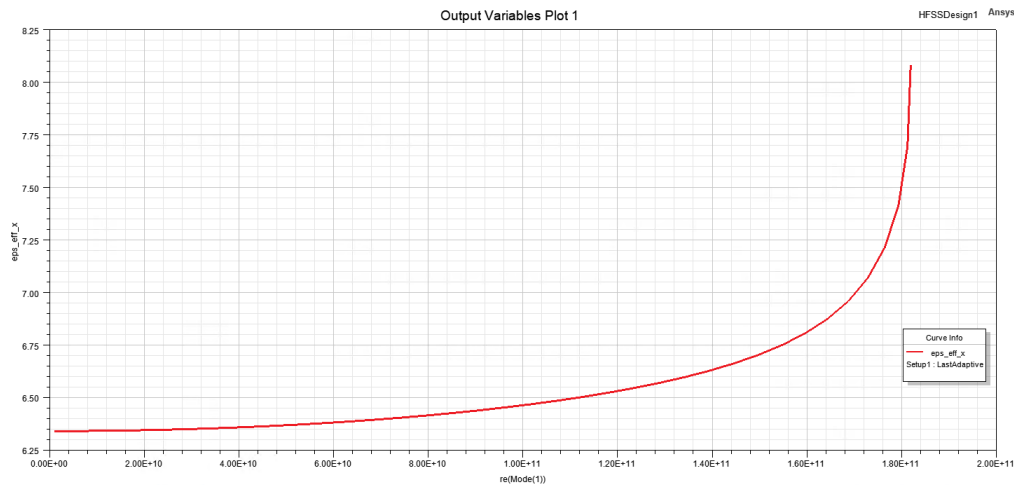


Figure C.7 Extracted effective permittivity of the fundamental mode.

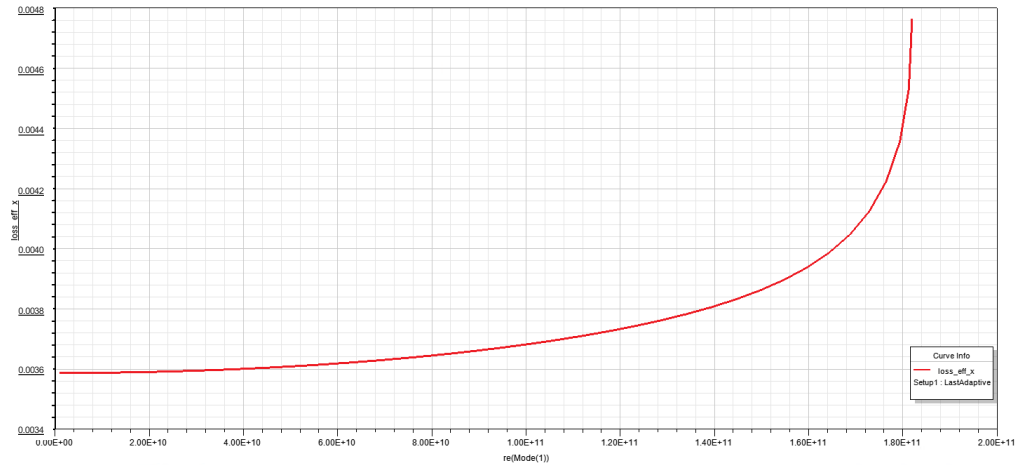


Figure C.8 Extracted effective dissipation factor of the fundamental mode.

## CST Suite Studio Simulation

Extracting the effective permittivity and effective loss of periodic perforations in a lossy dielectric substrate can be achieved by following the procedure outlined below:

1. To begin, as shown in Fig. C.9, we selected the following templates.

*MICROWAVES & RF/OPTICAL* → *Periodic Structures* → *FSS, Metamaterial - Unit-Cell*  
→ *Dispersion Diagram*

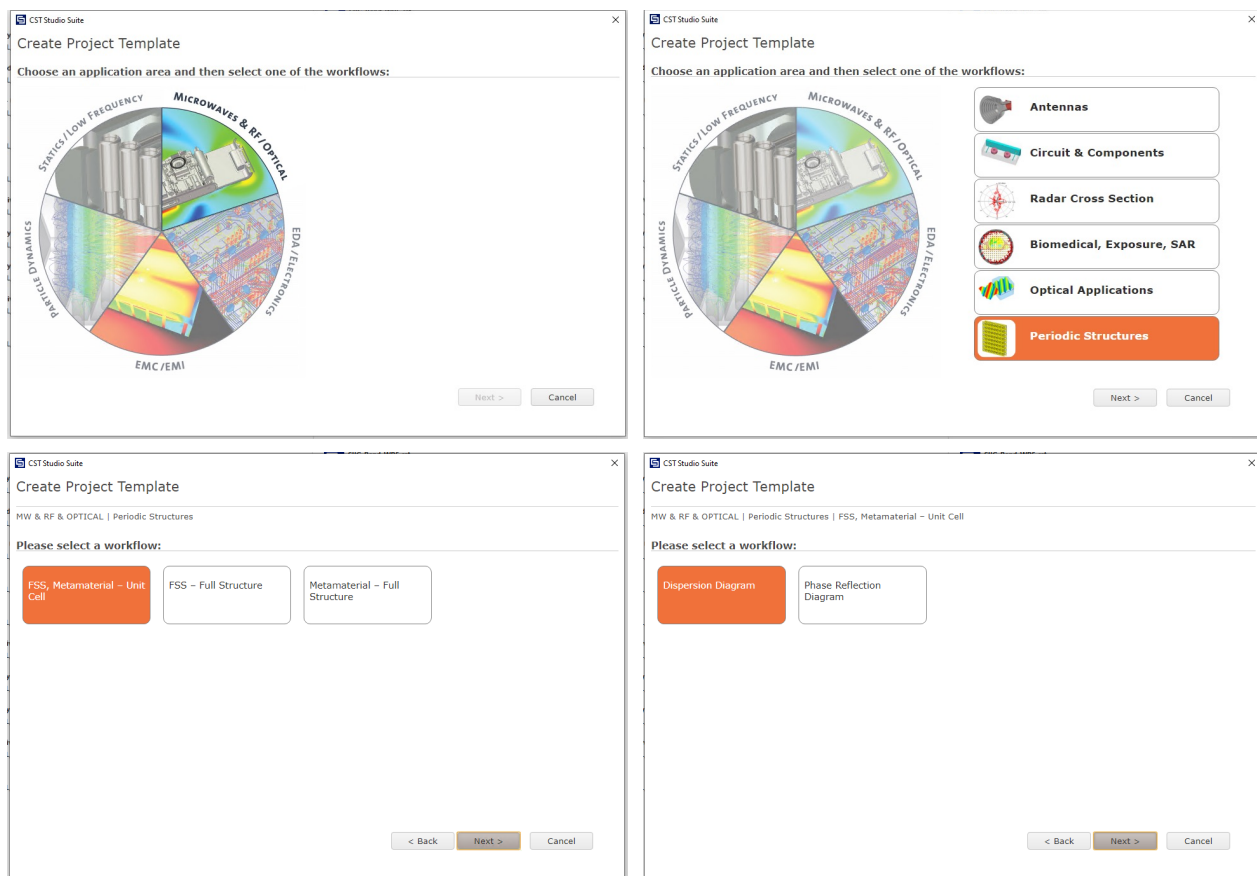


Figure C.9 CST Suite Studio template configuration.

2. As illustrated in Fig. C.10, we selected the *Eigenmode Solver*.

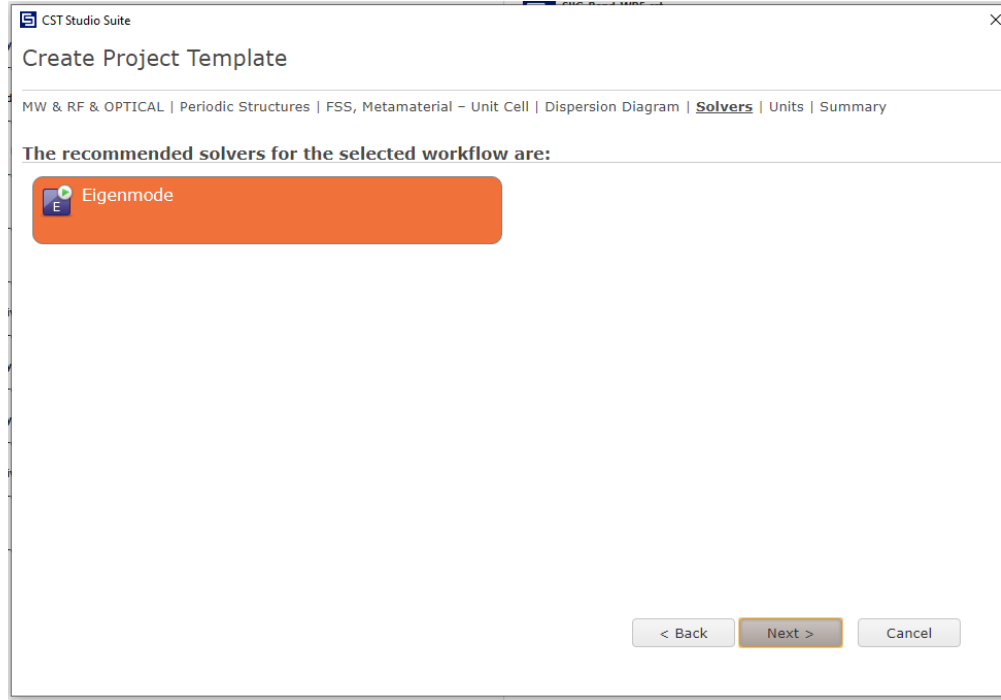


Figure C.10 *Eigenmode Solver* selection.

3. We created a rectangular unit-cell composed of Alumina substrate with a relative permittivity of  $\epsilon' = 9.4$  and loss tangent of  $\tan \delta = 6 \times 10^{-3}$ . The perforations have periodicity equal to  $a = c = 290 \mu m$  and dimensions of  $b = d = 200 \mu m$ . Then, as depicted in Fig. C.11, we implemented periodic boundary conditions in all directions. The phase difference between the defined boundaries is set as variables, denoted as  $phaseX$ ,  $phaseY$ , and 0 along  $x$ -,  $y$ -, and  $z$ - direction, respectively.

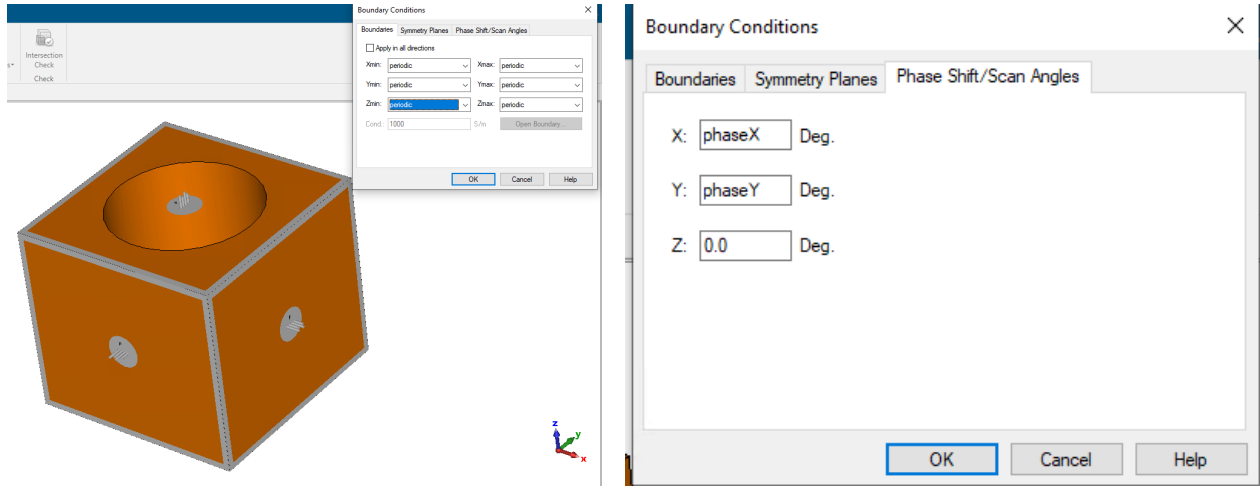


Figure C.11 Configuration of periodic boundary conditions.

4. As illustrated in Fig. C.12, we configured the *Eigenmode* solver to extract 9 modes. Subsequently, we utilized the *Sweep Analysis* to sweep the *PathPara* from 0.001 to 1.1.

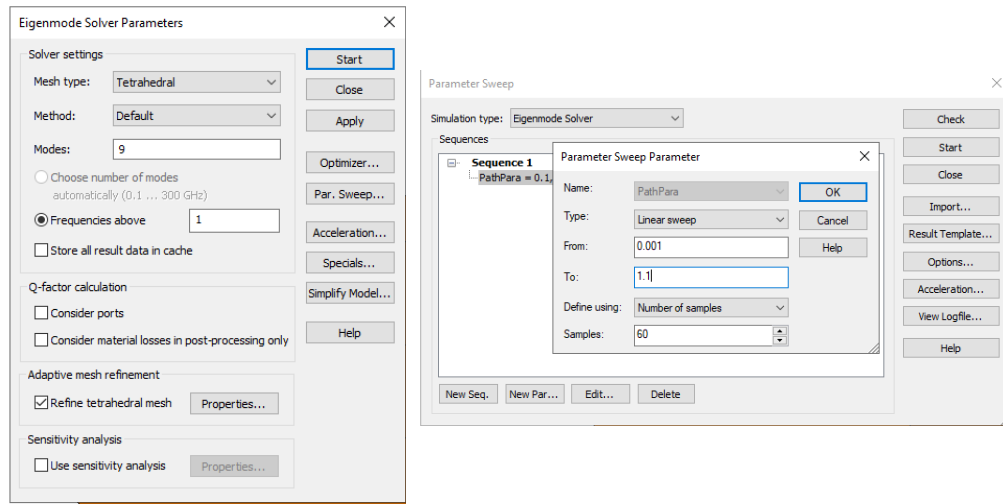


Figure C.12 Configuring the *Eigenmode* solver and parameter sweeps..

5. Following the completion of the simulation, as depicted in Figs. C.13 and C.14, we exported the values for the dispersion diagram and the Q-factor of each propagating mode.



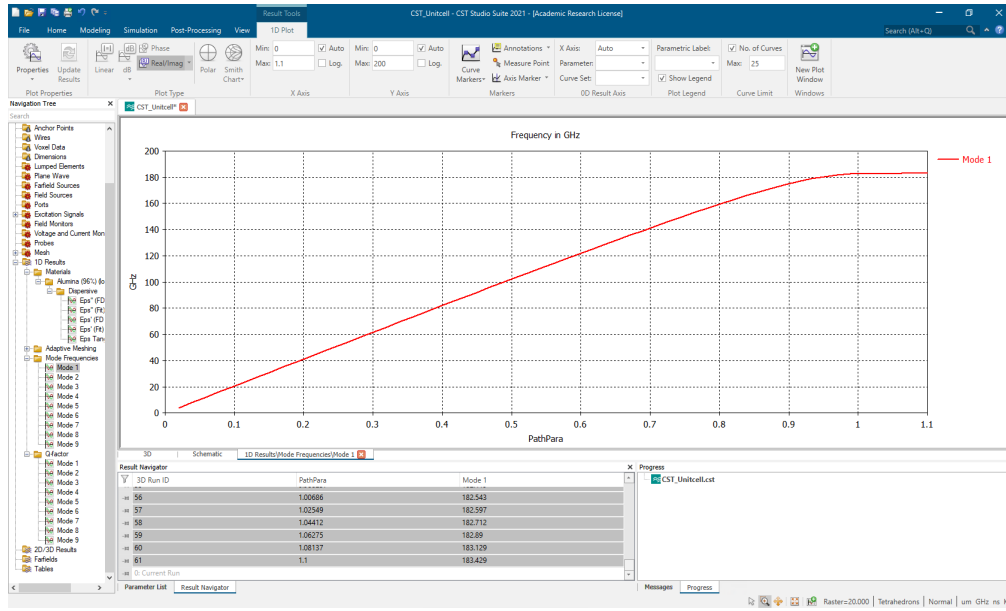


Figure C.13 Extracted dispersion diagram of the fundamental mode using the CST Suite Studio.

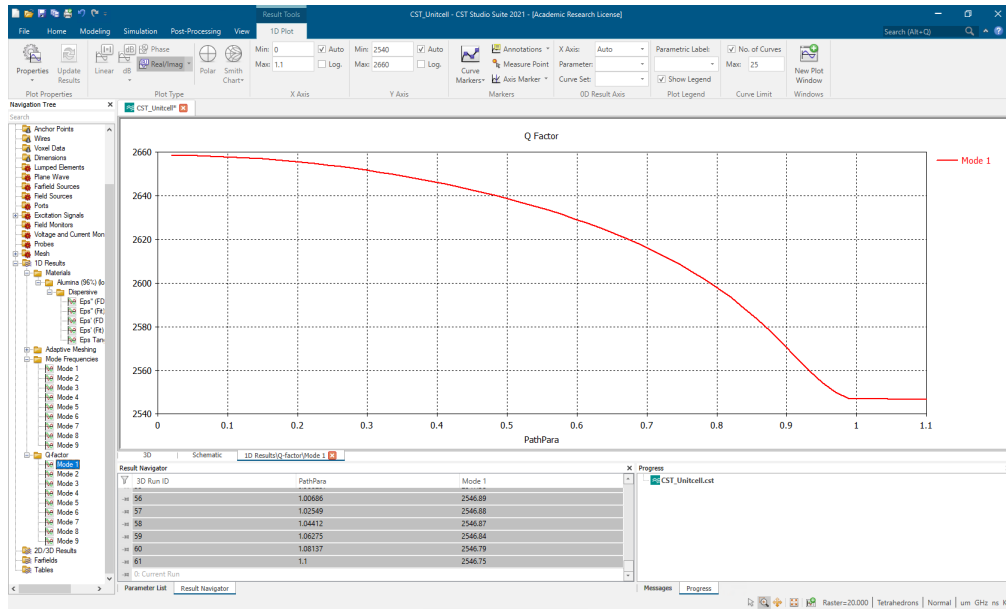


Figure C.14 Extracted Q-factor of the fundamental mode using the CST Suite Studio.

6. We imported the data into MATLAB software and applied the following formulation to calculate the effective permittivity. The extracted effective permittivity is depicted in Fig. C.15.

$$\text{delta\_x\_1} = \text{mode\_1}(:,1);$$

```
f_real_1 = mode_1(:,2);
eps_eff_1 = ((delta_x_1*c0)/(2*pi*a*f_real_1))^2;
```

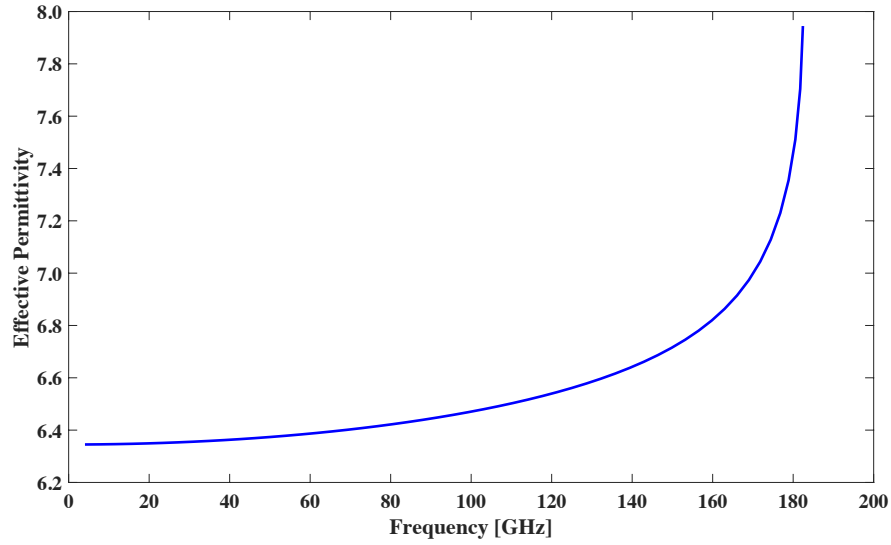


Figure C.15 Extracted effective permittivity of the fundamental mode.

7. We employed the following formulation to calculate the effective dissipation factor. The extracted effective dissipation factor is illustrated in Fig. C.16.

```
Q_Factor_1 = Q_1(:,2);
loss_eff_1 = eps_eff_1 * (1/2*Q_Factor_1);
```

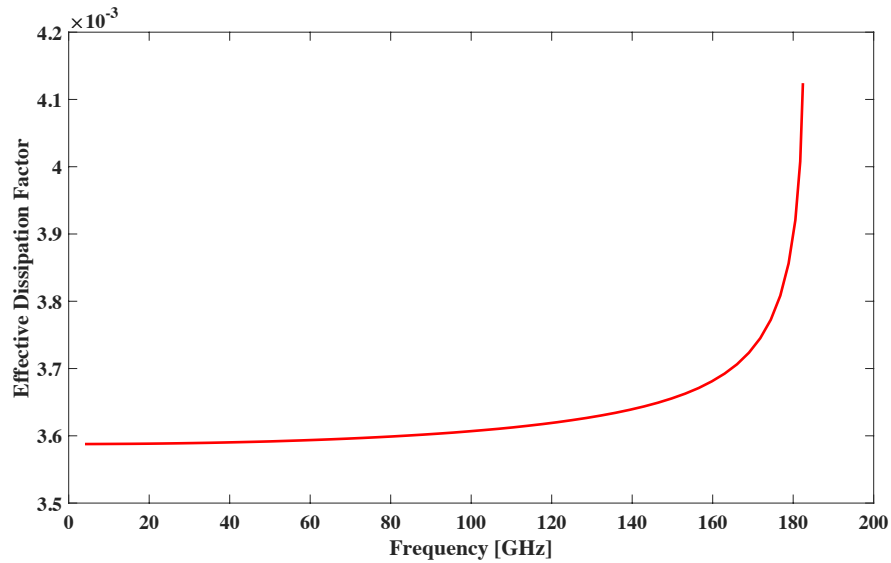


Figure C.16 Extracted effective dissipation factor of the fundamental mode.

## APPENDIX D

### Measurement and Fabrication Challenges

In this section, we examine several challenges encountered during the fabrication and measurement processes, elucidating the strategies employed to overcome these obstacles.

One of the most crucial challenges we encountered revolved around the selection of an appropriate substrate material for developing the SIIG waveguide. As previously mentioned, the WR-5.1 and WR-3.5 frequency bands exhibit significant dielectric losses. Consequently, a substrate with high permittivity and low dielectric losses is essential. Our initial attempt involved using a Silicon substrate, known for its lower dielectric loss compared to alumina. However, due to limitations with our laser-cut machine, we explored an alternative approach using Deep Reactive-Ion Etching (DRIE) to introduce perforations into the substrate. While this DRIE process proved effective, it did require more time and incurred higher costs than the laser-cutting method.

The designed SIIG structure incorporates extremely narrow tapers and guiding channels, rendering the structure inherently fragile. During the DRIE etching process, high gas pressure is applied to the Silicon wafer for cooling, posing a risk of breaking the SIIG structure. To address this challenge, we introduced an additional layer of wafer beneath the main wafer to enhance structural stability and prevent waveguide breakage. This modification proved effective; however, a new issue arose during high-temperature operation. The two wafers, subjected to elevated temperatures, inadvertently welded together. Subsequent attempts to separate these wafers resulted in the fracture of the entire fabricated SIIG, as illustrated in Fig. D.1.

In response to the challenges encountered, we opted to switch to the laser-cutting mechanism as an alternative to DRIE etching. The material available at the *Poly-grames Research Center* that met our criteria for high permittivity and sufficient firmness for laser-cutting was the alumina substrate. Despite its higher dielectric losses compared to the Silicon wafer, alumina was chosen due to the limited material options. Unfortunately, we faced further constraints as only two thickness options were available, specifically  $254\ \mu\text{m}$  and  $127\ \mu\text{m}$ . This restricted range of thicknesses added complexity to the design process, limiting the achievable results, given the significant impact of substrate thickness on the performance of the SIIG structure.

Another significant challenge we faced was the necessity of maintaining a  $25.4\ \mu\text{m}$  wall distance between adjacent perforations. This constraint was dictated by the available laser-

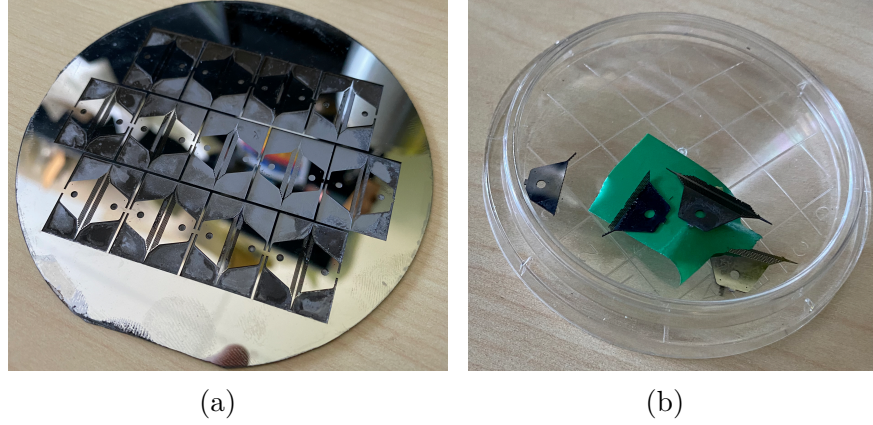


Figure D.1 Difficulty encountered in fabricating SIIG waveguides on a Silicon wafer.

cutting machine, its operating power, and the characteristics of the laser beam. To ensure the structural integrity and mechanical stability of the SIIG, a minimum distance of  $25.4\ \mu\text{m}$  between adjacent perforations was crucial. It's important to note that larger perforations would result in more substantial substrate removal, leading to a lower effective permittivity in the perforated region. This, in turn, would enhance the contrast between the permittivity of the guiding channel, offering improved performance for the SIIG structure. However, this imposed limitation inherently restricted the achievable permittivity contrast, consequently placing constraints on the overall performance potential of the designed SIIG structure.

Another challenge we encountered pertained to the ground plane. Our research indicated that a ground plane with higher conductivity could minimize conductor losses in the overall structure, leading to improved performance for the designed SIIG structure. However, due to material constraints at the *Poly-Grames Research Center*, we were limited to using aluminum, which inherently has higher conductor losses compared to gold and silver materials.

Furthermore, achieving optimal performance required the alumina substrate to be precisely positioned atop a metallic ground plane. Unfortunately, the CNC machine used for fabricating the feeding platform and ground plane couldn't provide a perfectly flat surface. To address this, we took the additional step of sanding the aluminum ground plane to ensure a smooth, flat surface. Subsequently, as shown in Fig. , we introduced two screws to exert pressure on the alumina substrate, eliminating any potential air gap between the substrate and ground plane and enhancing the overall performance of the SIIG structure.

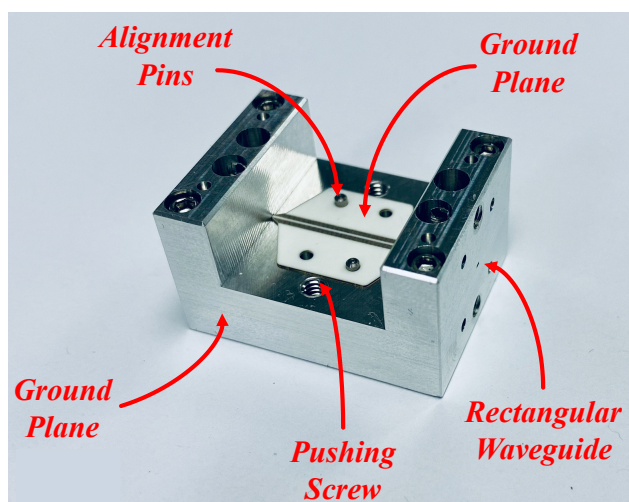


Figure D.2 The fabricated SIIG structure fed by rectangular waveguide.

## APPENDIX E

### Published and Submitted Articles

The Ph.D. thesis under consideration comprises the following resulting articles:

#### Peer-Reviewed Journals:

- **Article 1: M. Moradi**, M. S. Sharawi, and K. Wu, "Analytical Model of Guided Waves in Periodically Perforated Dielectric Structures and Its Applications to Terahertz Substrate-Integrated Image Guides (SIIG)," *IEEE Transactions on Microwave Theory and Techniques*, vol. 71, no. 10, pp. 4236–4246, 2023. (Published)
- **Article 2: M. Moradi**, M. S. Sharawi, and K. Wu, "Exploring Low-Loss Wideband Substrate-Integrated Image Guides (SIIG) for Terahertz Applications," *IEEE Transactions on Terahertz Science and Technology*, 2023. (Accepted)
- **Article 3: M. Moradi**, M. S. Sharawi, and K. Wu, "Substrate-Integrated Hybrid Dielectric-Metallic Image Guide (SIHDMIG) Architecture and Its Applications in Developing sub-THz/THz Power Divider," *IEEE Transactions on Microwave Theory and Techniques*, 2023. (Submitted)